Journal of Energy Challenges and Mechanics

ISSN 2056-9386

http://www.nscj.co.uk/JECM/

Volume 3, Issue 2
July 2016

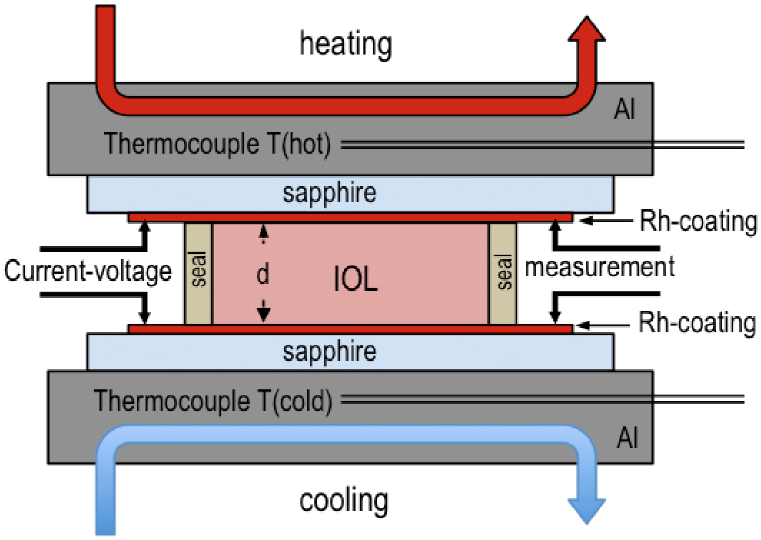

Featured article:

Potential of Thermoelectric Generators based on Ionic Liquids

Stefanie Uhl[1], Edith Laux, Tony Journot, Loïc Piervittori, Laure Jeandupeux and Herbert Keppner*
[1] Haute Ecole Arc Ingénierie (HESSO), Eplatures-Grise 17, 2300 La Chaux-de-Fonds, Switzerland

North Sea
North Sea Conference & Journal LTD
2 Charlestown Walk, Cove Bay, AB12 3EZ, Aberdeen, Scotland, United Kingdom
http://www.nscj.co.uk/JECM/ | jecm@nscj.co.uk | +44(0)1224 875635

Journal of Energy Challenges
and Mechanics
http://www.nscj.co.uk/JECM/
ISSN 2056-9386
Volume 3 (2016) issue 2

TABLE OF CONTENTS pages

Journal of Energy Challenges
and Mechanics
http://www.nscj.co.uk/JECM/

ISSN 2056-9386
Volume 3 (2016) issue 2, article 1

Potential of thermoelectric generators based on ionic liquids

基于离子液体的热电发生器之潜力

Stefanie Uhl[1*], Edith Laux, Tony Journot, Loïc Piervittori, Laure Jeandupeux and Herbert Keppner

[1] *Haute Ecole Arc Ingénierie (HESSO), Eplatures-Grise 17, 2300 La Chaux-de-Fonds, Switzerland*

stefanie.uhl@he-arc.ch

Accepted for publication on 14 May 2016

Abstract - **In advanced thermoelectric materials the key aspect lies in the reduction of the thermal conductivity while maximizing electric carrier transport. Skutterudites, clathrates, Half-Heusler compounds, complex chalcogenides and thin-film properties are only examples of tracks which are taken to optimize material properties for thermoelectric applications.**

New in the row of the advanced materials is Ionic Liquids (ILs) which have been investigated regarding their thermoelectric properties only by a few research groups in the last years. ILs are organic salts that exist as liquids below a threshold temperature, various at room temperature, and constitute a new generation of solvents composed of 100% of cations and anions.

The possibility to fine-tune practically all the ILs physiochemical properties by modifying its chemical structures makes IL truly designer solvents and might allow the optimization of the thermoelectric properties. Out of 15 tested off-the-shelf ILs a large range of Seebeck coefficients and Power outputs could be observed.

The potential of ILs does not only lie in the promising thermoelectric properties; liquids could also open new fabrication methods regarding flexible TEG modules using the Solid-on-Liquids Technology.

This paper investigates in a first part fundamental material studies of the promising protonic Ionic Liquid, Ethylammonium nitrate (EAN). In a second part, the integration of Ionic Liquids in a thermoelectric generator module is demonstrated.

Keywords - **Ionic Liquids, Thermoelectricity, Flexible TE modules, Low Power Generation**

I. INTRODUCTION

Reduction of thermal conductivity of a TEG is obvious due to the fact that a high thermal conductivity will not allow the creation of a significant temperature difference at reduced heat-flows. By that the generator voltage is poor and a high number of junctions must be serially connected. Looking at applications, the trend goes to energy autonomous devices. Originally the military was demanding for solutions, but also space missions. Recently, modern microelectronics had a tremendous success in further reduction of power consumption of all kinds of integrated circuits, displays, CMOS devices etc. which allows to drive them with a low power TEG as long as the created voltage is sufficiently high [1]. Thermoelectric Generators have, (together with photovoltaic generators) no moving mechanical parts and no maintenance is needed within their lifetime.

Conventional $(Bi,Sb)_2(Te,Se)_3$-based thermoelectric materials and devices report very good performances at room temperature [2]. However if these materials are assembled and series-connected as a large number of bulk elements, certain difficulties and limitations arise in making highly miniaturized and flexible modules. Flexibility is one aspect that let increase the field of application of a TEG, since it can be applied around an object that needs to be electrically powered. Trends are observed in using wearable generators that can make use of the bodies' heat for powering biomedical devices, but also for consumer electronics such as bracelets for watches and acquisition systems for sports activities.

For such applications high flexibility is particularly needed [3-6] allowing a better thermal contact to the heat source surface as compared to rigid systems that must be mechanically clamped. Therefore TEG's technology passes more and more to thin-film technology allowing serial connection of the junctions at low space for obtaining the needed system voltage. The use of $(Bi,Sb)_2(Te,Se)_3$- thin films allows increasing the integration of P/N couples on a given surface, however the maintainable temperature difference over the module is limited, again, due to the high thermal conductivity which leads, again, to low output voltages [7].

Due to low thermal conductivities of Ionic Liquids (e.g. $[BMIM][BF_4]$ λ=0.184W/mK [8]) the temperature gradient between hot and cold electrode is maintained and high Seebeck coefficients ($[BMIM][BF_4]$ S=850µV/K [18]) could be shown. In contrast, the electrical conductivity ($[EAN][NO_3]$ σ=2.82S/m [9]) is generally low as compared with solid-state materials.

TEGs using ILs combined with elastic silicone-based substrates combine two effects: first high flexibility can be achieved; second, low thermal conductivity of the IL prevents a thermal short-circuit (see Fig. 1) and generates therefore enhanced voltages. In order to guarantee bubble-free packaging for the IL and series connection, solid on liquid technology will be applied [10].

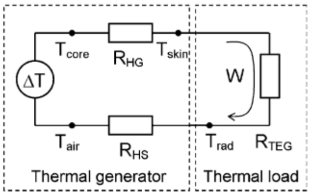

Fig. 1: Equivalent thermal circuit of a generator with a thermal load [11]. A TEG with a low thermal resistance will short-circuit the temperature difference.

Moreover, the reliability of TEG modules might be improved by ensuring a stable interface between the thermoelectric material and the electrode. The performance of solid-state-based TEG modules tends to degrade with thermal cycling as the constituent materials and the interfaces are exposed to large temperature gradients. This increases the internal resistance caused by poor contacts and micro cracks between a thermoelectric material and the electrode [12].

II. EXPERIMENTAL

2.1. MEASUREMENT SETUP

The current-voltage characteristics of the ILs of the generator have been performed in a specially designed test cell sketched in Fig. 2 [13]. The test setup consists of two thermally highly conductive sapphire plates that are coated with an inert electrode material (1µm Rhodium) that is in contact with the IL. Externally a 4-point configuration allows the current-voltage-power measurements and obtaining the data of the Seebeck coefficient. To avoid IL losses, the cell is sealed using a silicone gasket (d=4mm). The aluminium bodies are connected with a heater (thermal resistor, Vitelec, France) and cooler system (Thermostat Frigiterm, J.P. Selecta S.A, Barcelona, Spain); the thermocouples (Type K, Jumo-Regulations, Metz, France) are placed close to the sapphire plates between the IL and the heater, respectively cooler (Fig.2).

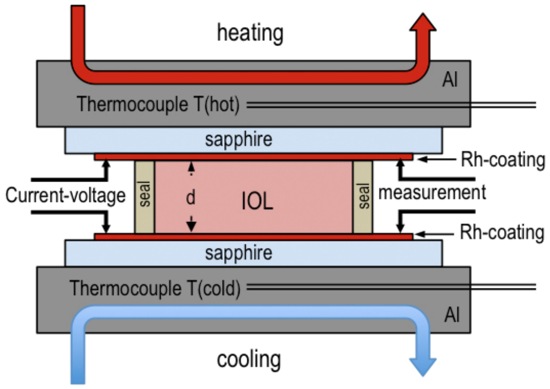

Fig. 2 Experimental setup for the characterization of the TEGs based on ILs

In order to extract a current from the TEG, redox couple I_2/LiI was added to the IL. The thermally generated potential difference at the electrodes was shunted using high precision resistors and the output current could be determined. For measurements of the open circuit voltage (V_{OC}) and the voltage under load, a high impedance voltmeter was used (Data Acquisition System 34970A and 34901A, Agilent, Santa Clara, CA, USA). The system is fully automatized allowing measuring the potential difference and the heating/cooling dynamics, as well as the stabilization of the measured data. The I-V characteristic was obtained by switching a resistance cascade in parallel to the test cell using the 4-probe-method. The resistances between 5Ω and 100MΩ have a tolerance of 0.1%. Every 10 seconds a measurement is taken and the maximum errors from the measurement system are less than 1 µV and ±1.5 K. The error in the temperature measurement due to thermal resistances at the contacts is not taken into account at this stage. The total concentration of impurities in the studied ILs was less than 2 % (Ionic Liquids Technologies, Heilbronn, Germany), and a concentration inaccuracy of the added redox couple of ±10 % is assumed.

The relative Seebeck-coefficient was determined from the slope of the measured voltage-temperature curve as:

$$S_E = (U_{max} - U_{min}) / (\Delta T_{max} - \Delta T_{min}) \quad (1)$$

Whereby ΔU_{min} is the potential difference [V] between the hot and cold electrode at the temperature difference ΔT_{min} [K] and $\Delta U_{max,}$ the potential at ΔT_{max}.

One of the principle advantages for using IL in TEGs is seen in the unique possibility for significantly reducing the thermal conductivity of the active substance. In previous work [13] it was mentioned that the heat flow in TEG based on ILs is convective, hence the effective heat-conductivity must be measured of better understanding the devices. These measurements have been carried out using a test cell as shown in Fig. 2 which was put into a vacuum system at 5 Pa pressure. In this case parasitic heat loss from the heater electrode (copper in this case) could be avoided.

2.2. RESULTS AND DISCUSSION

EAN was found to be the so far most promising IL as soon as 0.4 Mol/l redox couple I_2/LiI is added [14]. Furthermore, the output-power of the TEG could be increased by heating the cold electrode to about 30 °C. This effect was attributed to thermal activation of bulk-conductivity effects, but also as thermal activation for enhanced electron exchange between the electrode and the Helmholtz layer. In Fig. 3 it can be seen that the current that can be extracted from a TEG, has a maximum at higher temperatures as the maximum power point. It is surprising that just not a high difference between the hot and the cold electrode exhibits the best working condition for an IL-based TEG; the cold electrode must be rather activated.

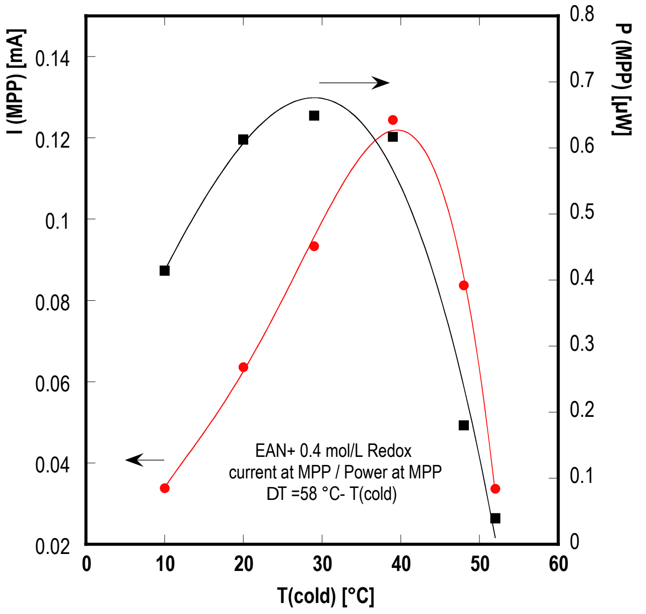

Fig. 3: Mismatch between the maximum power point and the highest extractable current. The cold electrode must be "activated" [14].

In Fig. 3 the reduction of the temperature difference between the fixed T(hot) =58°C and the increasing variable T(cold) gives rise to continuous voltage reduction that has its impact on the power of the device. Allowing T(hot) to increase let match the current maximum with the power maximum. The effect of heating the cold electrode was further researched comparing the same sample under 50-30 conditions [T(hot) = 50°C; T(cold) = 30°C] with 130-60 conditions. For 3.5 times increasing of the heat flow Fig. 4 shows that the electrical power increases 77 times.

In a next step T(hot)-T(cold) was kept constant at 5 K and the hot temperature was varied starting form 20°C up to 94°C. The experiment was assumed getting more insight into the ideal working conditions of IL-based TEGs. Fig. 5 shows the voltage-current and Fig. 6 the voltage-power characteristics.

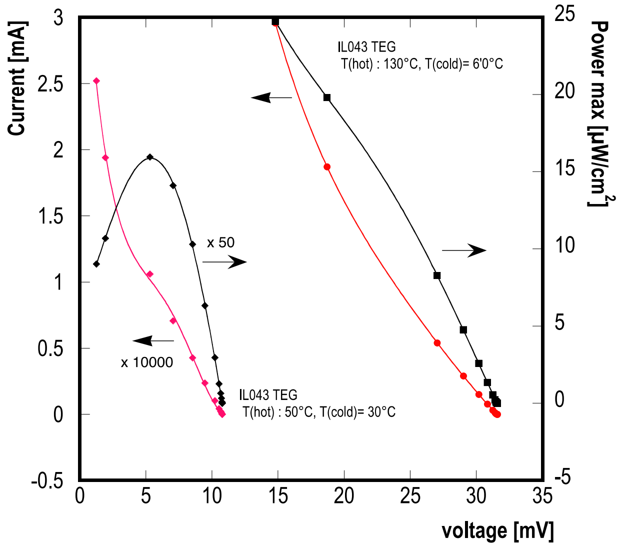

Fig. 4. Comparison of the V-I-P characteristics of EAN+0.4 Mol/L I_2/LiI under 50-30 (left) and 130-60 (right). The power is increased 77 times.

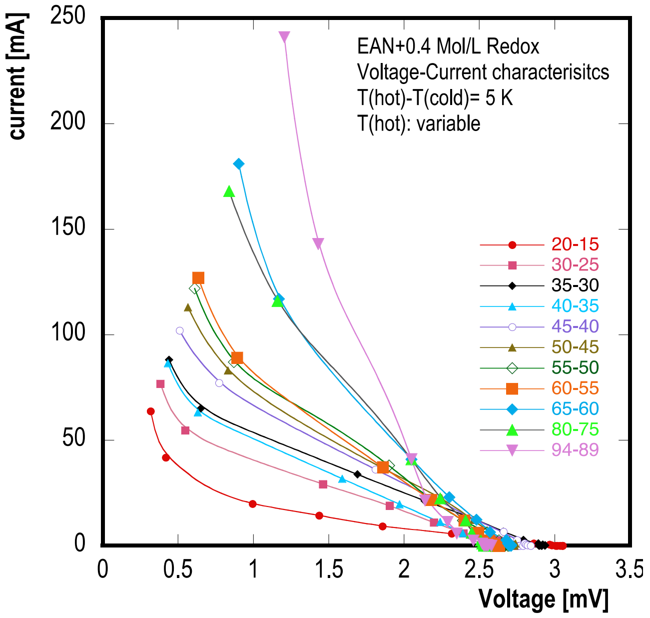

Fig. 5 V-I characteristics of EAN+0.4Mol/L redox for temperature differences of 5 K.

Fig. 5 confirms the trend that current extraction needs heat; note the heat-flow P through the generator is defined by equation (2):

$$P = A \cdot \frac{\lambda}{d} \cdot \Delta T \qquad (2)$$

whereby, A is the surface where the IL is in contact with the electrode. Looking at Fig. 6 it can be observed in this systematics that the maximum power point is at low T(hot)-values rather at increased voltages, whereas at increased T(hot)-values it is shifted to lower voltages.

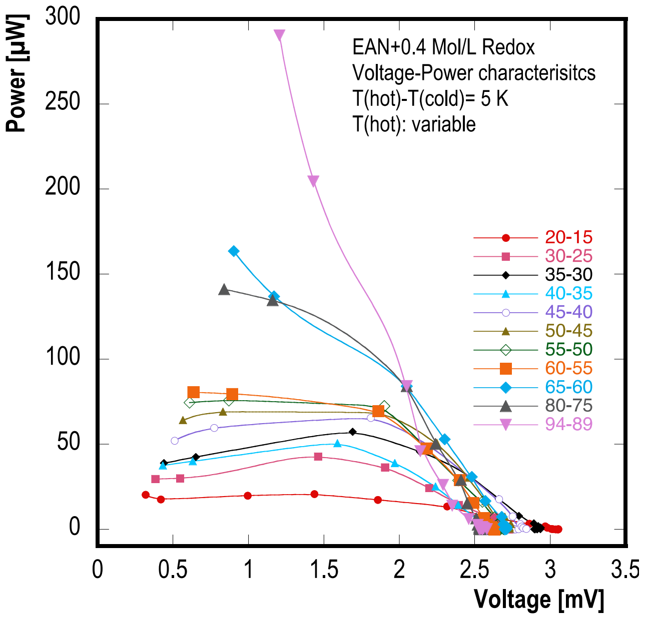

Fig. 6: Voltage-Power characteristics of the TEG from Fig. 5. Note the Maximum Power point is shifted to lower voltages as soon as T(hot) is increased.

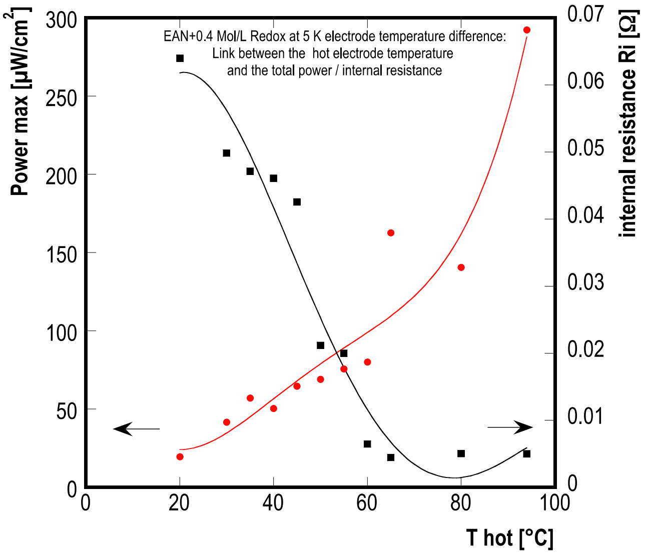

Fig. 7: Link between the internal resistance calculated from Ri=V(MPP)/I(MPP) and the maximum power output and T(hot).

Looking at Fig. 5 and 6, it is obvious that the power follows the current as soon as T(hot) is increasing. However, the open circuit voltage is decreasing. Looking at solid-state devices, the voltage depends rather exclusively from the temperature difference. Fig. 8 evaluates the Seebeck coefficient for the series of the measurements from figures 5, 6 and 7.

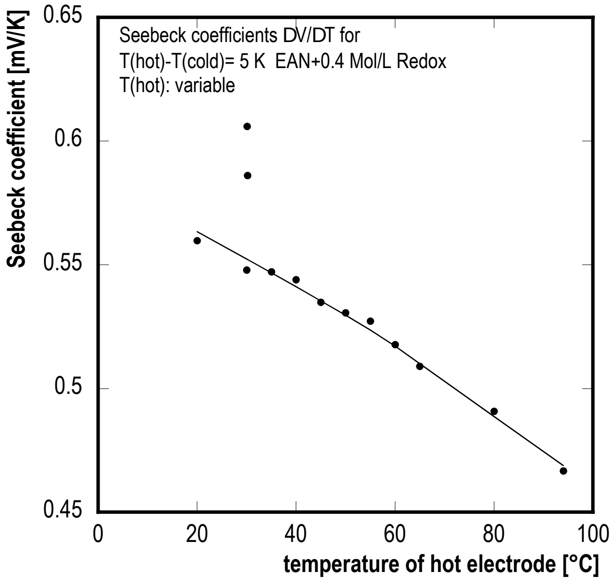

Fig. 8: Despite the constant temperature difference (5 K), the Seebeck coefficient (V_{OC} / T(hot)-T(cold)) decreases with increasing T(hot). Repeated measurements of the point 30-25 were not reproduced, probably due to different electrode coverage.

The effect observed in Fig 8 is surprising and a model explaining this observation is needed. There are two mechanisms that could explain the phenomenon:

1. Due to enhanced T(hot) and T(cold) the thermally selective carrier attachment at the electrodes is reduced due to modified Helmholtz-layer / electrode interaction.
2. Due to the fact that the cells of the generator have rather a large diameter (A = 176.7 mm^2) at low thickness (d = 4 mm), the heat transport is highly convective. Enhanced convective flow at globally higher temperatures (T(hot) and T(cold)) increases the apparent total heat conductivity, leading to a reduced temperature difference in the vicinity of the liquid-electrode interface, and by that to a reduced V_{OC} and Seebeck coefficient.

In order to find an explanation, the apparent heat conductivity (consisting of laminar and turbulent contribution) was measured. The cell of Fig.2 was equipped with a high heat-capacity copper electrode and put into a vacuum system to avoid unwanted parasitic heat losses. For this experiment, the Copper-body was heated up; after switching off the heater the stored thermal energy was released via the sample into the cooled Al body. For verification, the experiment was carried out only using the Copper/Sapphire/Sapphire/Aluminum stack and the sample arrangement without IL in the reservoir. The results of the measurements are summarized in Fig. 9.

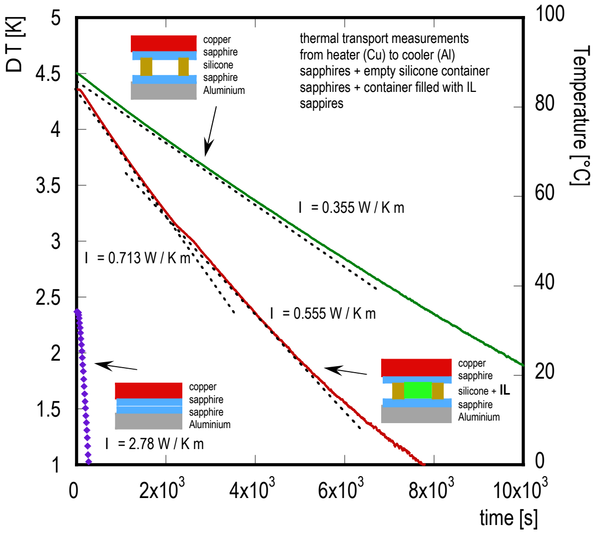

Fig. 9: Heat transport experiments using three different configurations. The middle curve represents the sample that is loaded with EAN+redox.

As assumed the left graph show the strongest decay (linear); the transport is dominated by the 3 interfaces (Cu/sappire, sapphire/sapphire, sapphire/Al) the total conductivity is 20 times smaller as Sapphire 42 W/(mK). The upper curve represents the unloaded sample holder with an apparent heat conductivity of λ=0.355 W/(mK). The IL loaded sample indicates two slightly different regimes (modified slopes); the one between 80°C and 50°C is more pronounced (λ= 0.713 W/(mK)), as compared to the one between 50°C to 30 °K (λ = 0.555 W/(mK)). The measurement of the heat conductivity could support model 2, but does not exclude model 1.

III. APPLICATION

3.1. DESIGN AND FABRICATION OF SERIAL CONNECTED THERMOPILES

The proposed TEG (Fig.10) comprises a flexible Silicone substrate (e.g. Polydimethylsiloxane (PDMS), thickness range 0.25-3.2mm) and a plasma bonded thin polymer film (e.g. Mylar®, thickness range 0.36-0.75µm) on both sides, which contain the electrode pattern for the serial connection of the IL cells. PDMS is suitable due to its chemical inertness, flexibility and low heat-conductivity (λ=0.15 W/(mK)), avoiding parasitic heat-flow through the generator. Looking at Fig. 9 typical heat-flows through an EAN TEG are less than λ=0.5 W/(mK)). Furthermore, plasma assisted bonding together with Solid on liquid deposition [10] allow a perfect bubble-free hermetic sealing. A first prototype of 34 serial-connected cells is represented in Fig. 10.

Fig. 10: TEG module (1.5x1.5cm) with 34-serial connected IL-cells based on a Silicone substrate.

In the following, a schematic representation of the fabrication steps is shown in figure 11. The polymer foil is structured by Laser (Laser Nanoseconde, Type Nd:YAG Fresco-Ultra, Fab. Coherent, spot size 20µm) and partially masked with blue tape (I), see Fig. 12. The holes have a diameter of 0.3mm and the masked area corresponds to the electrode pattern (Ø1.2mm, track width 0.8mm, track length 13 mm) which is coated with Rhodium in a later step. (II) In a plasma enhanced chemical vapor deposition process (PECVD), a SiO_x layer is deposited with a gradually changing composition, starting with an inorganic SiO_2 layer (ratio 2 O_2/HMDSO) and ending with an organic composition (ratio 15 O_2/HMDSO). This adhesion layer is necessary to reach a strong bond between the polymer foils and the silicone substrate by plasma bonding. The area for the metal electrodes are spared because of the adhesion properties. The electrode pattern is coated in a physical vapor deposition (PVD) process and the thickness of the rhodium layer is 500nm (V), see Fig. 13. The mask is subsequently lifted off and the patterned polymer foils are plasma bonded (N_2 10 Pa, 50W/40sec, curing 2h/60°C) to the Polydimethylsiloxane (PDMS) substrate on both sides (VII). Before filling the cavities, the surfaces are activated with an argon plasma for a good wettability (Ar 10 Pa, 20W/60sec). The masked device is placed in a vacuum chamber together with a reservoir of IL which is tilted to pour the liquid over the cavity inlets (Fig. 14). By setting the sample again under ambient pressure, the cavities are filled with the ionic liquid, see Fig. 15 and 16. The same procedure is repeated for the opposite side with the second Ionic Liquid (Fig. 17).

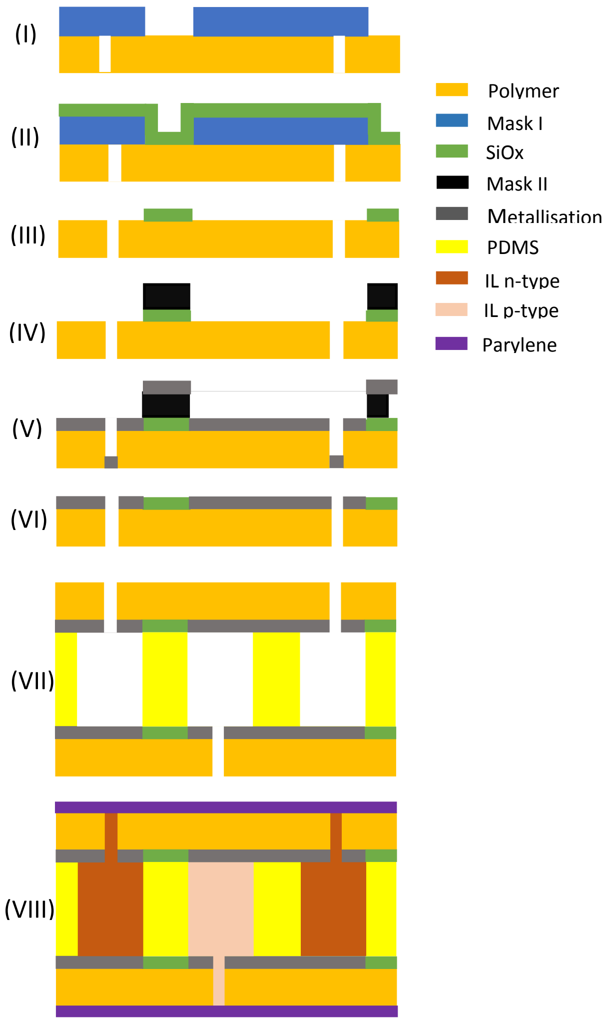

Fig. 11: (I), (II) and (III) Polymer foil and mask is structured by Laser to coat the SiOx adhesion layer; (IV), (V) and (VI) Subsequently the electrode pattern for the serial connection of the cells are coated by PVD; (VII) on both sides of a laser structured PDMS substrate, a patterned polymer foil is plasma bonded; (VIII) the cavities are filled under vacuum and the liquid is encapsulated.

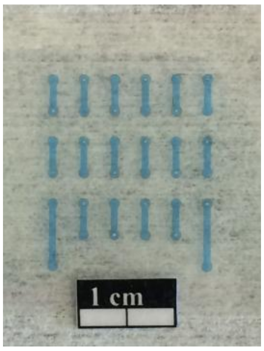

Fig. 12: Mylar Foil structured by laser and masked with bluetape

Fig. 13: Rhodium electrodes, deposited by sputtering; layer thickness 500nm

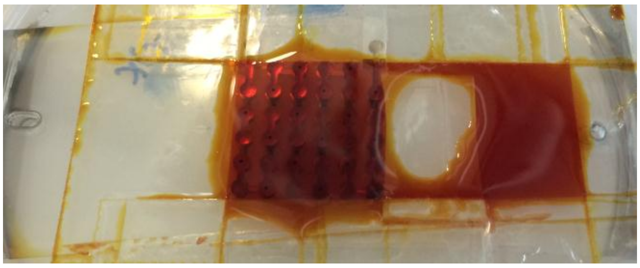

Fig. 14: Vacuum filling technique for cavities: Liquid is applied in the reservoir (right side) and the substrate is tilted after applying the vacuum. The liquid flows through a narrow channel over the inlets of the cavities (left side) and after a complete coverage, the sample is set again under ambient pressure. While cycling the pressure, residual air bubbles in the cavities are degased and the cavities are completely filled with IL.

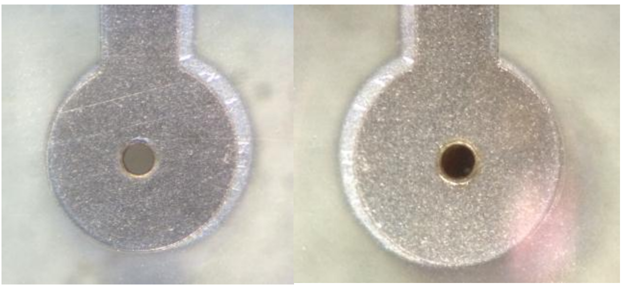

Fig. 15: left: unfilled cavity (hole diameter 0.3mm); right: IL-filled cavity

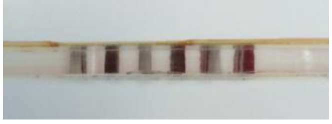

Fig. 16: TEG module filled from one side with ionic liquid (e.g. p-equivalent type of IL)

Fig. 17: TEG module is turned and filled with the second IL (e.g. n-equivalent type)

3.2. CHARACTERISATION OF THERMOPILE

The characterization of the prototype was made in the setup described above, to determine the total Seebeck coefficient and of 34 serial-connected IL cells. As shown in previous work [18], IL with positive and negative Seebeck coefficients could be found. EAN+ 0.2 Mol/l I_2/LiI has a positive coefficient and 17 cells have been filled with and the residual 17cells with Methyl-3-propyl iodide (PMIM I) with 0.2Mol/l I_2 (negative coefficient).

In a former material study, the two ILs have been characterized with the following Seebeck Coefficents:

EAN + I_2/LiI 0.2 Mol/l → S_E= 629µV/K

PMIM I + I_2 0.2 Mol/l → S_E= -56µV//K

Theoretically, the TEG module should therefore have a total Seebeck Coefficient of:

$$S_{E\_total} = 17 \times 629\mu V/K - 17 \times (-56\mu V/K)$$

$$= 11.6mV/K$$

The determined Seebeck Coefficient was 9.24mV/K.

The difference might be explained by a locally lacking thermal contact when heating/cooling the 34 cells.

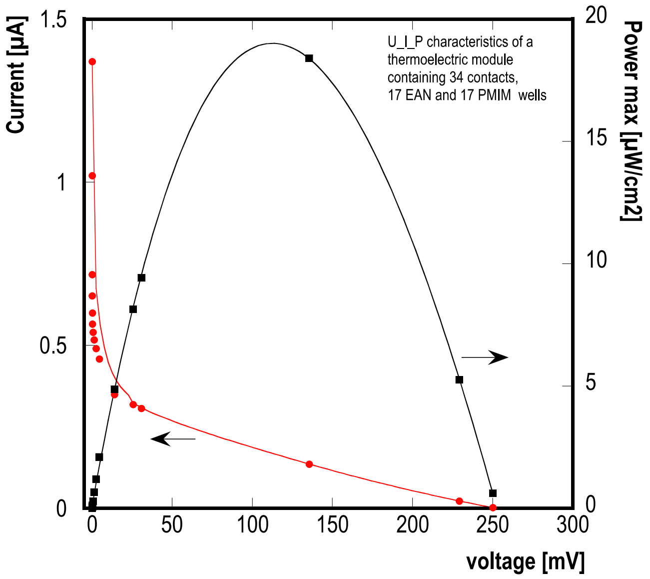

Fig.18: Prototype with 34 serial-connected cells (ΔT=37K); Ethylammonium nitrate with 0.2Mol/l I_2/LiI and 1-Methyl-3-propyl iodide (PMIM I) with 0.2Mol/l I_2

Looking at the power output of the device, one can observe a pounced mismatch between the properties of the liquids with positive and negative Seebeck coefficients (Fig. 19); the liquid PMIM I has a high cell resistance and limits therefore the current extraction [18]. Further material research has to be done to find or design an Ionic Liquids with a negative Seebeck Coefficient and the ability of a high carrier extraction. Fig. 18 and Fig. 19 illustrate the mismatch in detail.

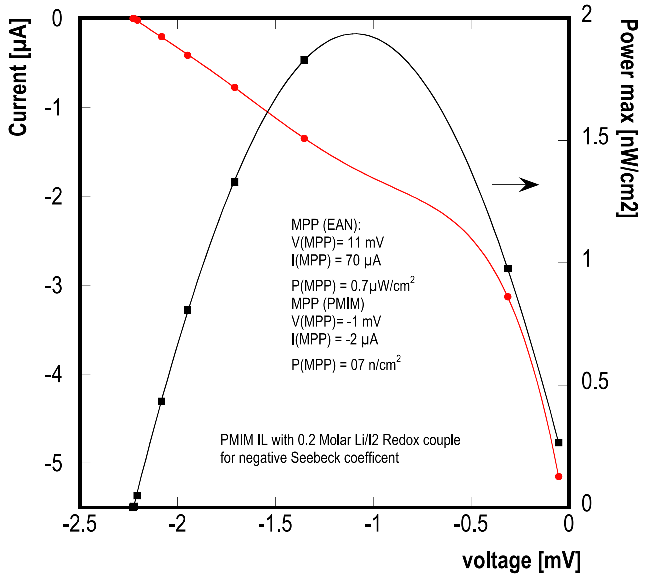

Fig. 19: V-I-P characteristics of the negative S_E-partner in the thermoelectric module. These properties limit the overall performance of the EAN part.

IV. CONCLUSION

Ionic liquids are interesting candidates as thermoelectric materials because their thermal conductivity is 5 to ten times smaller as compared to solid-state materials. This is a typical property of liquids in general. A high thermal conductivity means that for a given heat-flow only a small temperature difference can be generated across the material ending in strongly reduced generator voltages. Ionic liquids present a large new variety of substances, creating space for optimization and new developments. It is concluded in this paper that the current is the principal remaining bottleneck for further conversion efficiency increase. One way out is given by further optimizing redox couples that allow in a cyclic process carrier exchange with the electrodes at low energy. A further way out is just heating of the entire device; heating overcomes the activation energy for increasing the bulk conductivity and for carrier exchange between the liquid and the electrodes. It was found that an increase of the heat-flow of 3.5 times lead to an increase of the electrical power of 77 times.

An issue is the encapsulation of the ILs. The advantage of choosing liquids in combination with polymers appears to be ideal looking at manufacturing of highly flexible generators; however long-term sealing and bubble-free packaging is not straightforward. In this paper the first result on a successfully serial connected IL-based TEG is presented, whereby all process steps could be solved. ILs exhibit positive and negative Seebeck coefficients; this is principally favorable for obtaining higher voltages, however at present the values of the internal resistance negative S_E ILs are by far too high and more effort must be done in order to “match” them with positive S_E ILs.

ACKNOWLEDGEMENTS

The authors acknowledge the financial support of the 'Polish-Swiss-Research Programme' for the project ''ENERLIQ" (Grant number: PSPB-051/2010) in collaboration with Gdansk University of Technology in Poland, and by the Swiss Federal Office of Energy and the Swiss Space Center.

REFERENCES

[1] M. Belleville, E. Cantatore, H. Fanet, P. Fiorini, P. Nicole, M. Pelgrom, C. Piquet, R. Han, C. van Hoof, Ruud Vullers, M. Tartagni. "Energy Autonomous Systems: Future Trends in Devices, Technology, and Systems, CATRENE, 2009

[2] www.micropelt.com, www.nextreme.com, www.eureca.de, www.marlow.com

[3] S. Kim, J. We, B. Cho. "A wearable thermoelectric generator fabricated on a glass fabric", Energy&Environmental Science, 7, pp.1959-1965, 2014.

[4] G. Sevilla, S. Inayat, J. Rojas, A. Hussain, M. Hussain. "Flexible and Semi-Transparent Thermoelectric Energy Harvester from Low Cost Bulk Silicon (100)", Communications: Energy Harvesters, Small 2013, 9, no. 23, pp. 3916-3921, 2013

[5] S. Jo, M. Kim, M. Kim, H. Kim, Y. Kim. „Human Body Heat Energy Harvesting Using Flexible Thermoelectric Generator For Autonomous Microsystems", 16th International Conference on Miniaturized Systems for Chemistry and Life Sciences, Oct. 28 – Nov. 1 Okinawa, Japan, pp. 839-841, 2012

[6] V. Leonov. "Energy Harvesting for Self-Powered Wearable Devices", Wearable Monitoring Systems, pp. 27-49, 2011

[7] W. Glatz, E. Schwyter, L. Durrer, C. Hierold. "Bi2Te3-Based Flexible Micro Thermoelectric Generator With Optimized Design", Journal of Microelectromechanical Systems, vol. 18, no. 3, pp. 763-772, 2009

[8] M. Valkenburg, R. Vaughn, M. Williams, J. Wilkes. "Thermochemistry of ionic liquid heat-transfer fluids", Thermochimica Acta 425, pp. 181-188, 2005

[9] S. Uhl, E. Laux, T. Journot, L. Jeandupeux, J. Charmet, H. Keppner. "Development of Flexible Micro-Thermo-electrochemical Generators based on Ionic Liquids", Journal of Electronic Materials, pp. 3758-3764, 2014

[10] A. Homsy, E. Laux, L. Jeandupeux, J. Charmet, R. Bitterli, C. Botta, Y. Rebetez, O. Banakh, H. Keppner. "Solid on liquid deposition, a review of technological solutions", Microelectronic Engineering 141, pp. 267-279, 2014

[11] V. Leonov. "Chapter 2 Energy Harvesting for Self-Powered Wearable Devices", Wearable Monitoring Systems, DOI 10.1007/978-1-4419-7384-9_2, p. 29, 2011

[12] W. Park, M. Barako, A. Marconnet, M. Asheghi, K. Goodson. "Effect of Thermal Cycling on Commercial Thermoelectric Modules", IEEE, Thermal and Thermomechanical Phenomena in Electronic Systems, pp. 107-112, 2012

[13] H. Keppner, S. Uhl, E. Laux, L. Jeandupeux, J. Tschanz, T. Journot. "Ionic Liquid-based Thermoelectric Generator: Links between Liquid Data and Generator Characteristics", Materials Today: Proceedings 2, pp. 680-689, 2015

[14] E. Laux, S. Uhl, T. Journot, J. Brossard, L. Jeandupeux, H. Keppner. "Aspects of protonic ionic liquid as electrolyte in thermoelectric generators", Journal of Electronic Materials: Conference Proceedings ICT & ECT, pp 1-7, 2016

Journal of Energy Challenges
and Mechanics
http://www.nscj.co.uk/JECM/

ISSN 2056-9386
Volume 3 (2016) issue 2, article 2

High efficiency perovskite/crystalline silicon thin-film tandem solar cell from a highly textured MgO [111] buffered glass substrate: a proposal

来自于高度织构氧化镁[111]缓冲玻璃基板的高效率钙钛矿/结晶硅薄膜串列式太阳能电池：一个建议

Ashok Chaudhari[1*]

[1]*Solar-Tectic LLC, 416 Long Hill RD E, Briarcliff Manor, NY 10510, United States*

solartectic@gmail.com

Accepted for publication on 27 July 2016

Abstract - **In this paper, a proposal for high-efficiency perovskite/crystalline silicon thin-film tandem solar cells is presented. The proposal is based on the successful fabrication of a highly textured MgO [111] thin-film on a glass substrate which is a promising indicator for the successful growth of highly textured (c-axis aligned) silicon films on which textured perovskite films can then be deposited for high-efficiency tandem solar cells.**

Keywords – **perovskite solar cells, thin-film crystalline silicon solar cells, MgO substrates.**

I. INTRODUCTION

In today's solar cell market high power conversion efficiency (PCE) is the most important factor in any photovoltaic technology.[i] It was only recently that cost was considered to be the primary factor, and of course it still remains paramount, but PCE may now even be something manufacturers will pay extra for because efficiency lowers the balance of system costs (BOS) and therefore the overall price per Watt installed (currently at $3.00 USD per Watt without subsidies with the goal of $1.00).[ii] Ideally, both factors – PCE and low cost -- can be achieved, and here a proposal to accomplish this by fabricating a perovskite/crystalline silicon thin-film tandem solar cell is presented for the first time. To date, to the best of our knowledge, there have been no proposals or reports on a perovskite/silicon thin-film tandem solar cell device whether amorphous thin-film silicon or crystalline thin-film silicon.

II. BACKGROUND

Recently papers were published by Solar-Tectic LLC[iii] reporting the growth of a highly textured MgO [111] film on soda-lime glass,[iv] crystalline Al_2O_3 on this same MgO substrate,[v] and silicon film growth also on this MgO/soda-lime glass substrate.[vi] Additionally, a paper was published reporting crystalline silicon film growth on glass without an MgO buffer layer, where the glass was a flexible glass made by a leading glass manufacturer.[vii] While these papers prove that inexpensive deposition of crystalline silicon thin-films on ordinary glass is possible, their efficiency when converted to solar cells will be necessarily limited by the single absorber layer. This is true even if a single crystal thin-film of silicon without defects could be grown on glass, a long standing objective in the materials research community, which remains to be accomplished.[viiiix]

Also recently, much attention within the solar cell community has been focused on a relatively new material called perovskites, specifically metal halide organic-inorganic hybrid perovskites. It has been suggested that a tandem solar cell consisting of a silicon sub-cell layer (of wafer thickness) combined with a perovskite layer would provide a solution to solving both the efficiency and cost problems which are keeping solar energy from truly competing with fossil fuels, without subsidies.[x] Here we propose an alternative which is potentially less expensive, non-toxic, and equally efficient to a perovskite/silicon wafer tandem solar cell structure of the kind proposed thus far: a tandem solar cell consisting of a thin-film of crystalline silicon on soda-lime glass and perovskite film

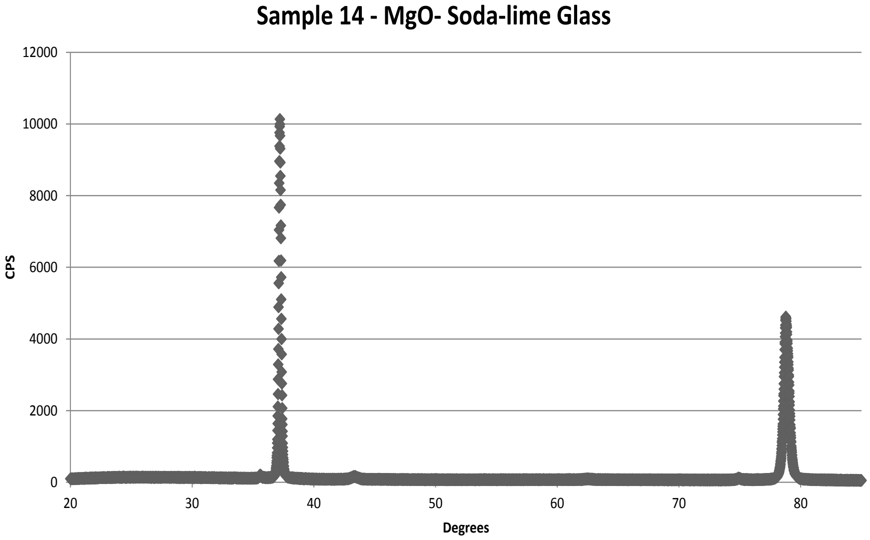

Fig.1, XRD of 7µm MgO [111] on soda-lime glass with associated- [222] peak at ~78 dgrees.

grown on this film for a planar heterojunction high efficiency solar cell. Following the recipe (recently patented) of the late Dr. Praveen Chaudhari, a textured silicon film is grown on an MgO [111] buffered soda-lime glass substrate from a silicon-tin eutectic melt and a tandem solar cell is formed by the addition of a layer of another material with better light conversion efficiency, i.e. with a higher bandgap. In the new process disclosed here for the first time by Solar-Tectic LLC (patent pending) the Sn from the Si-Sn eutectic alloy melt which has segregated on the surface of the crystalline silicon film after deposition is then used as the metal in the perovskite structure thus replacing the toxic lead, and facilitating a planar heterojunction device formation for high efficiency, low cost.

In the following pages, data will be provided regarding the first and second steps in this architecture, namely the MgO [111] on glass substrate and the crystalline silicon film grown on it; and in the second half of the paper a proposal regarding the third and final step – the deposition of the perovskite film on the crystalline silicon film, will be described, though many details remain and this is only an introduction to a new process invented which will be developed.

III. STEP 1: TEXTURED MGO [111] FILM ON SODA-LIME GLASS

For the perovskite/crystalline silicon tandem solar cell a textured buffer layer that serves as a diffusion barrier for the soda-lime glass, preventing glass impurities from entering the silicon, as well as a template to induce texture in the silicon film, is preferable as it is known than textured materials have distinct electronic advantages, and this includes perovskites.[xixii] Although the MgO [111] film on glass is highly transparent (see figure 2), transparency is not a requirement for the device architecture since light must enter first through the top perovskite layer which has the higher bandgap. It is the combination of the higher bandgap perovskite with the lower bandgap silicon that allows for higher voltage and PCE.

The textured MgO [111] film on glass serves the purpose of the required buffer layer for the tandem device. As already stated a previous paper reported the successful deposition of the MgO [111] film on soda-lime glass, and here we present some additional data regarding this accomplishment which has not been made public until now. Figure 1 shows a second XRD that was performed on the same sample as reported on in the previous paper, but includes the associated parallel [222] peak thereby indicating and/or confirming that a good crystalline formation (better than if there had only been one [111] peak) was obtained. To further investigate the quality of the crystalline MgO [111] film, TEM was performed (see figure 3) clearly evidencing alignment or high texture. A rocking curve was also performed on a highly textured (almost perfectly aligned) sample of 3µm MgO [111] film deposited on a quartz substrate at 800°C using the same invented process[xiii]. This particular sample was chosen because of the near perfect alignment and thinner film, and it showed a large FWHM (see figures 4 and 5).

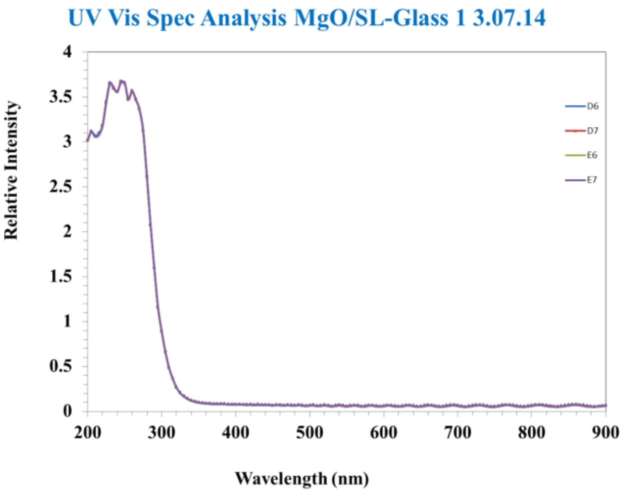

Figure 2: Transparency of MgO on glass. The layer here is 7µm thick and shows high transparency, or ~99%.

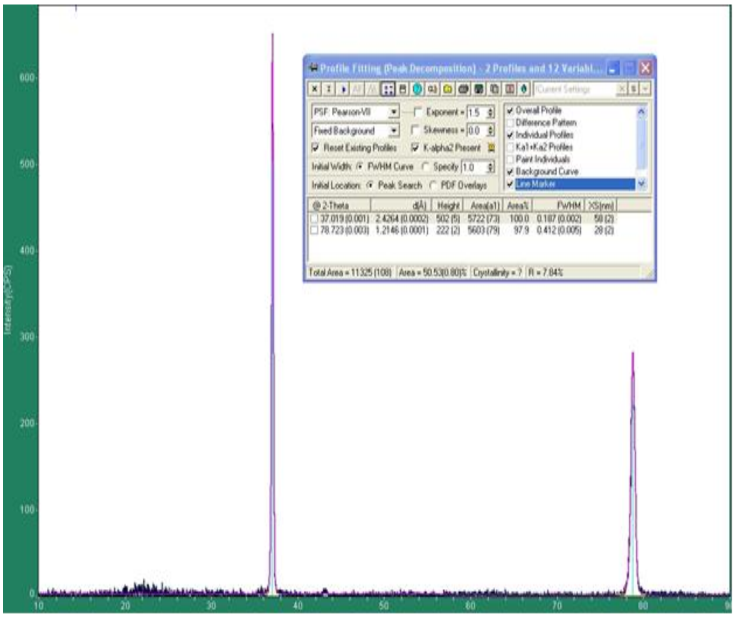
Profile Fitting (Peak Decomposition) - 2 Profiles and 12 Variabl...

PSF: Pearson-VII
☐ Exponent = 1.5
Fixed Background
☐ Skewness = 0.0
☑ Reset Existing Profiles
☑ K-alpha2 Present
Initial Width: ● FWHM Curve ○ Specify 1.0
Initial Location: ● Peak Search ○ PDF Overlays

☑ Overall Profile
☐ Difference Pattern
☑ Individual Profiles
☐ Ka1+Ka2 Profiles
☐ Paint Individuals
☑ Background Curve
☑ Line Marker

@ 2-Theta	d(Å)	Height	Area(a1)	Area%	FWHM	XS(nm)
☐ 37.019 (0.001)	2.4264 (0.0002)	502 (5)	5722 (73)	100.0	0.187 (0.002)	58 (2)
☐ 78.723 (0.003)	1.2146 (0.0001)	222 (2)	5603 (79)	97.9	0.412 (0.005)	28 (2)

Total Area = 11325 (108) | Area = 50.53(0.80)% | Crystallinity = ? | R = 7.84%

Fig.4: XRD of 3µm of MgO [111] on quartz. No peaks besides the MgO [111] and MgO [222] parallel peak (at ~78 degrees) are visible indicating near perfect out-of-plane or c-axis alignment.

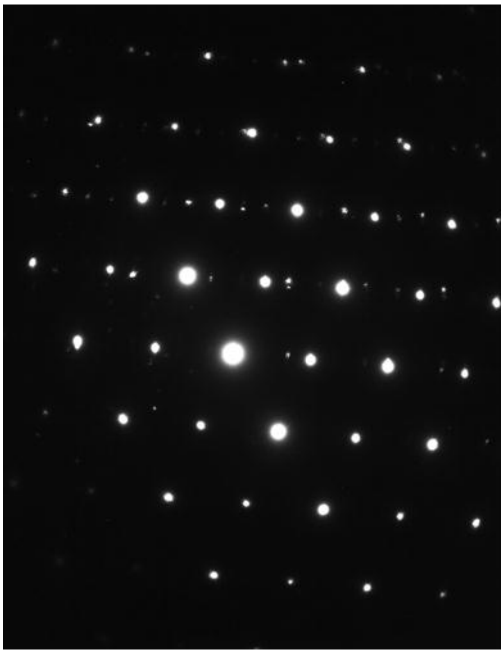

Figure 3: Selected area diffraction from TEM of 7µm MgO [111] film on soda-lime glass showing a c-axis aligned or highly oriented [111] film was grown directly on glass.

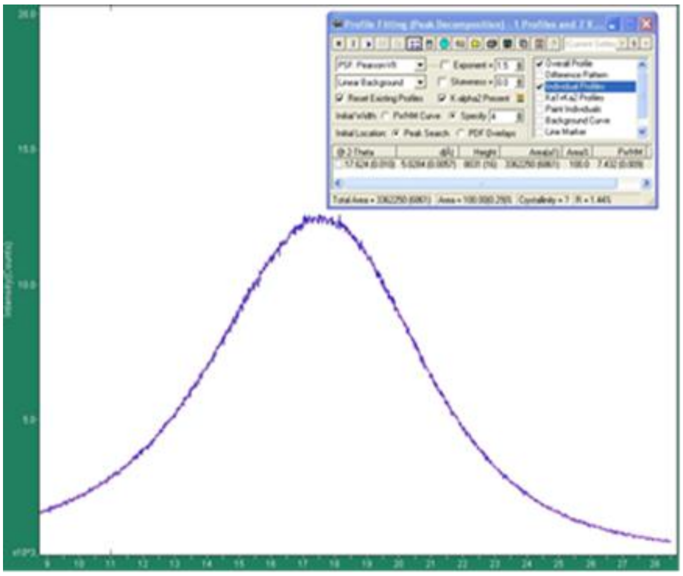

Fig.5, Rocking Curve of 3µm MgO [111] on quartz at 800°C 7.4 degrees.

It was hypothesized that higher temperature may improve the crystalline quality compared to the sample reported on in the previous paper since generally crystallinity of materials improves with higher temperature. It was therefore considered to be a "best case" scenario. The FWHM of the rocking curve indicates the range of tilt angles through which the MgO 111 planes are oriented, which was determined to be 7.4 degrees, a wide range. For comparison, single crystals usually give a FWHM of 0.1 deg. using the same configuration. Additional investigation and a rocking curve of the 7µm MgO [111] film on soda-lime glass samples reported on the previous paper is planned in the near future.

IV. STEP 2: CRYSTALLINE SILICON DEPOSITION ON THE MGO/SODA-LIME GLASS SUBSTRATE.

For deposition of thin-films on a textured substrate from a eutectic alloy melt, the energetics of the interface with the substrate and/or the vacuum or gas must be considered, and it is not only the chemical interaction of the metal or Si with the substrate that is important but also its crystallographic orientation. This is because the surface or interface energy depends upon orientation of the grains.[xiv] Here the MgO has a strong texture which is [111] oriented, and should therefore be advantageous to silicon [111] film growth. However, another concern is the difference in lattice match between the nucleating film and the substrate which can lead to strain induced energy that is minimized by either inducing defects or not growing uniformly in thickness across the substrate surface. There is a lattice mismatch between MgO and silicon that may be adverse to achieving high quality films. MgO has a lattice constant of 4.212Å and silicon 5.431 Å. These factors determine if silicon is likely to deposit on the substrate (heterogeneous nucleation) or nucleate and form small crystals in the liquid (homogenous nucleation).[xv]

When considering the texture of the MgO on glass, it is important to determine whether it is uniaxial or biaxial. In other words, whether it has in-plane or out-of-plane texture. In order to determine this, EBSD was performed on the samples, presented here for the first time. It was clear (see figure 6) that the sample was highly textured [111] out-of-plane. It was also evident that there was little or no in-plane texture, which is not surprising since the films were deposited on an amorphous substrate without ion beam assistance. It should be noted that it is well known that MgO films with both in-plane and out-of-plane texture can be grown using ion beam assisted deposition (IBAD). But this process is more expensive than the process we report on here. Moreover, it is not clear that biaxial orientation and epitaxy would be necessary in the process since epitaxial growth with both in-plane and out-of-plane texture is not always necessary and preferentially oriented polycrystalline films are often sufficient.[xvi] Also, if one looks at this process as a kind of Vapor-liquid-solid thin-film process (VLS-TF) where the film is essentially a nanowire-like, and therefore -- because nanowires are single crystal -- single crystal-like thin-film, which depends more on the out-of-plane crystallographic orientation of the film for growth (necessarily the case with nanowire growth), one can see how in-plane texture may not be so important.[xvii] Also, with nanowire growth the [111] direction is crucial. (For details on this VLS-TF process by P. Chaudhari please see McMahon et al, "Textured [111] crystalline silicon thin film growth on flexible glass by e-beam evaporation"). Indeed, it may be for this reason that the film growth reported on in a recent paper where silicon was deposited on the MgO/glass substrate was not oriented as thought. It was polycrystalline but there was no texture. Initial XRD scans seemed to indicate the film was textured, as there was only one silicon peak in the XRD, but TEM later showed the film to be polycrystalline (see figure 7) without oriented silicon. We reason that the lack of orientation could be due to the amount of Al that was used. Too much Al would prohibit nanowire-like film growth and would not lead to oriented film growth, failing to replicate the high texture in the MgO substrate clearly evidenced in the XRD. On the other hand, the process disclosed by P. Chaudhari is probably closer to a modified liquid-phase epitaxy method. And therefore it may be necessary to grow biaxially textured substrates in order to obtain the quality of crystallinity that is the aim of his invention, and indeed is a part of the prescription. However, the plan view TEM of the same sample, presented here for the first time (see figure 8), showed a completely continuous film with crystals of various sized completely covering the MgO substrate and no pinholes. The film was etched to remove the Al from the Si film.

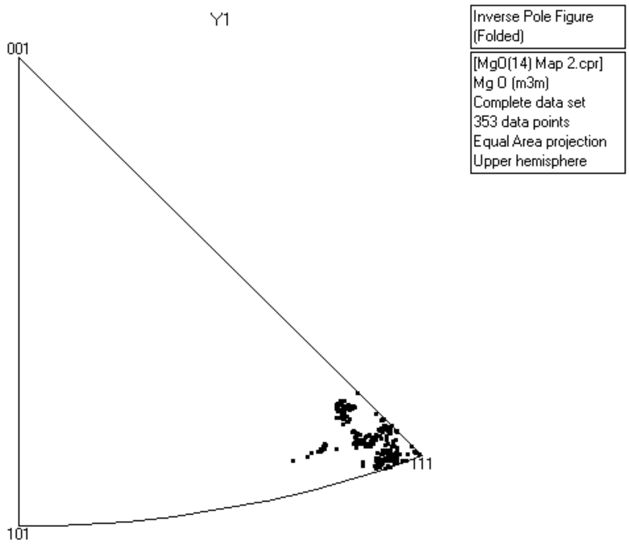

Figure 6: Inverse pole figure from EBSD confirming a highly oriented [111] MgO crystalline film has been grown.

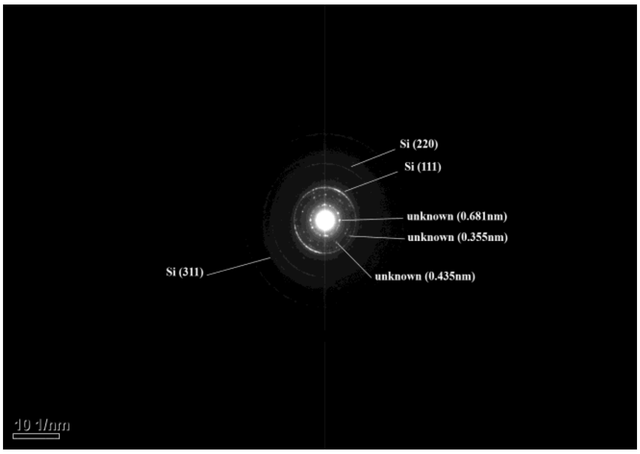

Figure 7: TEM SAED diffraction pattern showing a polycrystalline Si film with perhaps some in-plane orientation but otherwise no texture, despite the strong intensity of the [111]. (Cornell University, CCMR, 2016).[xviii]

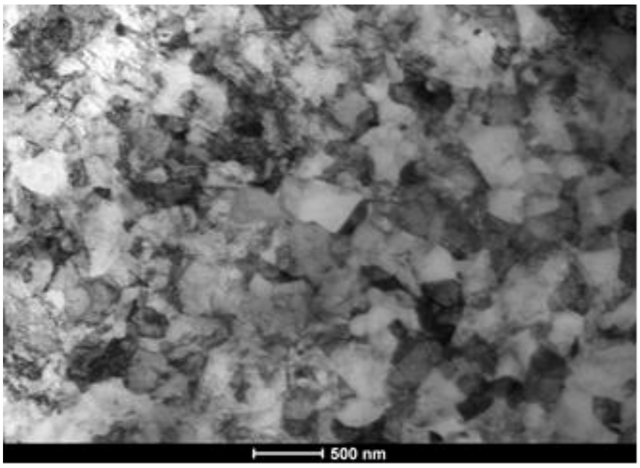

Figure 8: Plan view TEM of same sample as in figure 7, showing a completely continuous Al etched polycrystalline Si film covering the MgO/glass substrate. No pin holes are evident. (Cornell University, CCMR, 2016).[xix]

V. STEP 3: PEROVSKITE FILM GROWTH ON THE SI FILM.

As already stated, solar cell efficiency is now of primary importance and in fact also lowers overall costs since the BOS costs are reduced with increased PCE. Many now believe that the best way to achieve a highly efficient and cost effective solar cell is by fabricating a tandem (or multi-junction) solar cell, consisting of two layers, where one layer has a bandgap higher than the other, and the layers work in tandem towards higher efficiency light conversion. The question is which materials should be used for this structure. Silicon has a near ideal bandgap for a sub-cell (1.1eV),[xx] and the more difficult question is which material should be used for the top layer (with higher bandgap). Interestingly, there is only one example found in the literature of a tandem solar cell consisting of crystalline thin-film silicon layer, and it is with germanium (on the bottom). A proposal and simulation for this was reported with maximum efficiencies of 28% predicted.[xxi] However, very recently, perovskites have gained much attention due to the rapid increase in efficiency from just 3.8% in 2009 to over ~20% at present. It has been suggested that combining perovskites with silicon for a tandem cell is a viable way to gaining market entry in a silicon wafer dominated industry; and initial tandem device models predict that 36% to 37% efficiencies are achievable for perovskite/silicon tandems.[xxii] However, these are not thin-film devices since the Si is wafer thickness or fabricated by the same process as Si wafers, namely at very high temperatures.

For a thin-film crystalline Si tandem solar cell, a perovskite top absorber layer is an attractive material because perovskites are easy and cheap to make.[xxiii] But there are several significant problems that prevent perovskites entry into the market place at this point[xxiv]. One such problem is the use of Pb (lead) as the main metal, which is toxic. Here we present a solution to this problem by replacing lead with Sn (tin) in a tandem structure. This has actually been demonstrated before in a perovskite solar cell,[xxv] but not with a thin-film crystalline Si under layer. A crystalline Si under-layer can be deposited at low temperature using eutectics and requires much less material[xxvi]. It is therefore is less expensive than c-Si wafers. So far the only tandem solar cell reported which used crystalline thin-film Si as an under-layer was with a P3HT (polymer).[xxvii] Here for the first time we propose a process that uses Sn as the metal catalyst for low temperature crystalline silicon thin-film growth that not only makes use of the highly efficient perovskite material combined with silicon, but in using a thin-film of silicon rather than a wafer, additional cost savings are achieved since less silicon material is needed. Moreover, by using a Sn-Si eutectic alloy (rather than the more common Al-Si used in Aluminum Induced Crystallization) to deposit the silicon at low temperature on the MgO [111] buffered glass, the Sn can be used as the metal (the “B” in ABX_3) in the perovskite material, thus avoiding the otherwise necessary step of etching the Sn from the surface of the silicon layer. The process is simple, and can take place at low temperature – a crucial advantage often cited in connection with perovskite technology too -- using known deposition methods and non-toxic materials and processes throughout. Depositing the silicon film by e-beam evaporation avoids the costly and dirty manufacturing process associated with silicon wafers, both polycrystalline and monocrystalline. Since silicon has a global market share of about 90%, there is obviously a huge market potential for silicon thin-films with comparable quality to c-Si but with additional efficiency (beyond the 25.6% Si wafer current record) due to the tandem perovskite layer.[xxviii][xxix] And this holds true for any material with a higher bandgap such as CZTS which is another contender for a top layer due to its high bandgap as well as closely matching lattice parameter with that of silicon.

As for details of the perovskite material, the family of perovskite materials adopt the chemical formula ABX_3, where A and B are cations of dissimilar sizes, and X are anions. B is the metal cation and would in this case be Sn instead of Pb.[xxx] Either a hybrid perovskite (organic-inorganic) or a non-organic perovskite material can be used, though it is known that the non-organic perovskites have bandgaps that are too large for high PCE.[xxxi] Therefore, a likely material would look like $MASnI_3$. And the deposition process for combining the MA and I_3 with the Sn would be that known in the art and involve common processes, and while this requires much more development and detailed investigation, there is reason to be optimistic because perovskites are versatile and there is room for various configurations.

The versatility of perovskites makes them highly attractive as they can form multidimensional structures pertaining to the same chemical formula through use of different combinations of various components. There is therefore flexibility as to the exact perovskite compound.[xxxii] They are known to easily form solar cells layers. “One of the real beauties of perovskite is it almost doesn’t care how you make it. Put a few drops of perovskite precursor, in liquid form, on a piece of aluminum foil on your desk; leave it to evaporate for a day; then plug in a metal probe and you have an operating PV cell — cruddy output, but output nonetheless” as one industry expert put it, perhaps somewhat unscientifically![xxxiii]

Despite the seeming ease of fabricating perovskite films described above, there are potential hurdles. The B metal cation sites in hybrid perovskites are occupied by the group IVA metals in a divalent oxidation state (Pb2+, Sn2+, Ge2+). Lead (Pb) has proven the superior constituent compared to tin (Sn), both in terms of performance and stability, and consequentially has been the most widely employed of the group IVA metals.[xxxiv] In the new process presented here, one concern is this issue of Sn stability. Another issue is how exactly the remaining components of the perovskite structure would be combined with the Sn layer on Si. Finally, if there are any impurities in the Sn from the Si (per Si-Sn eutectic melt), how will this affect the perovskite material?

As far as the solar cell structure is concerned, planar heterojunction perovskite/silicon solar cells have already been achieved. And they can be made with an electron transport layer between the silicon and the perovskite, or without. For example, a perovskite/silicon multi-junction solar cell may also be constructed via monolithic integration where a thin film perovskite sub-cell is deposited directly onto the c-Si sub-cell without a recombination layer.[xxxv] In the case of the process we propose here the Sn on the surface of the silicon (the Sn segregates to the surface of the Si film in the process) film can be oxidized to form a SnO_2 electron transport layer onto which the perovskite film is then deposited. SnO_2 has already been proven to be a viable substitute for the common TiO_2.[xxxvi] This SnO_2 film is also likely to have texture if the underlying silicon film does.

While texture would be advantageous, it is not necessary for an efficient perovskite layer. Textured crystalline silicon and perovskite layers in a tandem cell would however be likely to have improved efficiencies as it is known that in order to achieve highly efficient perovskite layers good quality crystallinity is key. That is, crystallization of the perovskites, including the orientation, grain size, and morphology, determines the device performance of perovskite solar cells[xxxvii]. There has been one report of textured perovskite growth.[xxxviii] However, at the present time, there are no reports of any perovskite/crystalline or amorphous silicon thin-film results (or patent applications). And this includes both a-Si and crystalline Si from aluminum induced crystallization. Work has however been done on perovskite/thin –film CIGS tandem structures[xxxix]. Yet a crystalline silicon thin-film would have many advantages over CIGS, not least because CIGS uses selenide (H_2Se) which is highly toxic. Also the manufacturing process is much more complicated than the crystalline silicon thin-film deposition process reported on here which is a straightforward e-beam or CVD (or HW-CVD) deposition method already used widely in the display industry, for example.

III. CONCLUSION

In conclusion, additional characterizations of the MgO [111] film growth on soda-lime glass have been provided, confirming the high texture growth, but also clarifying the texture is limited to out-of-plane or uniaxial as per EBSD results and analysis. Also, further investigation and analysis of the rocking curve (FWHM) should be undertaken and its significance reported. Secondly, further characterizations of the crystalline silicon film grown on this MgO [111] film have been reported and have clarified that in fact the Si film is likely not textured as originally thought, though it is polycrystalline and TEM showed that it is completely continuous even after etching of the Al. Such a film, if deposited using Sn instead of Al at the catalyst, could serve as the bottom layer in a tandem cell where perovskite film could be deposited. Moreover, the Sn segregated on the Si film could be used to form the $MASnI_3$ material thus saving the step of etching the Sn and also perhaps improving the perovskite material. Such a perovskite/crystalline silicon thin-film solar cell could be an even better solution than the current perovskite/c-Si design recommended by a number of groups, since lower temperature processing could be sufficient all around, not just for the perovskite film. Details of this proposal will be reported on as R&D commences in the near future.

REFERENCES

---

[i] C. Bailie and M. McGehee, "High efficiency tandem perovskite solar cells" MRS Bulletin, vol. 40, August 2015.

[ii] R. Martin, "Wind and Solar Will Be the Cheapest Way to Generate Power by 2040" MIT Technology Review, June 13, 2016.

[iii] Solar-Tectic LLC is a start-up based primarily on the technologies invented by the late Dr. Praveen Chaudhari, winner of the 1995 US National Medal of Technology.

[iv] A. Chaudhari, R.D. Vispute, H. Efstathiadis, "Extremely highly textured MgO [111] crystalline films on soda-lime glass by e-beam", Materials Letters 121 (2014) 47-49.

[v] A. Chaudhari, R.D. Vispute, T. Murray, H. Efstathiadis, "Crystalline Al_2O_3 on buffered soda-lime glass by e-beam", Materials Letters 136 (2014) 407-410.

[vi] S. McMahon, A. Chaudhari, H. Efstathiadis, "Highly textured silicon [111] crystalline thin-film on buffered soda-lime glass by e-beam evaporation", Materials Letters 140 (2015) 123-126.

[vii] S. McMahon, A. Chaudhari, Z. Zhao, H. Efstathiadis, "Textured [111] crystalline silicon thin film growth on flexible glass by e-beam evaporation", Materials Letters 158 (2015) 269-273.

[viii] K. Chen, R. Kapadia, A. Harker, S. Desai, J.S. Kang, S. Chuang, M. Tosun, C.M. Sutter-Fella, M. Tsang, Y. Zeng, D. Kiriya, J. Hazra, S.R. Madhvapathy, M. Hettick, Y.Z. Chen, J. Mastandrea, M. Amani, S. Cabrini, Y.L. Chueh, J.W. Ager, "Direct growth of single-crystalline III-V semiconductors on amorphous substrates", Nature Communications DOI:10.1038, 2016.

[ix] S. Kühnapfel, S. Gall, B. Rech, D. Amkreutz, "Towards monocrystalline silicon thin films grown on glass by liquid phase crystallization", Solar Energy Materials & Solar Cells 140 (2015) 86-91.

[x] V. Sivaram, S. Stranks, H.J. Snaith, "Outshining silicon: An upstart material – perovskite – could finally make solar cells that are cheaper and more efficient than the prevailing silicon technology" Scientific American, July 2015.

[xi] M. Yang, Y. Zhou, Y. Zeng, C.S. Jiang, N. Padture, "Square-centimeter solution processed planar Ch3NH3Pbl3 perovskite solar cells with efficiency exceeding 15%", Adv. Mater. 2015.

[xii] C. Teplin, D.S. Ginley, H.M. Branz, "A new approach to thin film crystal silicon on glass:Biaxially-textured silicon on foreign template layers", Journal of Non-Crystalline Solids 352 (2006) 984–988.

[xiii] For details of the process see R.D. Vispute et al "Methods of producing large grain or single crystal films" (US 2014/0245947, patent pending).

[xiv] P. Chaudhari, "Methods of Growing Heteroepitaxial Single Crystal or Large Grained Semiconductor Films and Devices Thereon", US Patent 9,054, 249. 2015.

[xv] P. Chaudhari, "Methods of Growing Heteroepitaxial Single Crystal or Large Grained Semiconductor Films and Devices Thereon", US Patent 9,054, 249. 2015.

[xvi] J. Beeckman, J.P. George, K. Neyts, D.V. Thourhout, "Ferroelectric thin films on silicon and glass for optical applications", IC1208, September, 2014.

[xvii] P. Chaudhari, H. Shim, B.A. Wacaser, M.C. Reuter, C. Murray, K.B. Reuter, J. Jordan-Sweet, F.M. Ross, S. Guha, "Heteroepitaxial silicon film growth at 600°C from an Al-Si eutectic melt", Thin Solid Films 518 (2010) 5368-5371.

[xviii] This image was made at Cornell University's Center for Materials Research (CCMR), by Don Werder, in 2016.

[xix] This image was made at Cornell University's Center for Materials Research (CCMR), by Don Werder, in 2016.

[xx] C. Battaglia, A. Cuevas, S. De Wolf, "High-efficiency crystalline silicon solar cells: status and perspectives" Energy Environ. Sci. 2016, 9, 1552.

[xxi] G. Sun, F. Chang, R.A. Soref, "High efficiency thin-film crystalline Si/Ge tandem solar cell", Optics Express, Vol. 18, No.4, 15 February 2010.

[xxii] C. Ballie and M. McGehee, "High efficiency tandem perovskite solar cells" MRS Bulletin, vol. 40, August 2015.

[xxiii] V. Sivaram, S. Stranks, H.J. Snaith,"Outshining silicon: An upstart material – perovskite – could finally make solar cells that are cheaper and more efficient than the prevailing silicon technology" Scientific American, July 2015.

[xxiv] K. Chen, R. Kapadia, A. Harker, S. Desai, J.S. Kang, S. Chuang, M. Tosun, C.M. Sutter-Fella, M. Tsang, Y. Zeng, D. Kiriya, J. Hazra, S.R. Madhvapathy, M. Hettick, Y.Z. Chen, J. Mastandrea, M. Amani, S. Cabrini, Y.L. Chueh, J.W. Ager, "Direct growth of single-crystalline III-V semiconductors on amorphous substrates", Nature Communications DOI:10.1038, 2016.

[xxv] N. Noel, S. Stranks, A. Abate, C. Wehrenfennig, S. Guarnera, A-A. Haghighirad, A. Sadhanala, G.E. Eperon, S.K. Pathak, M.B. Johnston, A. Petrozza, L.M. Hertz, H.J. Snaith, "Lead-free organic-inorganic tin hailde perovskites for photovoltaic applications", Energy Environ. Sci. 2014, 7, 3061.

[xxvi] C. Teplin, D. Ginley, H.M. Branz, "A new approach to thin film crystal silicon on glass:Biaxially-textured silicon on foreign template layers", Journal of Non-Crystalline Solids 352 (2006) 984–988.

[xxvii] A. Zellmeier, S. Kuhnapfel, B. Rech, N.H. Nickel, J. Rappich, "Enhanced stability of P3HT/poly-crystalline Si thin film hybrid solar cells", Phys. Status Solidi A, 1–5 (2016).

[xxviii] C. Battaglia, A. Cuevas, S. De Wolf "High-efficiency crystalline silicon solar cells: status and perspectives" Energy Environ. Sci. 2016, 9, 1552.

[xxix] V. Sivaram, S. Stranks, H.J. Snaith, "Outshining silicon: An upstart material – perovskite – could finally make solar cells that are cheaper and more efficient than the prevailing silicon technology" Scientific American, July 2015.

[xxx] Q. Chen, N. De Marco, Y.M. Yang, T-B Song, C-C. Chen, H. Zhao, Z. Hong, H. Zhou, Y. Yang, "Under the spotlight: The organic—inorganic hybrid halide perovskite for optoelectronic applications "Nano Today (2015) 10, 355—396.

[xxxi] Q. Chen, N. De Marco, Y.M. Yang, T-B Song, C-C. Chen, H. Zhao, Z. Hong, H. Zhou, Y. Yang "Under the

---

spotlight: The organic—inorganic hybrid halide perovskite for optoelectronic applications “Nano Today (2015) 10, 355—396.

[xxxii] Q. Chen, N. De Marco, Y.M. Yang, T-B Song, C-C. Chen, H. Zhao, Z. Hong, H. Zhou, Y. Yang “Under the spotlight: The organic—inorganic hybrid halide perovskite for optoelectronic applications “Nano Today (2015) 10, 355—396.

[xxxiii] D. Snieckus “Could this be solar's next big breakthrough?” RECHARGE magazine, June 03 2016.

[xxxiv] Ibid.

[xxxv] J. Mailoa, C. Bailie, E.C. Johlin, E.T. Hoke, A.J. Akey, W.H. Nguyen, M.D. McGehee, T. Buonassisi, “A 2 terminal perovskite/silicon multijunction solar cell enabled by a silicon tunnel junction”, Applied Physics Letters 106, 121105 (2015).

[xxxvi] W. Ke, G. Fang, Q. Liu, L. Xiong, P. Qin, H. Tao, J. Wang, H. Lei, B. Li, J. Wan, G. Yang, Y. Yan, “Low-Temperature Solution-Processed Tin Oxide as an Alternative Electron Transporting Layer for Efficient Perovskite Solar Cells”, J. Am. Chem. Soc. 2015, 137, 6730−6733.

[xxxvii] Z.K. Wang, X. Gong, M. Li, Y. Hu, J-M. Wang, H. Ma, L-S. Liao, “Induced crystallization of perovskites by a perylene underlayer for high performance solar cells”, ACS Nano 2016, 10, 5479−5489.

[xxxviii] M. Yang, , Y. Zhou, Y. Zeng, C.S. Jiang, N. Padture “Square-centimeter solution processed planar $Ch_3NH_3PbI_3$ perovskite solar cells with efficiency exceeding 15%”, Adv. Mater. 2015.

[xxxix] L. Kranz, A. Abate, T. Feurer, F. Fu, E. Avancini, J. Lockinger, P. Reinhard, S.M. Zakeerruddin, M. Gratzel, S. Buecheler, A.N. Tiwari, “High-Efficiency Polycrystalline Thin Film Tandem Solar Cells” J. Phys. Chem. Lett. 2015, 6, 2676−2681

Journal of Energy Challenges
and Mechanics

http://www.nscj.co.uk/JECM/

ISSN 2056-9386
Volume 3 (2016) issue 2, article 3

Crude glycerol as substrate for oleaginous yeasts

作为含油酵母基板的粗甘油

Heike Kahr[1*], Manuel Pointner[1], Klaus Krennhuber[1], Alexander Jäger[1]

[1]*School of Engineering and Environmental Sciences, University of Applied Sciences Upper Austria, 4600 Wels, Austria*

Heike.Kahr@fh-wels.at

Accepted for publication on 13th March 2016

Abstract - **Diverse oleaginous yeasts can grow and accumulate lipid on a broad range of competitive substrates. In this study crude glycerol from conventional biodiesel production was used as the substrate for lipid production via oleaginous yeasts. Various cultivation conditions were tested – different C/N ratios, temperatures and addition of salts.**

Candida lipolytica, Yarrowia lipolytica, Trichosporon fermentans **produced up to maximum of 22 % (w/w) lipid relating to the biomass at specific cultivation conditions. Scale up experiments revealed the further challenges of the lipid production via oleaginous yeasts - adhesion of the yeast, production of citric acid, low biomass and lipid yield. The lipid yield was 17 % (w/w) relating to the biomass despite addition of detergent.**

Keywords – **oleaginous yeast, crude glycerol, lipid production.**

I. INTRODUCTION

Conventional biodiesel is produced from diverse sources - from edible plant oils (mainly from rapeseed in Austria) and non-edible plant oils and waste oil. In the future biofuel production should be done with non-food crops, agro-industrial wastes and renewable resources. These substrates will not compete with food and feed production and will avoid a food versus fuel discussion.

The next generation biodiesel production is developed with lipid accumulating microorganisms such as microalgae, bacteria and fungi, especially yeast. The oleaginous yeasts mainly belong to the genera *Yarrowia*, *Candida*, *Rhodotorula*, *Rhodosporodium* and *Cryptococcus* [1] [2] [3].

The oleaginous yeasts convert low cost substrates to lipids, grow quickly to high density, produce lipid year around and can accumulate up to 70% oil by dry matter. The dominant lipids are palmitic acid, palmitoleic acid, stearic acid, oleic acid and linoleic acid - similarly to those detected in plant oils and therefore suitable for biodiesel.

The lipid production via yeasts requires specific cultivation conditions – often carbon excess and nitrogen limitation. But the lipid production via yeast is also influenced by other factors like the yeast species, stage of growth, carbon source and level, aeration rate, temperature, presence of inhibitors, nitrogen source, phosphorus level, thiamine, biotin, pH value and acclimatization to a carbon source [4].

Glycerol is a co-product from the oleochemical industry especially from biodiesel production. The global annual biodiesel production will increase up to over 41 billion litres in the year 2022 [5]. About 1 kg crude glycerol remains from 10 kg of biodiesel from rapeseed oil [6]. Refining this crude glycerol to high purities is too costly and energy-intensive [7].

Several publications exist about the lipid production from crude glycerol via oleaginous yeasts. For instance *Rhodotorula glutinis* converted crude glycerol to 10.05 g/L biomass, 60.6 % (w/w) lipid and 6.1 g L^{-1} lipid yield [8]. The yeast *Yarrowia lipolytica* produced in continuous culture with crude glycerol 3.5 g L^{-1} cellular lipid and 43 % (w/w) lipid [9].

First scale ups, pilot and demonstration plants were built and run during the last century but theses factories were closed because of the inefficient production. The first up to date scale up (200 litres medium containing glycerol) was reported in the year 2014 – here the cultivation of the yeast *Metschnikowia pulcherrima* yields 2.06 g L^{-1} biomass and 34 % lipid (w/w) [10].

We tested the oleaginous potential of diverse oleaginous yeasts using crude glycerol from conventional biodiesel production as substrate. *Yarrowia lipolytica* produced 22 % lipid (w/w) relating to the biomass at specific cultivation conditions. Finally we illustrated the problems with the scale up - adhesion of the yeast, production of citric acid and low biomass and lipid yield.

In future the industrial lipid production via yeast will be feasible with cheap feedstock (like crude glycerol), higher productivity and final higher oil concentrations.

II. MATERIALS AND METHODS

2.1. YEASTS, MEDIA, PRECULTIVATION AND CULTIVATION

The cell growth and lipid accumulation of the yeast species *Candida lipolytica*, *Yarrowia lipolytica* and *Trichosporon fermentans* (kindly provided from the strain collection of the company Agrana (http://www.agrana.at/)) were investigated in this study.

The yeast was precultured in incubator shaker in crude glycerol medium (60 g L^{-1} glycerol, 2 g L^{-1} yeast extract, 2 g L^{-1} peptone, autoclaved at 121°C for 20 minutes) for 24 hours at 180 rpm at 30°C. Furthermore yeast cells were adapted in the crude glycerol medium over a lot of generations.

Screening was done in crude glycerol medium (60 g L^{-1} crude glycerol) with different C/N ratios and sometime with or without salts (2.7 g L^{-1} potassium dihydrogen phosphate, 1.192 g L^{-1} disodium hydrogen phosphate dihydrate, 0.1 g L^{-1} ethylenediaminetetraacetic acid) at 25°C or 30°C with 180 rpm for 7, 10 or 17 days.

2.2. HPLC AND GC-FID ANALYSIS, MAIN IONS AND TRACE ELEMENT ANALYSIS, DETERMINATION OF THE YEAST BIOMASS

Glycerol concentration was quantified by HPLC, using an Agilent Technologies 1200 Series equipped with a Varian Metacarb 87 H column (300x7.8 mm) at 65°C, H_2SO_4 (c = 5 mmol L^{-1}) eluent and an isocratic flow rate of 0.8 mL min^{-1} was used. The data acquisition was performed per refractive index detection and UV detection at 210 nm. For calibration the method of external standard was applied. Data analysis was performed per Agilent Chemstation 04.03 b.

Samples for the determination of main ions by IC were prepared by dilution with the proper mobile phase followed by centrifugation with a rotational speed of 13,000 min^{-1}. The main ionic components of the raw glycerin were determined by a Dionex ICS 1000 ion chromatographic system, equipped with an AS40 auto sampler. Signals were obtained by a conductivity detector. For anions the chromatographic setup was an IonPac AS14A (4x250 mm) separation column, guarded by an IonPac AG14A (4x50 mm) and the suppressor ASRS Ultra II, 4mm from Thermo Fisher.

For cations the chromatographic setup was an IonPac CS12A (4x250 mm) separation column, guarded by an IonPac CG12A (4x50mm) and the suppressor CSRS Ultra II 4 mm from Thermo Fisher. Chromatographic conditions were set up according the columns reference method. As calibration the external standard method was applied. Standard solutions were purchased from Merck Certipur.

Samples for determination of trace elementals by ICP OES were prepared by centrifugation at a rotational speed of 13,000 min^{-1}. The clear supernatant was diluted to a proper factor with nitric acid (TRACE METAL Fisher Scientific, 67-70 %) c = 0.1 mmol L^{-1} in a 50 mL plastic screw tube.

Trace metal concentration was determined by ICP OES from Horiba Jobin Yvonne, ULTIMA2, equipped with an AS 80 auto sampler using the software ICP Analyst 5.2. The argon plasma torch (Air Liquide, >99,999 %) was generated with a power of 1,000 Watt and a flow rate of 12 L min^{-1}. Samples were injected by a concentric Meinhard nebulizer in the concentric cyclone chamber. As calibration, the method of external standard was applied. Multi standard solution was purchased from Roth Rotistar.

Cells were harvested by centrifugation at 5000 min^{-1} for 15 minutes. The supernatant was used for HPLC analysis. The pellet was washed twice with pure water and utilized for biomass determination (dried at 105°C until its mass is constant).

For the analytical quantification of the fatty acid content and distribution, 5 mL yeast suspension was centrifuged at a rotational speed of 4000 min^{-1} for 15 minutes. The yeast pellet was washed twice with 5 mL of deionized water and dried at 105°C for 24 hours. The pellet was resuspended and methylated with 5 ml of methanol/acetyl chloride with a volumetric dilution of 50:2 for 24 hours at 60°C. The reaction was stopped by adding 2.5 mL of a sodium carbonate solution with a concentration of 60 g L^{-1}. Extraction was done by adding 2 mL of hexane and shaking for 2 minutes. The upper phase, containing the methyl esters, was transferred in a 1.5 mL crimp vial for GC analysis. The hexane extract was injected in a Thermo Trace GC equipped with an autosampler AS 2000 and detection was done with FID.

The chromatographic conditions were chosen according the chromatographic columns, an Agilent J&W capillary column DB23 60 m, 0.25 mm ID and 0.25 µm film thickness was used for analytical separation. The data analysis was performed with the software Chrom Card Data System Ver. 2.8 from Thermo Finnigan. For calibration the external standard method has been used.

III. RESULTS AND DISCUSSION

3.1. GLYCEROL COMPOSITION AND SCREENING OF YEAST AT DIFFERENT C/N RATIOS AND TEMPERATURES

The crude glycerol was kindly provided by the company BDI (Grambach, Graz, Austria). The content of this crude glycerol was analysed and shown in table 1. The crude glycerol contains considerable ammonium and nitrate values.

The yeast strains, *Candida lipolytica and Yarrowia lipolytica*, *Trichosporon fermentans* were chosen to evaluate the lipid accumulation potential for future microbial oil production.

We already determined the growth condition and lipid accumulation of the different yeast strains in pure glycerol medium [11].

TABLE 1, CONTENT OF THE CRUDE GLYCEROL

Glycerol	680 g L^{-1}
Sodium	10.05 g L^{-1}
Ammonium	2.05 g L^{-1}
Potassium	22.05 g L^{-1}
Magnesium	0.03 g L^{-1}
Calcium	0.015 g L^{-1}
Chloride	12.05 g L^{-1}
Nitrate	8.45 g L^{-1}
Phosphate	0.6 g L^{-1}
Sulfate	18.95 g L^{-1}
Aluminium	24 mg L^{-1}
Cooper	9 mg L^{-1}
Iron	11 mg L^{-1}

The lipid production via yeasts works mostly in a medium with an excess of the carbon source and limited nitrogen - the ratio of carbon and nitrogen sources (C/N ratio) influences the oleaginous potential of the culture. The determination of the optimal C/N ratio for both cell number and lipid accumulation is essential [12] [13], therefore cultivation of different yeast species was done in glycerol medium with variable C/N ratios (ranging from 27 up to 59) for 7, 10 or 17 days at different temperatures. The experiments were done in 50 ml medium in 250 ml Erlenmayer flasks. 50 ml crude glycerol based medium was inoculated with 10 % preculture (v/v; adapted yeasts).

At the start of the cultivation extra nitrogen source was added (yeast extract and peptone) to the glycerol medium. Low C/N ratio resulted in low lipid content (lower than 10 % (w/w, relating to the biomass, data not shown). Lipid accumulation increased after changing the nitrogen level and therefore the C/N ratio. Table 2 and 3 show the culture conditions, cell biomass and lipid content of the yeast strains with high lipid accumulation potential at 25°C temperature. Other conditions resulted in lipid content lower than 10 % (w/w, relating to the biomass) and therefore these data were not shown.

The achieved cell biomass ranged 0.42 g 100 g^{-1} up to 0.85 g 100 g^{-1} (shown in table 2) - values typically for oleaginous yeast growth in crude glycerol medium, for example the biomass of the yeast *Yarrowia lipolytica* achieved 6.5 g L^{-1} up to 8.1 g L^{-1} in crude glycerol medium [14].

TABLE 2, CELL BIOMASS OF THE YEASTS AT DIFFERENT CONDITIONS AT 25°C TEMPERATURE

Yarrowia lipolytica	
25°C; C/N ratio 59, 10 days	0.42 g 100 g^{-1}
25°C, C/N ratio 59, 17 days plus salt	0.79 g 100 g^{-1}
Candida lipolytica	
25°C, C/N ratio 59, 17 days plus salt	0.85 g 100 g^{-1}
Trichosporon fermentans	
25°C; C/N ratio 49, 10 days	0.69 g 100 g^{-1}

TABLE 3, LIPID CONTENT OF THE YEASTS AT DIFFERENT CONDITIONS AT 25°C TEMPERATURE

Yarrowia lipolytica	
25°C; C/N ratio 59, 10 days	18 %
25°C, C/N ratio 59, 17 days plus salt	20 %
Candida lipolytica	
25°C, C/N ratio 59, 17 days plus salt	20 %
Trichosporon fermentans	
25°C; C/N ratio 49, 10 days	17.9 %

The three different yeast strains, *Candida and Yarrowia lipolytica*, *Trichosporon fermentans*, accumulated lipid contents from 17.9 % up to 20 % at different culture conditions (summarized in table 3) – a phenomenon which seems to be yeast strain specific [4]. The yeasts mainly produced lipid like oleic acid, palmitic acid, stearic acid and linoleic acid – fitting for biodiesel.

The incubation temperature can influence the lipid accumulation too, therefore the same medium was used for further experiments at increased temperature of 30°C.

TABLE 4, CELL BIOMASS OF THE YEASTS AT DIFFERENT CONDITIONS AT 30°C TEMPERATURE

Yarrowia lipolytica	
30°C, C/N ratio 59, 17 days plus salt	0.51 g 100 g^{-1}
Trichosporon fermentans	
30°C, C/N ratio 59, 17 days	1.23 g 100 g^{-1}

TABLE 5, LIPID CONTENT OF THE YEASTS AT DIFFERENT CONDITIONS AT 30°C TEMPERATURE

Yarrowia lipolytica	
30°C, C/N ratio 59, 17 days plus salt	17 %
Trichosporon fermentans	
30°C, C/N ratio 59, 17 days	16 %

The lipid production potential of oleaginous yeast is obviously lower at higher temperature, the lipid content of the yeast *Yarrowia lipolytica* is lower than 10 % (w/w, relating to the biomass, data not shown) and the duration of lipid production of *Yarrowia lipolytica* and *Trichosporon fermentans* took more time. In comparison, the lipid accumulation of the oleaginous yeast *Candida* 107 reached a maximum at 25°C ranging the temperature from 19°C up to 33°C [15]. Maybe the lipid accumulation catabolism could be decelerated or be changed at higher temperature.

The crude glycerol already contained nitrogen sources (see table 1) – therefore the medium for lipid accumulation was prepared plus salt but without an additional nitrogen sources. Reduction or avoidance of external nitrogen sources will reduce the cost of the lipid production process and contributed to the marketability of this process.

The lipid accumulation potential of the three selected yeast was tested within this medium at two temperatures for 7, 10 and 17 days. *Trichosporon fermentans* and *Candida lipolytica* produced relative low biomass concentrations (see table 6) but good lipid contents (see table 7). Other conditions did not result in high lipid content (lower than 10 % (w/w) relating to the biomass) and therefore these data were not shown.

TABLE 6, CELL BIOMASS OF THE YEASTS IN CRUDE GLYCEROL MEDIUM AT 25°C TEMPERATURE

Trichosporon fermentans	
25°C, crude glycerol, 7 days plus salt	0.49 g 100 g^{-1}
25°C, crude glycerol, 10 days plus salt	0.47 g 100 g^{-1}
Candida lipolytica	
25°C; crude glycerol, 10 days plus salt	0.42 g 100 g^{-1}
25°C; crude glycerol, 17 days plus salt	0.45 g 100 g^{-1}

TABLE 7, LIPID CONTENT OF THE YEASTS IN CRUDE GLYCEROL MEDIUM AT 25°C TEMPERATURE

Trichosporon fermentans	
25°C; crude glycerol, 10 days	18.7 %
25°C, crude glycerol, 17 days plus salt	18 %
Candida lipolytica	
25°C, crude glycerol, 17 days plus salt	17 %

The yeasts were tested also at 30°C in this medium. *Yarrowia lipolytica* achieved biomass concentration of 0.45 g 100 g^{-1} and a lipid content of 22 % (w/w) relating to the biomass. Obviously the factor C/N ratio influences the lipid production to a greater extent than the temperature. Furthermore the nitrogen sources within the crude glycerol supported the lipid production via yeast and no external nitrogen sources will be needed.

In comparison to the results in other publications all achieved lipid data are quite lower [8] [9] – but the lipid production via yeast depends on several issues: selection of the yeast strain, on composition of the used substrate (included inhibiting or promoting substances) and kind of lipid extraction and transesterification.

Scale up experiments in 2 liters fermenter were done with yeasts in crude glycerol medium and the medium with variable C/N ratio to improve the lipid production via yeasts due to the improved controlled aeration and pH value. Various problems occurred – the production of citric acid, adhesion of the yeast, low biomass yield and lipid content. Diverse detergents were used to decrease the adhesion of the yeast. Different cultivation modes were tested and the pH value was regulated constant or no pH regulation was applied. Anyhow - the lipid content increased only up to a maximum of 17 % (w/w) relating to the biomass (see table 8). The biomass concentration reached a maximum of 0.33 g 100 g^{-1}.

TABLE 8, LIPID CONTENT OF *YARROWIA LIPOLYTICA* IN CRUDE GLYCEROL IN FERMENTER

Day 3	5.5 %
Day 6	7.3 %
Day 7	7.4 %
Day 10	9 %
Day 13	17 %

Crude glycerol is suitable as substrate for lipid production via yeast. An important requirement of commercialization is the price of the substrate used. Therefore the use of glycerol could contribute to the commercialization of lipid production with yeasts. Furthermore several challenges: higher biomass values and lipid content due to optimization of the process step by step, suitable fermenters and optimal mode of transesterification must be solved before industrial scale up.

IV. CONCLUSION

This paper has shown that specific oleaginous yeasts convert crude glycerol to lipids suitable for biodiesel production. Variation of the culture conditions in small lab scale mode concerning the C/N ratio, temperature and duration revealed the optimum at 30°C in a crude glycerol medium without external nitrogen sources. The produced lipid fitted for further biodiesel production.

The scale up experiments failed due to adhesion of the yeast, production of citric acid and low yeast numbers and lipid content.

Further improvements concerning each step within the lipid production process must be done before starting further scale ups.

REFERENCES

[1] Q. Li, W. Du and D. Liu., “Perspectives of microbial oils for biodiesel”, *Applied Microbiology and Biotechnology*, **80**, pp. 749-756, 2008.

[2] A. Amaretti, S. Raimondi, M. Sala, L. Roncaglia, M. De Luca, A. Leonard and M. Rossi. “Single cell oils of the cold-adapted oleaginous yeast *Rhodotorula glacialis* DBVPG 4785”, *Microbial Cell Factories*, **9**:73, 2010.

[3] J. Ageistos, J. Vallejo, P. Veiga-Cespo and T. Villa. “Oily yeasts as oleaginous cell factories”, *Applied Microbiology and Biotechnology*, **90**, pp. 1219-1227, 2011.

[4] I.R. Sitepu. L.A. Garay, R. Sestric, D. Levin, D. E. Block, J. B. German and K. L. Boundy-Mills. “Oleaginous yeasts for biodiesel: Current and future trends in biology and Production”, *Biotechnology Advances* **32:** pp. 1336-1360, 2014.

[5] OECD-FAQ Agricultural Outlook, http://www.fao.org/fileadmin/templates/est/COMM_MARKETS_MONITORING/Oilcrops/Documents/OECD

_Reports/OECD_2013_22_biofuels_proj.pdf, 2013, downloaded at 20. March 2015.

[6] P.A.E.P. Meesters, G.N.M. Huijberts and G. Eggink. “High cell density cultivation of the lipid accumulating yeast *Cryptococcus curvatus* using glycerol as carbon source”, *Applied Microbiology and Biotechnology*, **45**, pp. 575-579, 1996.

[7] J.C. Thompson and B.B. He. “Characterization of crude glycerol from biodiesel production from different feedstocks”, *Applied Engineering in Agriculture*, **22**:pp. 261-265, 2010.

[8] C. Saenge, B. Cheirsilp, T.T. Suksaroge and T. Bourtoom. “Potential use of oleaginous red yeast *Rhodotorula glutinis* for the bioconversion of crude glycerol from biodiesel plant to lipids and carotenoids”, Process Biochem **46**: pp. 210-218, 2011.

[9] S. Papanikolaou and G. Aggelis. 2002, “Lipid production by *Yarrowia lipolytica* growing on industrial glycerol in a single continuous culture”, *Bioresource Technology* **82:** pp. 43-49, 2002.

[10] F. Santamauro, F.M Whiffin, R.J. Scott and C.J. Chuck. “Low-cost lipid production by an oleaginous yeast cultured in non-sterile conditions using model waste resources”, *Biotechnology for Biofuels* **7**:pp. 34, 2014.

[11] R. Haselgrübler , A. Jäger, H. Kahr, K. Krennhuber and D. Steindl. „Lipid Production with different oleaginous yeasts with glycerol as carbon source and varying growing conditions”, Poster, 21st European Biomass Conference and Exhibition, Copenhagen, Denmark 2013.

[12] L.M. Granger, P. Perlot, G. Goma and A. Pareileux. “Efficiency of fatty acid synthesis by oleaginous yeast: prediction of yield and fatty acid cell content from consumed C/N ration by a simple method”, *Biotechnology and Bioengineering* **42**, pp. 1151-1156, 1993.

[13] C. Ratledge and J.P. Wynn. “The Biochemistry and Molecular Biology of lipid accumulation in oleaginous microorganisms”, In *Advances in Applied Microbiology*, edited by Laskin AI, Bennett JW, Gadd GM, San Diego: Elsevier Academic Press Inc, pp. 1-51, 2002.

[14] R.W. Nicol, K. Marchand and W.D. Lubnitz. “Bioconversion of crude glycerol by fungi”, *Applied Microbiology and Biotechnology* **93**: pp. 1865-1875, 2012.

[15] M.J. Hall and C. Ratlegde. “Lipid accumulation in an oleaginous yeast (*Candida* 107) growing on glucose under various conditions in a one- and two-stage continuous culture”, *Applied and Environmental Microbiology* **33**: pp. 577-594, 1977.

Journal of Energy Challenges
and Mechanics
http://www.nscj.co.uk/JECM/

ISSN 2056-9386
Volume 3 (2016) issue 2, article 4

District heating as the infrastructure for competition among fuels and technologies

区域供热作为燃料与技术竞争之基础设施

Poul Erik Grohnheit [1], Bent Ole Gram Mortensen [2]

[1] DTU Management Engineering, Technical University of Denmark, Building 426, Produktionstorvet, DK-2800 Lyngby, Denmark, pogr@dtu.dk
[2] University of Southern Denmark Department of Law, Campusvej 55, DK-5230 Odense M, Denmark, bom@sam.sdu.dk

Accepted for publication on 31st August 2016

Abstract - **District heating networks offer the possibility of competition between a wide range of fuels for combustion as well as technologies for comfort heat and cooling in buildings. For decades, cogeneration of electricity and heat for industrial processes or district heating has been a key technology for increased energy efficiency. Additional technologies suitable for small-scale networks are heat pumps, solar panels and local biomass in the form of straw or biogas. For large-scale urban networks, incineration of urban waste and geothermal heat are key technologies. With heat storages, district heating infrastructure can contribute significantly to balancing the intermittency of wind power.**

This paper is an update of the authors' article published in Energy Policy in 2003 focusing on the European directives focusing on competition in the electricity and gas network industries and promotion of renewables and cogeneration but limited support for the development and expansion of the district heating infrastructure. It was partly based on a contribution to the Shared Analysis Project for the European Commission Directorate-General for Energy, concerning the penetration of combined heat and power (CHP), energy saving, and renewables as instruments to meet the targets of the Kyoto Protocol within the liberalised European energy market.

The update will focus on recent research on district heating in North Europe, which covers not only the physical infrastructure but also the very important immaterial infrastructure, such as the legal and institutional framework. This includes the experience with market places for electricity trade on an hourly basis over the last two decades. Improved modelling tools and modelling experience will add to the development and performance of district heating systems.

Finally, we summarise the tasks for a European policy concerning the future regulation of district heating net-works for CHP, emphasising the need for rules for a fair competition between natural gas and district heating networks and the need for integration between energy systems.

Keywords **Infrastructure; District heating; Competition, Energy market, Legal Framework.**

Acknowledgement: The article is based on research for the 4DH - Strategic Research Centre for 4th Generation District Heating Technologies and Systems.*www.4dh.dk.*

I. INTRODUCTION

The primary intention of the EU electricity and gas directives is to make the electricity and natural gas markets part of the internal market. The overall objective has been to increase the availability of electricity and gas at more competitive prices for the benefit of the final consumers. The same objective was the motivation for the nationalisation of the electricity and other energy industries in several Western European countries – notably France, UK and Italy – a few decades earlier.

All these measures share the same strengths and weaknesses: The may increase the efficiency of energy supply by a single energy carrier – electricity or gas – by economies of scale, rational organisation and standardisation, or by introducing competition into an industry that is dominated by monopolies. On the other hand, they may be obstacles to a synergetic use of the various energy carriers at the local or regional level. The best illustration is the very different penetration of CHP for district heating in North West Europe.

This paper was originally based on a contribution to the Shared Analysis Project for the European Commission DG Energy, concerning the penetration of CHP, energy saving, and renewables as instruments to meet the targets of the Kyoto Protocol within the liberalised European energy market [1,2]. It focused on obstacles and lost opportunities for the development of district heating systems as a necessary infrastructure for further penetration of these technologies, emphasising the legal issues systems [3,4]. In recent years the concept of 4th Generation District Heating (4GDH) includes the relations to District Cooling and the concepts of smart energy and smart thermal grids [5]. This includes surplus electricity to be used in district heating [6]. Further, promotion of district cooling may increase efficiency [7].

During the last decade several EU and national research projects have focused on the integration of low carbon and renewable technologies for electricity and heat into the European energy market.

We are using Denmark as the main example, because the penetration of district heating has gone much further than in the large countries in north-west Europe, in spite of no significant difference in climate and the urban physical structure. District heating systems is the backbone of the physical infrastructure that will allow 50 % or more of the Danish electricity demand to be supplied by wind power.

The immaterial infrastructure is just as important as the physical infrastructure for the integration of wind. Especially the physical commodity exchange (energy exchange) – Nord Pool Spot – operating the world's largest electrical power exchange with a day-ahead market and an intraday market has become an important part of the Nord European power market. The main part of Nord Pool Spot is owned by the TSO’s in Norway, Sweden, Finland and Denmark.

II. INFRASTRUCTURE FOR SPACE HEATING AND COMPETITION AMONG FUELS AND TECHNOLOGIES

The infrastructures for electricity and natural gas are mature in most European countries. The natural gas infrastructure is dependent of a single fuel, which must be imported to the European Union in increasing amounts, although biomass offers an alternative within their resource limitations. The district heating infrastructure can exist in all scales, but requires a higher heat density than gas networks – and water-based heating systems in buildings.

2.1. THE URBAN HEAT MARKET

Fig. 1 describes the urban heat market as a hierarchy of building levels and heating technologies. Half a century ago solid fuelled stoves in single rooms were dominant even in urban areas. The customers were independent of collective systems and could be free to choose their supplier of coal, coke, fuel wood or paraffin. Today, these systems are found only in outdated flats. Electric heating is an additional choice that requires limited investment, but it may be too expensive for the – often poor – residents. In many cities the introduction of natural gas has improved the standard of living at moderate costs

In some countries – in particular the United Kingdom – natural gas is frequently used for water-based radiator systems supplied from an individual boiler in each flat. This system is dominant for single-family houses in areas with natural gas supply in most countries in northwest Europe. The introduction of competition in the gas sector based on the natural gas market directive has given the customer free choice among several gas suppliers. Also new technologies may become available for gas customers in the near future, which may increase fuel efficiency and competition, in particular micro-scale CHP in the form of gas engines or fuel cells. However most of these new technologies are gas-only technologies with limited flexibility concerning base and peak load.

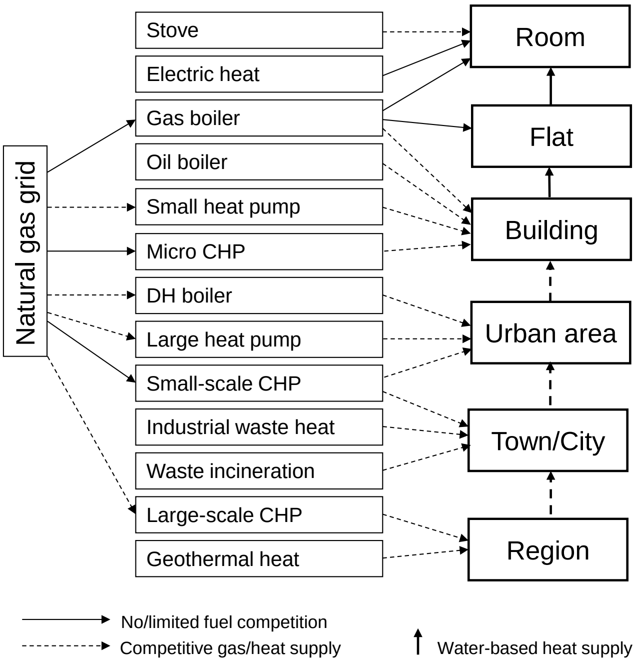

Fig.1. The urban heat market.

The principal advantage of larger water-based heat distribution system is that they enable more competition among fuels and technologies both in the short and long term, and possible also cheaper heat supply. On the other hand, these systems require investment in infrastructure over decades and regulation, which may reduce the short-term choice of the individual consumers. District heating itself is a system in competition with other systems [8].

District heating for single-family houses is best established as a part of the development of sites for detached or terraced houses together with electricity, water and sewage. At this level competition from a natural gas grid or individual boilers may be detrimental for energy efficiency and recovery of investment. Larger groups of single-family houses with water-based heat distribution systems or blocks of flats or offices will have a local infrastructure that may be supplied by connection to an urban-wide district heating system in competition with large gas-fired boilers or small-scale CHP.

Larger district heating systems, covering a whole town or an urban region, offer more opportunities for competition between fuels and technologies for heat supply, in particular urban waste incineration, industrial waste heat, or transmission of geothermal heat.

2.2. OVERLAPPING INTERNATIONAL ELECTRICITY AND GAS MARKETS

The electricity and gas markets are becoming more overlapping. New gas transmission lines may not only have impact on the gas trade. It may also lead to further integration of the European market for wholesale electricity. With the increasing capacity of gas-fired electricity generating units, gas will be used for electricity generation, where the price of electricity is highest. The organised markets for spot and future electricity already exist. Nord Pool Spot now operates in Norway, Denmark, Sweden, Finland, Estonia, Latvia, Lithuania, Germany and the UK. The spot and futures markets of Nord Pool have become a model for power exchanges in the Netherlands, Germany, Poland and Spain.

2.3. THE ‘SINGLE ENERGY CARRIER’ DIRECTIVES AND DISTRICT HEATING

The common rules of the two energy market directives (electricity and natural gas) are similar, but the two network industries are treated separately. The disadvantages of the separate treatment of the electricity and gas grids regarding the creation of the internal market are small, because there is only a limited potential for competition between these two types of grids. However, none of them are considering the district heating systems, although the district heating networks offer the possibility of competition between natural gas and a range of other fuels on the market for space heating.

The law and regulations regarding anti-competitive agreements and abuse of dominant position may apply not only to the electricity and gas markets but also to the heat market. However, part of the heat market is supplied by a third network industry, district heating, which provides a market for several competing types of fuels and technologies, including natural gas, various types of biomass combustion including incineration of urban waste, and combined heat and power (CHP). The heat market might be left in a regulatory ‘vacuum’ only regulated by national provisions and the general EC Treaty provisions, while CHP producers can be regulated by both the electricity and gas market directives and parallel national legislation. This may involve a risk of conflicts between the different set of rules.

Several of those technologies that may be victims of this regulatory conflict are supported by EU policy as means to meet environmental challenges or technologies to meet the target of sustainable development, including international obligations to reduce the emissions of greenhouse gasses.

III. CONSUMERS’ CHOICE, INFRASTRUCTURE AND COMPETITION

The regulatory frameworks for district heating, electricity and natural gas are normally very different. However, some common characteristics exist, in particular with regard to large-scale district heating networks. Competition involving CHP exists in different ways. As supplier to district heating grids certain possibilities in competition with existing suppliers seem open. Vertical disintegration (unbundling) exists also within the district heating market. There are examples of markets for district heating, which seem relatively mature and already use market mechanisms in buying heat.

3.1. HOUSEHOLD CONSUMERS

Both European and national competition authorities tend to have a bias towards cash-and-carry items with low transaction costs, and high discount rates in the choice of production technology. These features are compatible with goods and services that are internationally traded. With some innovative types of regulation, the development in the late 20th Century demonstrates that competition can be introduced in industries that were considered as natural monopolies, in particular telecommunication, public transport, electricity and natural gas.

Other markets have features that are very different from these, e.g. the real estate market. In particular the market for resident-owned housing is characterised by long-term investments, very high transaction costs, and low personal discount rates. For most individuals and families the housing market is far more important than the energy market.

3.2. LOCAL GOVERNMENT AND CUSTOMER CHOICE

A key issue in the development of district heating systems has been the role of local government and local interests in the electricity supply industry and other utilities. In some countries local government is directly or indirectly owner of utilities or has an important influence on physical planning and urban/regional development. It is worth mentioning that in those countries, where the electricity supply industry was nationalised into a single dominant vertically integrated organisation, there has been very little development of district heating systems.

Some of the traditional instruments that were used by local government for the development of these systems do not comply very well with the liberalised markets. Customer choice of supplier is a basic element of the liberalisation of energy markets. However, the individual choice by consumers may be counterproductive to the target of creating a competitive market for space heating with competition between fuels and technologies. Thus, limiting the consumers’ choice on the local level – e.g. by regulation in the form of zoning that requires the use of particular heating systems, in particular district heating – will add to competition on the energy market as a whole.

The opposite of individual choices is collective decision by public planning. Such decisions may provide better solutions for the individual customers. The collective decisions may enable competition among fuels and technologies that are not available for the individual customer. In countries with tradition for individual home ownership financed by long-term mortgage loans, there is also a tradition for very strict physical planning and regulation. While new district heating grids in existing neighbourhoods may be too expensive, this may not be the case for new developments. Here, district heating becomes an alternative to investments in a new gas grid with individual boilers.

3.3. COMPETITIVE ELEMENTS IN NETWORKS FOR HEAT SUPPLY

The principle that is used for introducing competition in the electricity and gas supply industries is that generation and supply are subject to competition, while the grid activities – transmission and distribution – remain natural monopolies subject to regulation. A similar concept may be developed for district heating, either on a national level or harmonised for the Member States of the European Union.

Large-scale district heating networks have some characteristics that are similar to the electricity market. Although there is no example of an urban district heating grid with full-feature third party access and competition between many suppliers, there are examples of unbundling between competing heat producers using a variety of primary fuels and technologies, a monopoly transmission company, and several local distribution companies. The latter may be subject to various elements of competition, in particular competition between local heat production and purchase from the transmission grid.

There is now more than twenty years of experience with competition and market organisations in the electricity sector. There are only some few examples of attempts to introduce third party access and competition into district heating grids, and there are many examples of elements of competition between district heating and natural gas grids:

- Competition in the planning of grid distributed energy in new developments, where a license for grid development should be granted either to district heating or natural gas, but not both.
- Competition among heat generators (industrial waste heat, incineration of urban waste, CHP from large-scale and small-scale generators, heat-only boilers with combustion of different fuels).
- Competition among owners of boilers for peak load either through long-term contracts or a short-term market. In an interconnected district heating system, heat supply from boilers is important to overcome temporary capacity limitations in the grid.
- Outsourcing of operation and maintenance of grids or administration of supply, metering and billing of customers.
- Takeover of a district heating system by a utility company that is operating on a national or international scale
- The development and implementation of competitive elements for grid distributed energy network takes time and requires the development and implementation of new software and information systems.

The history of liberalisation of the electricity and gas sector already has numerous examples of delays and chaotic implementation due such practical issues, which are vastly underestimated in the more ideological discussion on liberalisation and competition in network energy industries.

IV. THE EUROPEAN MARKET FOR DISTRICT HEATING

In the Communication from the Commission to the Council and the European Parliament of October 1997 “A Community strategy to promote combined heat and power (CHP) and to dismantle barriers to its development” (COM(97) 514 final), it was stated that: “CHP is one of the very few technologies which can offer a significant short or medium term contribution to the energy efficiency issue in the European Union and can make a positive contribution to the environmental policies of the EU.” In 1994 less than 10 % of the electricity generation in the EU was combined production with significant variations among Member States: From more than 30 % in the Netherlands, Denmark and Finland to less than 5 % in the UK, France, Greece and Ireland. The maximum technical potential of CHP has been assessed by different studies to 40 % of the total electricity generation in the mid-1990s. In a recent study the potential for district heating in Europe has been indicated to 46 percent of all excess heat in EU27 (corresponding to 31 percent of total building heat demands) is located within identified strategic regions [9].

This potential includes CHP for both industrial steam raising and district heating and cooling. Increased energy efficiency in industrial processes and space heating will reduce the technical potential for heat supply from CHP, which is dependent of the heat densities of the local heat markets. However, past experience has shown that the penetration of CHP has been widely different in the countries in north-west Europe, in spite of no significant difference in climate and urban physical structure. The main explanation is the relative power of various institutions [2]

4.1 THE MARKET POTENTIAL FOR CHP, WASTE INCINERATION AND GEOTHERMAL ENERGY

CHP for space heating is available only via infrastructure in the form of a heat distribution system in an appropriate scale. Large extraction-condensing power stations with an electric capacity of several hundred MW will need an interconnected district heating grid for the sale of its potential for cogenerated heat. Small-scale CHP units are designed for a local water-based heat distribution system for a building, or a local group of buildings, a village or a small town.

The largest district heating systems in the European Union are in Berlin Copenhagen, Helsinki, Hamburg, Stockholm and Paris. None of these systems have been developed over a short period according to a single initial plan. They were developed over decades for different reasons by adding new elements to the existing infrastructure, often taking advantage of temporary and unusual situations, e.g. the high oil prices in the period 1973-1985. The most constant elements have been local or national actors with a consistent interest in finding ways and means for expanding the district heating markets and networks.

Increased energy efficiency in space heating by better insulation will reduce the technical potential for heat supply from CHP, which is dependent of the heat densities of the local heat markets. On the other hand, a given heat market will become a basis for a much larger generation of electricity, because of a very significant increase in the power-to-heat ratio. The power-to-heat ratios for new combined-cycle gas turbine (CCGT) or gas engines are about 1.0 compared to 0.4 for traditional gas turbines a decade ago. Thus, the same heat market will become the basis for a much larger electricity generation.

Waste incineration. In Denmark waste incineration is an integrated part of district heating systems, delivering base load. Incineration of municipal solid waste in Denmark started in 1903 in a densely populated municipality with little access to space for landfill. The energy was used for a district heating system established at the same time and for generation for the local grid. It was built opposite to the new municipal hospital with supply of central heat for the hospital and electricity for the local grid.

District heating grew significantly during the 1960s – mainly driven by excess heavy fuel oil from the new-established Danish refineries. This gave a market for the heat from waste incineration plants, which was established in many medium-sized towns. The mismatch between the seasonal variation in the heat demand and the all year-round supply from waste incineration plants was gradually solved by expanding district heating grids and interconnection of smaller separate grids. With the high penetration of waste incineration in Denmark, the volume of incinerated waste will decrease, because waste treatment policies aim at increasing recycling on the expense of waste incineration [10].

Geothermal energy. District heating systems is an important market for geothermal energy in a larger scale. However, the Danish experience is limited. Geothermal sources are available in Denmark, but other sources for supply of district heating systems are more competitive.

District cooling. Even in a Nordic context, many buildings have a need for comfort cooling in the interest of the users. In most places, building cooling is done by means of electrically driven compressors installed in the building. The term “district cooling” refers to the arrangement where the cooling of a building is handled by centralised units which distribute cooling to multiple buyers through a heating or cooling medium via a grid. District cooling is a collective solution as an alternative to an individual cooling solution.

To simplify a little, district cooling covers two basic concepts. First, a primary solution is where cold water is produced in a facility and distributed through a network to a number of buyers. The central station can use different sources such as low temperatures in groundwater, lake water and seawater (so-called “free cooling”), and secondly energy for cooling can be obtained by utilising the energy in district heating water feeding district heating water to the end-user absorption unit which utilises district heating water to produce cooling water. The ability to convert district heating to cooling has made the technology particularly interesting to the district heating sector and thus for countries with a large district heating sector, such as the Nordic countries Finland, Sweden and Denmark.

In Finland there has been cooling in Helsinki since 1998, and now it is also used in Turku, Lahti, and Vierumäki. Denmark has not come so far; the supply of district cooling from a major public construction project only began in 2009 (in Copenhagen). The most advanced of the three Nordic countries is Sweden, where the first plant was built in 1992. Denmark has had a special District Cooling Act (Act No. 465 of 17 June 2008 on municipal district cooling) which specifically provides a basis for municipal participation in district cooling operations [7].

4.2 MODEL ANALYSES

The technology choice for electricity generation has been an important topic for traditional optimisation models, e.g. EFOM, MARKAL and TIMES, developed within the EU framework programmes and the IEA Implementing Agreement, ETSAP, *www.iea.etsap.org*. In a competitive market this optimisation is of limited interest. However, the same modelling tools can be useful for the analysis of different agents or market participants. A model developed for analyses of the electricity and CHP markets in the Baltic Sea Region has been used for numerous studies in many countries, including China, *www. balmorel.com* [11]. Very detailed data and geographical information systems (GIS) are essential tools for modelling district heating on a local level [12].

In global optimisation models, e.g. TIAM or EFDA-TIMES, which are divided into 15-17 regions, e.g. Europe or China, the district heating infrastructure can be modelled using very aggregated parameters for costs and efficiencies [13].

V. A EUROPEAN POLICY ON HEAT DISTRIBUTION NETWORKS

Numerous policy initiatives over the last decades have focused on CHP rather than district heating as a means for energy efficiency and CO_2 reduction. The emphasis from international organisations and lobbying organisations are mostly on small-scale CHP application for industries and smaller heat distribution networks, e.g. large hospitals. However, recent initiatives from the IEA are focusing on the “the network’s ability to use many heat sources including ones with renewable fuel sources” and express the concern that “market forces may drive solutions that may be shorter term than is optimum for society and discriminate against high capital technologies such as district heating.”

A community policy will be needed for support of the infrastructure necessary for further penetration of CHP, which should include framework conditions for local heat distribution networks that are compatible with the different national traditions of regulation of real property. Most of the elements for such a policy are found in existing EU legislation. However, existing legislation may contain a wide range of inconsistencies and conflicts that may be obstacles for both CHP, energy efficiency and renewables.

A community policy would also be needed to support and regulate the development of procedures for international tendering for operation of district heating networks. So far, a marked directive regarding districting heating has not been on the political agenda. As long as district heating in Europe mainly consists of local markets it can be questioned whether such a directive falls within the competence of the EU according to the principle of subsidiarity in the Treaty. However this principle shall not prevent the EU in developing Trans-European energy infrastructure including in the area of district heading.

A key task for the Commission to promote the development of CHP would be to support the legal framework and procedures for the development of district heating grids and the interconnection between them.

The role of district heating systems for balancing wind power is becoming increasingly important. In addition to heat storages, there is a range of technologies that offer flexibility for the electric system: Electric boilers with low investment cost are useful for surplus electricity in short periods. Heat pumps and CHP require much higher utilisation times, but they operate complementary to balance wind, while producing heat. It is essential that markets and regulation offer the proper incentives for investment in both [14].

Some of the issues that were discussed in the article from 2003 [1] may be addressed in Heat Roadmap Europe [9].

REFERENCES

European Union legal documents

Directive 2009/72/EC of the European Parliament and of the Council of 13 July 2009 concerning common rules for the internal market in electricity and repealing Directive 2003/54/EC. (the electricity market directive).

Directive 2009/73/EC of the European Parliament and of the Council of 13 July 2009 concerning common rules for the internal market in natural gas and repealing Directive 2003/55/EC (the natural gas market directive).

Directive 2010/75/EU of the European Parliament and of the Council of 24 November 2010 on industrial emissions (integrated pollution prevention and control) Treaty on the Functioning of the European Union (TFEU).

[1] Grohnheit, P.E.; Mortensen, B.O.G. (2003) Competition in the markets for space heating. District heating as the infrastructure for competition among fuels and technologies. Energy Policy Vol. 31, pp. 817-826

[2] Grohnheit, P.E (1999), Energy policy responses to the climate change challenge: The consistency of European CHP, renewables and energy efficiency policies (Office for Official Publications of the European Communities, Luxembourg) (Energy in Europe, Special issue, December 1999 with appended CD-ROM)

[3] Mortensen, B.O. G. (1998), Elforsyning – afvejning af hensyn til en sektor på vej mod det indre marked [Power Supply – Considerations to be taken in a Sector heading for the Internal Market] DJØF Publishing, Copenhagen.

[4] Mortensen, B. O. G. (2004), Elforsyningsloven med kommentarer [A commentary to the Danish Electricity Supply Act], DJØF Publishing, Copenhagen.

[5] Lund, H.; Werner, S; Wiltshire, R.; Svendsen, S.; Thorsen, J.E.; Hvelplund F.; Mathiesen, B. V. (2014), 4th Generation District Heating (4GDH): Integrating smart thermal grids into future sustainable energy systems, Energy, Vol. 68, pp. 1-11.

[6] Averfalk, H.; Ingvarsson, P.; Persson, U.; Werner, S. (2014), On the Use of Surplus Electricity in District Heating Systems, proceeding from the 14th International Symposium on District Heating and Cooling (*http://www.svenskfjarrvarme.se/In-English/District-Heating-in-Sweden/The-14th-International-Symposium-on-District-Heating-and-Cooling-/Proceedings/*)

[7] Mortensen, B.O.G. (2014), Legal Framework as a Core Element of District Cooling Success – The Case of Denmark. Journal of Power and Energy Engineering, Vol. 2, No 9, pp. 41-48, ISSN 2327-588X *(www.scirp.org/journal/jpee)*.

[8] Mortensen, B.O.G. (2012), Fjernvarme – en monopolsektor i konkurrence [District heating – a monopolistic sector competition] in Festskrift til Jens Fejø, DJØF Publishing, pp. 299-310

[9] Persson, U., Möller, B.; Werner, S. (2014): Heat Roadmap Europe: Identifying strategic heat synergy regions, Energy Policy, vol. 74, pp. 663-681.

[10] Münster, M.; Lund, H. (2009), Use of waste for heat, electricity and transport – Challenges when performing energy system analysis. Energy Policy, Vol. 34, pp. 636–644.

[11] Balmorel Project (2001), Balmorel: A Model for Analyses of the Electricity and CHP Markets in the Baltic Sea Region. *www.balmorel.com*.

[12] Petrović, S.; Karlsson, K.B. (2014). Danish heat atlas as a support tool for energy system models. Energy Conversion and Management, Vol. 87, pp. 1063–1076. 10.1016/j.enconman.2014.04.084

[13] Grohnheit, P. E.; Korsholm, S.B.; Lüthje, M (2011), Long-term modelling of Carbon Capture and Storage, Nuclear Fusion, and large-scale District Heating, Risø International Conference 10-12 May 2011. Risø-R-1776, 56-66 (2011)

[14] Grohnheit, P.E.; Møller Andersen, F.; Larsen, H. V. (2011) Area price and demand response in a market with 25% wind power. Energy Policy, Vol. 39, pp. 8051-8061.

Journal of Energy Challenges
and Mechanics
http://www.nscj.co.uk/JECM/

ISSN 2056-9386
Volume 3 (2016) issue 2, article 5

Funnel Flight Controller for a Simulation Model and Attitude Control System

漏斗飞行控制器用于仿真模型和姿态控制系统

Dr. Norman Hopfe[1*] and Dr. Guido Kurth[2]

[1]*R&D Engineer, Bayern-Chemie GmbH, P.O. Box 1131, 84544 Aschau am Inn, Germany*
[2]*Technical Director, Bayern-Chemie GmbH, P.O. Box 1131, 84544 Aschau am Inn, Germany*

norman.hopfe@mbda-systems.de

Accepted for publication on 27th July 2016

Abstract - **In the recent years modeling has become an important tool for predicting the behavior and the design of dynamical systems resulting in a reduced need for numerous and often expensive testing. Especially if the system under investigation cannot be tested completely under accessible test conditions on ground, the development of reliable simulation tools is mandatory for its design.**

Within this paper, the development of an advanced simulation tool is presented which is able to predict the behavior of a so called Attitude Control System (ACS) which is used to adjust the attitude of a missile to agility requirements commanded by the onboard guidance, navigation and control device. Here the focus is laid on the internal dynamics of such an ACS.

In general, an ACS can be regarded as a small scale rocket engine with the capability of providing thrust at certain points of the operational activity. This is usually realized by a set of circumferentially mounted "mini" motors which can be triggered individually while the missile performs a rotational movement along its longitudinal axis or by a continuous burning (solid propellant) motor which feeds a throttleable Cartesian nozzle configuration.

The advantage of such a system lies in the fact that it provides a continuous operation capability. The thrust direction can be controlled by a simultaneous modification of the four nozzle throats, usually realized by a hot gas valve system consisting of so called pintles which can be shifted (either two coupled or four individually) backwards and forth to increase or reduce the respective nozzle throat area.

For the current investigation an ACS is simulated which consists of a gas generator that produces a hot gas which is led into a pair of throttleable nozzles. The nozzles are aligned along a straight line and throttled by a coupled pintle system. The pintles connected via a metallic rod are shifted backwards and forth to change the respective nozzle throats such that with closing one throat the other will be opened. The rod is connected via a lever with an actuator.

Such a configuration allows very fast thrust modifications by side thrust change and due to this a very fast position change of the missile depending of the location of the ACS with respect to the missile's center of gravity.

This paper comprises the simulation model and application for such an ACS containing brief descriptions of the flight control algorithms and a mathematical simulation model. It investigates the performance prediction for the ACS.

For all models a funnel controller method is used as an automatic control tool. It is shown how the funnel controller is used in a simulation and for a real test facility trial aiming at a fast thrust variation.

The theoretical funnel control and experimental results of a laboratory rotatory mechanical system from [SIAM2013] are combined and extended to speed funnel control with nonlinear disturbances and elastic deformation without active damping where only thrust measurement is available. The extended innovative funnel control concept is applied to this highly reactive ACS and guarantees extremely fast thrust tracking with a required transient accuracy in the low millisecond range to achieve maximum performance. The knowledge of all system parameters, the nonlinear mass flow link and the actuator interaction is not required.

Keywords - **Funnel control, Attitude Control System, nonlinear systems, transient behavior, solid propellant, gel propellant, simulation model, propellant burnback, Matlab**

I. INTRODUCTION

This paper investigates the accuracy of a performance and design model in simulating the thrust generation, thrust direction, combustion pressure behavior, pintle movement, actuator behavior, propellant choice and propellant grain geometry (for solid propellant) etc. of an actively controlled ACS complemented by a methodology to properly model the system by a precise mathematical description. The basic physical equations of the dynamic can be found in [ROMA2009], [TAM2004], [WILE2001].

The simulation of the performance of an actively controlled ACS is a combination of all the characteristics of the system (e.g. mass properties, performance requirements, propellant burning and combustion gas supply, geometrical configurations), environmental conditions and actuator behavior. The tracking of a changing thrust profile (thrust direction and thrust level) requires a permanent adjustment of the commanded pintle position of the ACS (i.e. actuator command in voltage) in order to compensate the differences between the real measured and the nominal thrust due to manufacturing, measurement, atmospheric modeling errors and due to material failures during operation of the system (e.g. insulation fracture and/or rupture or particle deposition in the nozzle throat area).

A detailed simulation model enables engineers to investigate the dynamics and performance during each design phase. In the current model, the significant parameters (e.g. combustion pressure, nozzle exit pressure, thrust etc.) and component behaviors (e.g. actuator behavior model) are determined by different methods – experimentally (e.g. nozzle erosion), CFD analysis (e.g. nozzle design and performance) as well as semi-empirical (e.g. actuator behavior model) and analytical methods (e.g. propellant burning, pressure and thrust generation). The first group obtains data from test facility trials and flight tests. The CFD methods solve a set of fundamental equations for fluid domains – divided into discrete cells – to simulate flow fields and forces (e.g. internal forces and pressure along the boundary layer). At last, the semi empirical and analytical methods calculate the behavior via analytical formulas and an existent empirical database. The last method is the quickest way to determine or approximate the performance of a new component of the dynamical system or the missile/system performance and is thus important during development.

In order to ensure the correct functioning of the system in all phases, a robust and reliable control algorithm has been developed. Its effectiveness has been proven in numerous ground trials. A brief overview of the controller is given in the section of the performance funnel description in this paper. The interested reader is referred to [UVIL2010] for a detailed description.

II. ATTITUDE CONTROL SYSTEM: FUNCTION AND REALIZATION

ACS's use (impulse) force to control the attitude (pitch, yaw and roll) of a vehicle flying inside or outside the atmosphere. Vehicles using an ACS system are upper stages of space launchers, missiles or missile defense interceptors designed to intercept (ballistic) missiles and their effectors.

Missiles with an ACS system (see Figure 1) are Lockheed-Martin´s PAC 3 ground based air defense missile incorporating an array of many small solid impulse thrusters and MBDA´s CAMM ship-based air defense missile with a continuously operating solid gas generator to turn the missile after vertical launch and point it towards the correct direction. Well-known examples of missile defense systems are the Terminal High-Altitude Area Defense System (THAAD), which uses liquid propulsion to maneuver an endo-atmospheric vehicle and the longer range SM-3 missile, which uses solid propellant propulsion to maneuver an exo-atmospheric kill vehicle.

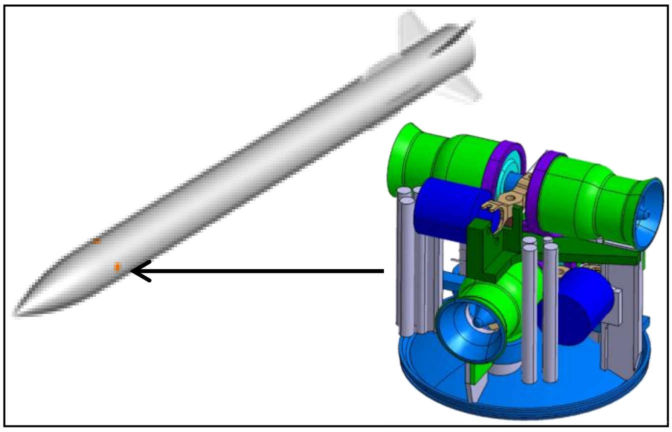

Figure 1: missile scheme with ACS

In space applications, ACS blocks, often designated as “Vernier Motors”, can be used to control the attitude of the launch vehicle without the need to integrate a movable nozzle into the solid propellant rocket motor or to move the liquid propellant rocket motor. Well-known applications are the Vernier motors of the Sojuz launcher.

Currently, liquid and solid propellant ACS are used in operational vehicles. The liquid ACS of the Ground Based Interceptor (GBI) uses individual ACS thrusters from space propulsion technology. These thrusters operate intermittently and use hydrazine or a derivative as propellant. The solid ACS of the SM3 has a central combustion chamber with supposedly three solid propellant grains that produce a mission-adapted level of gas flow for the ACS along the mission.

For vehicles that fly within the atmosphere, ACS's are in use to increase the agility of a missile in conditions where the aerodynamic forces do not generate sufficiently high pitch and yaw moments or in order to secure a direct hit. This can be the case immediately after the launch of a missile, when the low velocity does not generate the aerodynamic control force needed for a quick turn or in the final approach to a maneuvering target at high altitude, when the low atmospheric pressure does not support quick control of pitch and yaw. The thrust vector of an ACS creates a lateral force at a distance of the Centre of Gravity (CoG) of the missile. The thrust vector of an ACS creates a lateral force at a distance of the CoG of the missile.

The introduced ACS concept assumes a central and continuously operating gas generator to supply the nozzles with produced gases which create the necessary thrust directions. A hot gas pipe transports the produced gas from the gas generator to the ACS.

The design uses four coupled, controlled nozzles with plenum, pintles and actuators, i.e. the two pintles of one nozzle plane are connected. The system has a quasi-Cartesian configuration with pintles to regulate the nozzle throat and control the thrust direction, i.e. the system has two planes with two nozzles. The actuators are outside of the hot gas. The design assumes coupled nozzles to steer the gas flow through the nozzle pair to reduce complexity and number of actuators. A scheme of the system can be seen in Figure 2.

The actual design assumes that the gas generator supplies the nozzle plenum over a hot gas pipe with thermal insulation and efficiency loss. A complete closure of a nozzle is a harder challenge then a “nearly closed” condition. Therefore, the design concept assumes a “nearly closed” nozzle.

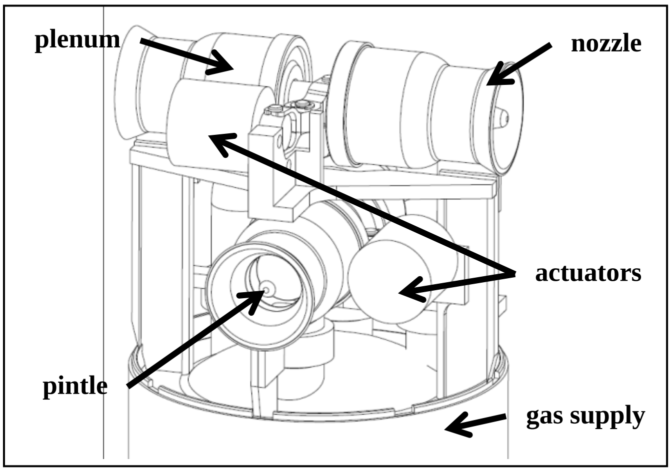

Figure 2: ACS configuration with four nozzles and actuators

Figure 2 shows the basic building blocks of an ACS with the exception of the electric energy and gas supply. In most designs a gas generator supplies the gas that is distributed by the nozzle, pintle blocks according to the thrust demand. The ACS thrusters are located outside the CoG near the periphery. For missile applications, the total time of operation of ACS is typically some seconds depending on the mission profile.

Continuously operating ACS’s, as shown in Figure 2, consist of three main building blocks - namely the combustion gas supply (CGS), the nozzle, pintle, actuator blocks that distribute the gas to the ACS’s nozzles and the control unit that controls the pintle and actuator and, if possible, the CGS system, to convert the signals from the guidance, navigation and control (GNC) into thrust vectors of correct magnitude and direction. In many applications the nozzles and the pintles are one assembly that is very tightly connected with the actuators. The mechanical interface between CGS and nozzles can be described comparatively easily as a flow of hot combustion gas with determined mass flow at a given set of state parameters. This allows to take pintle nozzles with actuators and CGS as separate mechanical entities. More complicated are the interfaces of the control unit with both pintle nozzle actuator and CGS if the CGS can produce a variable mass flow (e.g. gelled propellant gas generator or TDR with solid propellant) which has to be controlled by the control unit in connection with the nozzle, pintle and actuator.

Due to their compact design, pintle nozzles are the preferred solution. Independent on the design of the nozzle and valve, the materials of both have to withstand the extreme heat loads generated by the hot gas at high pressure. The pintle nozzles can be designed to have always a constant total nozzle throat area $\sum_i A_{throat,i}(\cdot) = \text{nearly const.}$ This allows to connect the control of oppositely oriented nozzles directly in that way that the sum of both $A_{throat}(\cdot)$ is nearly constant, independent from the displacement of the pintle. By this, one actuator can drive the pintles for these two oppositely oriented nozzles.

III. FUNCTIONAL BEHAVIOR OF THE CURRENT ACS

The current ACS is meant to be applied within an interceptor against incoming ballistic missiles. Hence, it should be able to guarantee, that the interceptor is capable of hitting the target within a certain “miss distance” depending on the intercept velocity and misalignment of the interceptor with respect to the target.

In addition, the ACS should also be capable of stabilizing the missile attitude such, that a seeker is able to track the ballistic missile’s trajectory in order to enable the GNC to guide the missile properly to its predicted intercept point (PIP).

For this purpose, the current ACS uses four thrusters that have to provide the required thrust very accurately within a required thrust level and time frame. Depending on the missile and mission design, the ACS has to perform over a wide range of altitudes. In case the ACS is located outside the CoG, the missile maneuvering capability can be increased and the time constant for “instant” turns can be reduced.

The benefits of the current system are then

- compact system,
- attitude control in low and high altitudes
- hit to kill precision and
- a continuous operation of the system.

The concept is in its essence a thrust system with four nozzles in a quasi-Cartesian configuration.

The thrust direction is an integral element effectively controlled by an actuator system. Hot gas pintles are integrated to provide the control authority as part of the ACS. The actuators are directly coupled with the hot gas pintles which control the thrust direction of the ACS. In all cases, the actuators and their control are an integral element of the system.

If a constant mass flow gas generator, for example a solid fuel gas generator, is used, the use of four individually controlled ACS nozzles allows for significant savings of propellant mass. This is because only those ACS nozzles that need to provide thrust have to be opened while all other nozzles can be kept closed - thus preventing the loss of waste gas.

If a variable mass flow gas generator - like a gelled propellant gas generator or a RJ gas generator - is used the gas generator mass flow can be controlled through a valve additionally to the four controlled ACS nozzles.

Assuming that the gas is isentropic and the GG temperature is constant, the simplified gas supply dynamics can be described by the following ordinary differential equation:

$$\frac{V_{combustion}(\cdot)\,\dot{P}_{combustion}(\cdot)}{R\,T_{combustion}} = \frac{\rho_{propellant}\,A_{burning}\,r_{burn}}{R\,T_{combustion}} + \frac{\rho_{propellant}\,\dot{P}_{combustion}(\cdot)}{R\,T_{combustion}} - \frac{P_{combustion}(\cdot)\,A_{throat}}{c^*}.$$

The variables in the equation are explained in the nomenclature section at the end of this paper. The detailed dynamic description of the model is given in the mathematical model subsection (see (2)).

In order to show the capability of the system, the second component of the 3-dimensional Lorenz system has been chosen as a reference thrust tracking curve. The following simulation results use the Lorenz system

$$\begin{aligned}
\dot{\xi}_1(t) &= \xi_2(t) - \xi_1(t) && ,\xi_1(t) = 1\\
\dot{\xi}_2(t) &= \frac{28}{10}\xi_1(t) - \frac{1}{10}\xi_2(t) - \xi_1(t)\xi_3(t) && ,\xi_2(t) = 0\\
\dot{\xi}_3(t) &= \xi_1(t)\xi_2(t) - \frac{8}{30}\xi_3(t) && ,\xi_3(t) = 3
\end{aligned}$$

The Lorenz system has the advantage that the system is fully deterministic, chaotic and bounded with bounded derivatives (see [SPAR1982], App. C), i.e. an estimation of the reference signal behavior in the future is not possible.

The simulation of the thrust performance of a coupled two-nozzle system assumes an actuator with a time constant of 40ms (for so called “bang bang” control) and a non-throttleable high-energetic solid propellant gas generator.

The graphs of the combustion chamber pressure, thrust and pintle position are normalized. Figure 3 shows the reference thrust profile (blue) for tracking, the simulated realized thrust (red) and the non-monotonic performance funnel (in-time calculated during simulation based on the tracked reference signal). An error feedback with an allowed maximum user defined tracking error of 5% is allowed.

Figure 4 presents the thrust error between commanded and simulated thrust and the performance funnel (first subplot). The second subplot contains the pintle movement. It is obvious that the performance funnel is non monotone and increases the performance funnel automatically to more than the pre-defined tracking error of 5% (see first subplot of Figure 4). This is around the zero thrust command (since the funnel boundary definition must be positive over the whole time). This is visible in Figure 3 with a zoom-in, too.

Figure 6 presents the combustion chamber pressure of the simulation and the simulated thrust – namely the generated thrust of nozzle 1 (blue), generated thrust of nozzle 2 (red) and the combined thrust (green) of both nozzles for the overall system (e.g. an ACS). Figure 5 shows the control input and the gain.

IV. CONTROL ALGORITHMS

The design of the control algorithm is closely connected to the non-linear behavior of the system and its various operational phases, which require different control philosophies all realized within a single controller. Hence, the proper physical understanding of these phases and their accurate modeling can be regarded as the corner stone of the control algorithm.

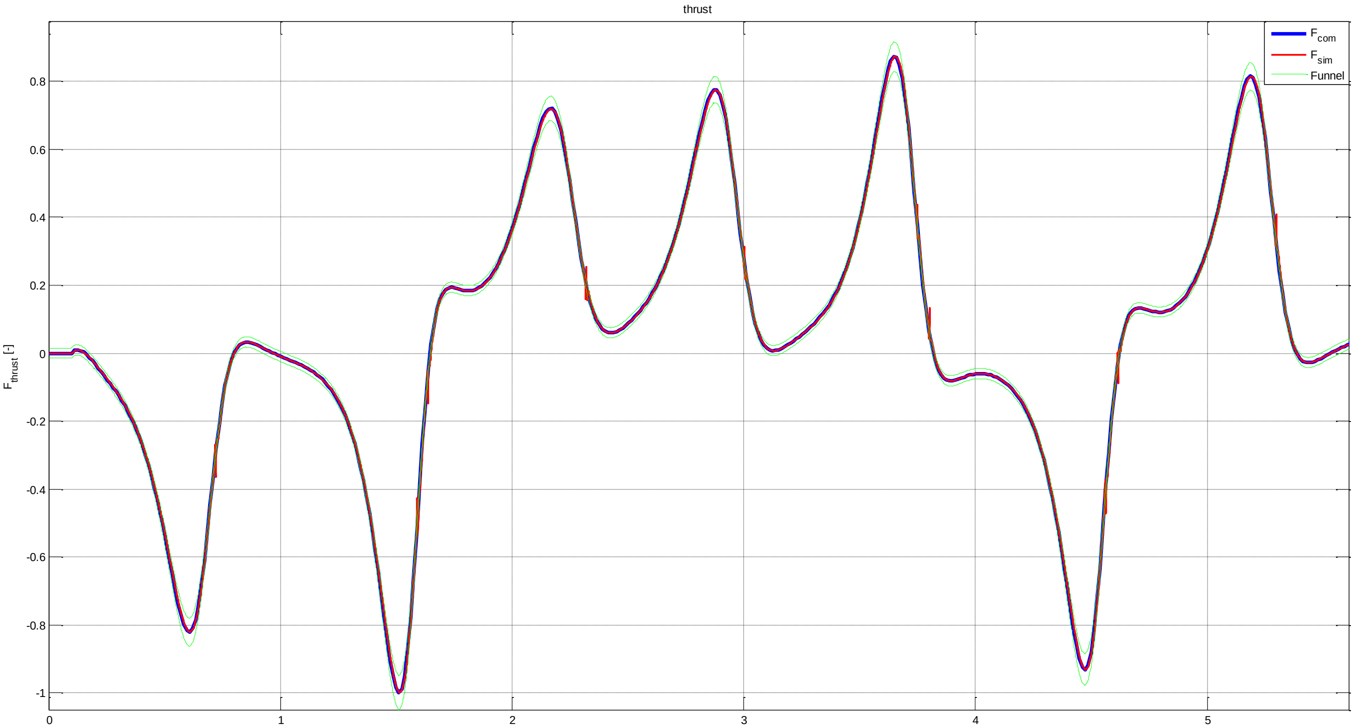

Figure 3: simulation: commanded and simulated thrust (normalized)

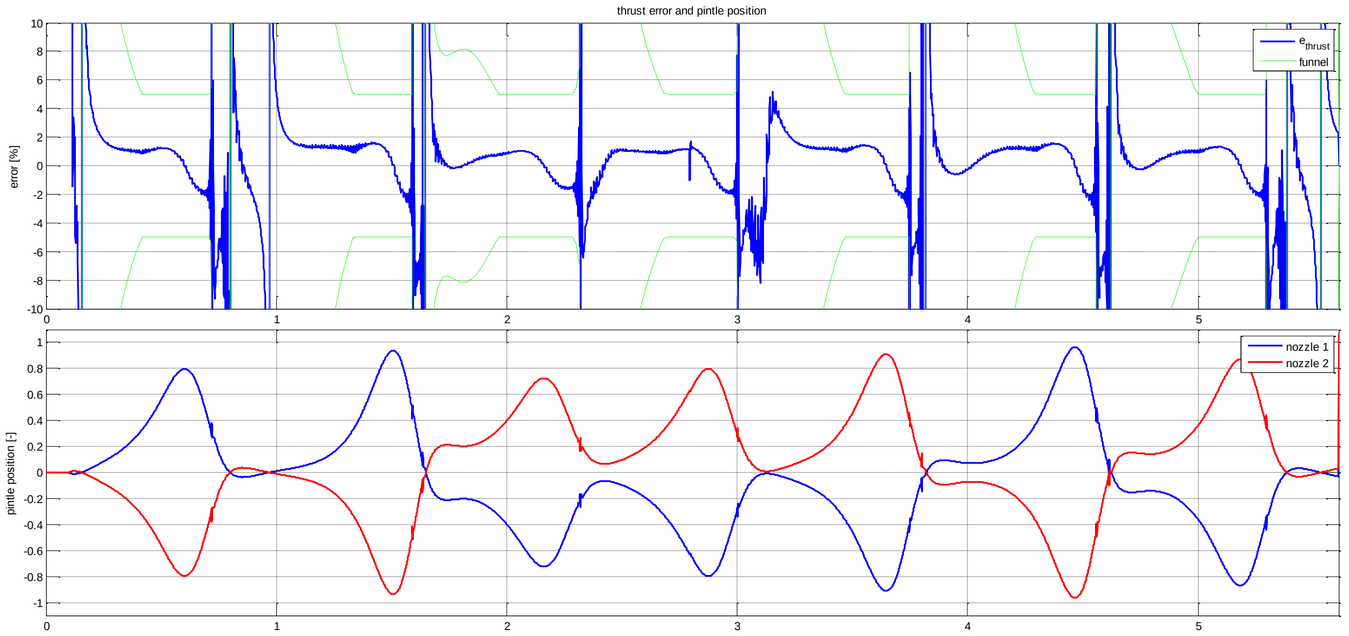

Figure 4: simulation: thrust error and pintle position (normalized)

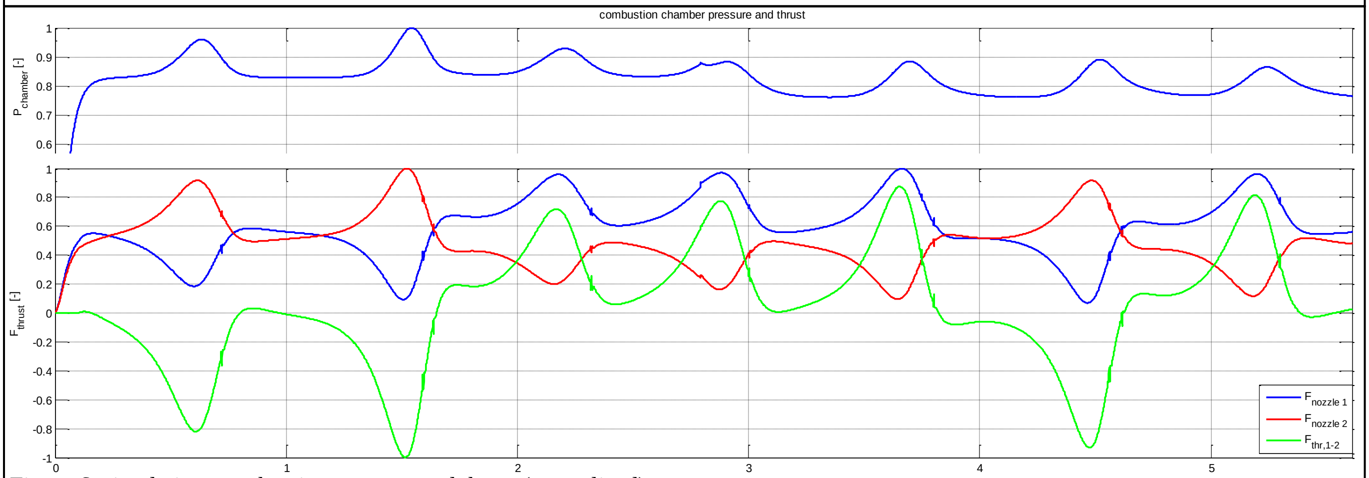

Figure 6: simulation: combustion pressure and thrust (normalized)

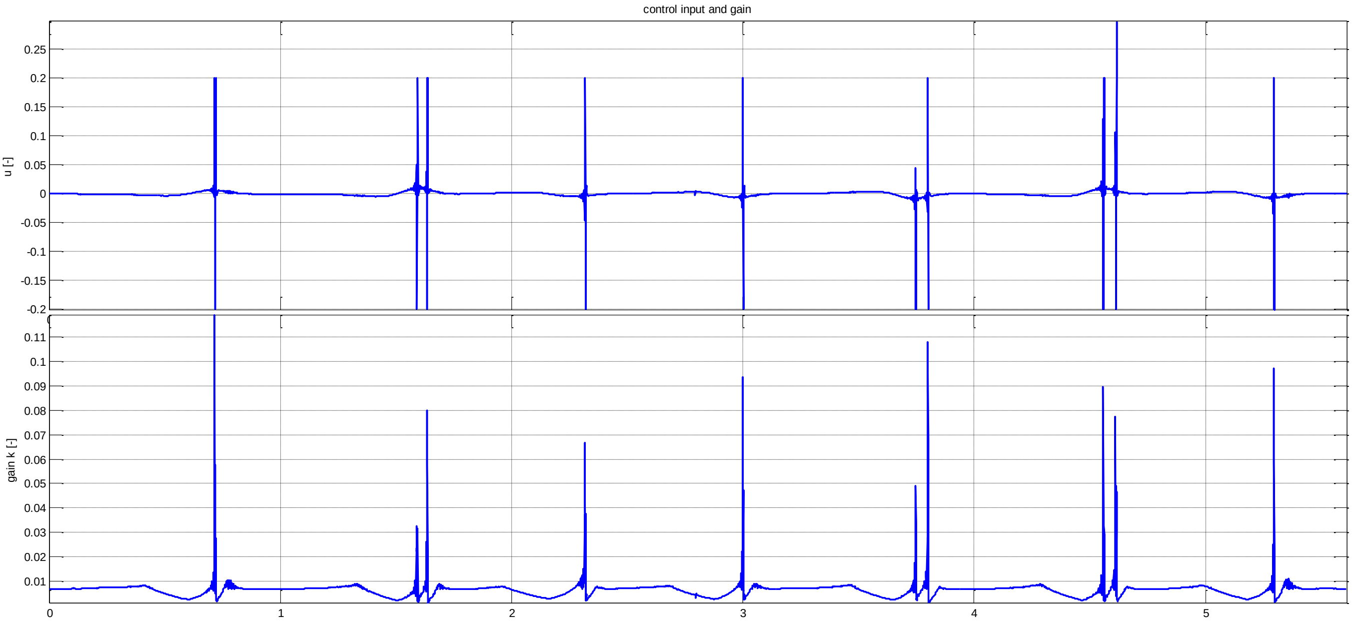

Figure 5: simulation: control input u and gain k

The main objective of the controller is to modify the controllable parameters (i.e. the actuator position) such that a certain command thrust is achieved without endangering the system's physical stability.

The controller has to monitor and react to changes in the system even if the demand thrust remains unchanged. Typical examples are changes in material geometry and elastic deformations with implications on the thrust performance. This means that the control algorithms have to monitor constantly all the relevant system parameters and adapt the actuator position continuously.

The aim is to track a reference signal (e.g. the pre-defined thrust profile) in the context of input and output systems in the presence of input control. The investigated method is a pre-specified parameterized performance funnel. The tracking error is required to evolve within the funnel: transient and asymptotic behavior of the tracking error is influenced through the choice of parameter values which define the funnel. The proposed structure is an error feedback wherein the gain function evolves so as to preclude contact with the funnel boundary.

A feasibility condition (formulated in terms of the funnel data and the reference signal) can be formulated under which the tracking objective is achieved, whilst maintaining boundedness of all signals. The performance funnel evaluates system reliability and technical performance such that it allows a better orientation, more accurate matching and a better control of the parameter influence on the results.

[ESAIM2002] assumes arbitrary small time steps inside the proof of the main theorem. In real applications, the time step is limited to a minimum given by the sensor measurement system, actuator response time and the overall software/hardware delay.

Thus, a direct application of the funnel controller from [UVIL2010] is not possible. The well-known performance funnel concept was extended for use in applications with discrete time steps given by the used hardware.

V. MATHEMATICAL MODEL

Simulation models predict general system behavior as represented by speed, performance or reaction times by solving the respective equations of the system's dynamics. The aim is to improve the operational effectiveness of a system through modeling and simulation. Figure 7 shows the model structure of the current ASC design which covers system dynamics, sensors to track the realized system thrust, a guidance law to generate the a-priori actuator commands, a propulsion model and a controller to achieve the desired thrust response to the guidance commands (actuator, pintle, thrust control).

As seen in Figure 7, the model is divided into different components – the propulsion gas supply, actuators, sensors, disturbances, thrust control, actuator controller and transformations. The closed-loop nature of the simulation shows the connectivity between the different model components. The propulsion supply system includes a propellant burning model, different flow models, description of the nozzle, pintle and actuator behavior as a function of time constants, combustion pressure, used propellant gas and ambient conditions. The system contains a large number of sub-components of which Figure 7 gives only a limited overview. The reference thrust follows a pre-specified profile, e.g. the chaotic 3-dimensional Lorenz system.

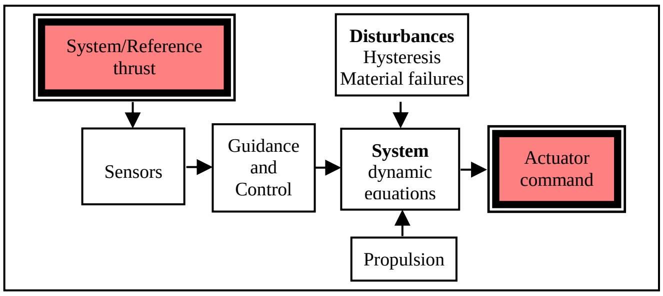

Figure 7: Model structure

The kinematic and dynamic equations model the system under the influence of the actuator behavior, disturbances and the thrust forces produced by the propulsion supply system. Actuator commands and combustion pressure interaction and any other effects caused by actuators or signal processing are included.

In view of precision, speed and ability to respond of the ACS, the characteristics of the ACS and propulsion system are analyzed and computational tools are developed. Numerical simulations with a dynamic model are carried out to investigate the behavior.

In order to predict the thrust response of a controlled ACS, a mathematical model with several subclasses describes the dynamic of all components. The code can be easily integrated in applications or used as standalone program, e.g. when performing adapted performance simulations within a pre-existing database of actuator and nozzle data.

The dynamic equations of the model describe the performance and reaction time of the system (see (2)). The variables in (2) are explained in the nomenclature section at the end of this paper. Note that $\rho_{\text{combustion}}(\cdot)$ and $\dot{r}_{\text{burn}}(\cdot)$ depend on $P_{\text{combustion}}(\cdot)$. For simplicity, since the correct mathematical space definition and initial values formulation are complex, the functional definition space of the right hand side of (2) is sloppy at this point.

Note that the equations of (2) are a non-linear state space representation of the thrust simulation model. The full non-linear equations are used, integrated and solved for pressure, mass flow, density and volume. In view of (2), some caution is required in formulating the existence of a unique global solution, i.e. defined on $\mathbb{R}_{\geq 0}$. A straightforward formulation proves the existence and uniqueness of a global solution which is a major step for a prediction model. Standard theory of ordinary differential equations (see [WALT1998], Th. III.10.VI) yields existence and uniqueness of a maximal solution of the initial value problem (2).

$$\left.\begin{aligned}
\dot{m}_{combustion}(\cdot) &= \dot{m}_{throat}(\cdot) + \frac{d\left(\rho_{combustion}(\cdot)V_{combustion}(\cdot)\right)}{dt} \\
\frac{dV_{combustion}(\cdot)}{dt} &= A_{burning}(\cdot)\dot{r}_{burn}(\cdot) \\
\frac{d\rho_{combustion}(\cdot)}{dt} &= \frac{\frac{dP_{combustion}(\cdot)}{dt} - \frac{2P_{combustion}(\cdot)}{c^*(\cdot)}\frac{dc^*(\cdot)}{dt}}{\left(c^*(\cdot)\sqrt{\gamma}\left(\frac{2}{\gamma+1}\right)^{\frac{\gamma+1}{2(\gamma-1)}}\right)^2} \\
\frac{dP_{combustion}(\cdot)}{dt} &= \frac{\left(c^*(\cdot)\sqrt{\gamma}\left(\frac{2}{\gamma+1}\right)^{\frac{\gamma+1}{2(\gamma-1)}}\right)^2}{V_{combustion}(\cdot)}\left(\rho_{propellant}(\cdot) - \rho_{combustion}(\cdot)\right)A_{burning}(\cdot)\dot{r}_{burn}(\cdot) \\
&\quad - \frac{\left(c^*(\cdot)\sqrt{\gamma}\left(\frac{2}{\gamma+1}\right)^{\frac{\gamma+1}{2(\gamma-1)}}\right)^2}{V_{combustion}(\cdot)}\frac{P_{combustion}(\cdot)A_{throat}(\cdot)}{c^*(\cdot)} + \frac{2P_{combustion}(\cdot)}{c^*(\cdot)}\frac{dc^*(\cdot)}{dt}
\end{aligned}\right\} \quad (2)$$

Traditional control techniques use a linearized state space form of (2) which may not be carried out in appropriate detail and may leave useful information/effects unconsidered.

The controller of the ACS thrust simulation model converts guidance commands into respective pintle position commands – more precisely, into actuator position commands to control the fuel mass flow direction from the gas supply system to the nozzles – in order to realize the required thrust level and direction needed for the intended missile maneuver. The resultant dynamics are measured by rate gyros, accelerometers and pressure sensors to design a non-adaptive feedback control system that tracks the a-priori defined thrust curve (e.g. the output of the chaotic Lorenz system).

As control system, the performance funnel is used [RTO2012]. The performance funnel ensures that the pre-specified transient behavior of the thrust generation and direction with respect to the reference profile is simpler than an adaptive controller insofar as the gain is not dynamically generated and does not invoke any internal model (see [RTO2012]).

VI. PERFORMANCE FUNNEL

Within this chapter the extension of the introduced funnel controller is discussed (see [IFAC2013], [RTO2012]) focusing on the practical, technical implementation of this control algorithm on an ACS in an uncontrolled environment.

A significant number of control algorithms that apply to dynamic inversion, backstepping techniques on simplified state variable models of the dynamics or PID controllers on linearized models in the frequency domain are presented in the literature (see [IEEE2004], [IEEE2007]). Here it is shown that if the practical non-linear time domain implementation is done correctly, even the simple non-monotone gain funnel controller can ensure the stability of the thrust direction and the thrust control (i.e. motor thrust, thrust direction and tracking error).

In the abstract sense, the complete model (2) can be described by functional differential equations in the presence of multi-input, multi-output systems which can be considered as a system of two interconnected nonlinear subsystems

$$\left.\begin{aligned}
\dot{x}(t) &= f_1\left(x(t), d_1(t)\right) + g\left(u(t)\right) \quad , x(0) = x^0 \\
y(t) &= f_2\left(x(t), d_2(t)\right)
\end{aligned}\right\} \quad (3)$$

where $f_1 \colon \mathbb{R}^n \times \mathbb{R}^p \to \mathbb{R}^n$, $f_2 \colon \mathbb{R}^n \times \mathbb{R}^{\tilde{p}} \to \mathbb{R}^m$ are locally Lipschitz, $d_1(\cdot) \in \mathfrak{L}^\infty(\mathbb{R}_{\geq 0} \to \mathbb{R}^p)$, $d_2(\cdot) \in \mathfrak{L}^\infty(\mathbb{R}_{\geq 0} \to \mathbb{R}^{\tilde{p}})$ are disturbances and $g \colon \mathbb{R}^q \to \mathbb{R}^n$ is the continuous input function. In view of (3), some care is required in formulating the existence of a unique global solution, i.e. defined on $\mathbb{R}_{\geq 0}$ which was discussed before. Momentarily regarding the second subsystem in (3), as an example for the presented application, $\mathrm{y}(\cdot) = F_{thr}(\cdot)$ is a possible representation.

The performance method is formulated in terms of the performance funnel (see Figure 8)

$$F(\varphi) \coloneqq \{(t, \eta) \in \mathbb{R}_{\geq 0} \times \mathbb{R}^m | \varphi(t) \|\eta\| < 1\},$$

determined by a function $\varphi(\cdot)$ which satisfies a Lipschitz condition. It has to be noted that the funnel boundary is given by $\varphi(\cdot)^{-1}$ which contains a potential singularity. Typical funnel prototypes are illustrated in Figure 8.

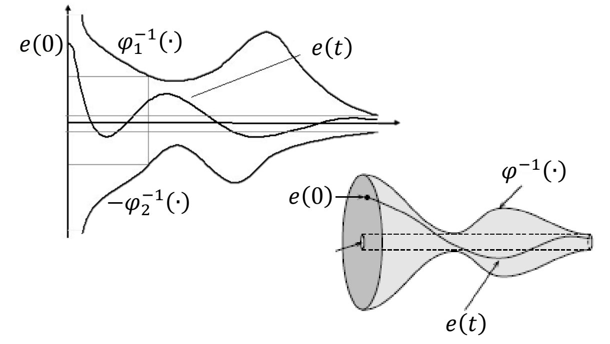

Figure 8: Prototypes of non-/symmetric performance funnels

The control objective is as follows. Determine a feedback structure which ensures that, for a given reference signal $y_{ref}(\cdot) \in W^{1,\infty}(\mathbb{R}_{\geq 0} \to \mathbb{R}^m)$, the output tracking error $e(\cdot) \coloneqq y(\cdot) - y_{ref}(\cdot)$ evolves within the funnel, i.e. $\left\{\left(t, e(t)\right)\right\}_{t \in \mathbb{R}_{\geq 0}} \subset F(\varphi)$: transient and asymptotic behavior of the tracking error is influenced through choice of the function $\varphi(\cdot)$. The proposed structure is an error feedback wherein the gain function evolves so as to preclude contact with the funnel boundary:

given: performance funnel $\varphi(\cdot)^{-1}$ - roughly speaking - $\varphi, \dot{\varphi} \in \mathfrak{L}^{\infty}$

design: gain $k(t) = k\left(t; \varphi(t), y(t), y_{ref}(t)\right)$

such that: for all reference signals - roughly speaking - $y_{ref}, \dot{y}_{ref} \in \mathfrak{L}^{\infty}$
the simple feedback $u(t) = -k(t)\left[y(t) - y_{ref}(t)\right]$ guarantees

- **non-monotone gain** which is simpler then the adaptive gain (not dynamically generated, no internal model)
- asymptotic and **transient behavior**: $y(t) - y_{ref}(t) \leq \varphi(t)^{-1}$
- that the performance funnel is **not restricted** to a specialized system
- **robustness** against input, output and reference noise
- **positivity**: $y(t) \geq 0$ if user/designer requirement

The performance funnel was first introduced in [ESAIM2002] and [UVIL2010] with the goal of achieving better performances than PID controllers in control situations. This is achieved with a basically simpler representation, as unlike a PID controller the funnel does not require a differential equation or internal module. An approach to the simulation model of the performance estimation for the purpose of formal verification and analysis is illustrated.

The performance funnel ensures pre-specified transient behavior of the tracking error, has a non-monotone gain, is simpler than an adaptive controller (insofar as the gain is not dynamically generated), and does not invoke any internal model. The method combines the benefits of two different approaches: the simplicity of adaptive feedback control and an intrinsic high-gain property if necessary. It can be applied directly to the problem without differential equations or an internal model. Two performance evaluation methods are implemented – Euclidean and component wise analysis. The first method uses the Euclidean norm of the output signal (see Figure 8). The second part fits each output signal separately. An allowed corridor for the input is used to fit the reference signals. The simple implementation of the algorithm only uses the input and reference signals.

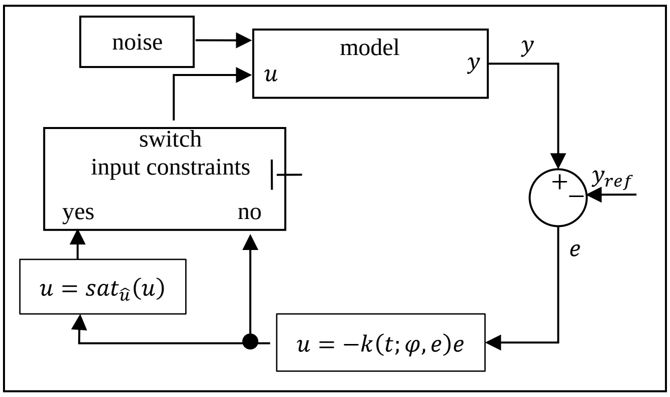

Figure 9: Schematically flow of the funnel based thrust direction control

A wide variety of funnels are possible (see Figure 8). Monotonicity of the funnel boundary is not required. Non-monotone funnels may be advantageous in situations for which it is known a priori when perturbations or set-point changes may occur – in this sense; non-monotone funnels have the connotation of re-initialization of the control structure.

The simplified workflow of the funnel based performance approach for an input output system is shown schematically in Figure 9.

VII. TEST FACILITY DEMONSTRATOR AND TRIALS

Based on requirements like performance, operational time, installation space, total mass etc., a first principal operational ACS design was developed to fulfill the requirements (see Figure 1 and Figure 2). The preliminary concept uses in-house tools, CFD calculations and experimental results for a principle concept of a gas supply system with an actuator concept to move the pintle and meet the performance requirements.

This basic design with all components was implemented and integrated into a simulation environment in Matlab/Simulink including propellant burning model, empirical actuator behavior curves, nozzle and pintle shapes to realize a simulation and performance prediction model to simulate the overall performance of the system, to identify and optimize key driver components, to do sensitivity studies (e.g. influence of actuator time constant or influence of sensor measurement and data transfer rates etc.) and to validate and verify test facility trials and results.

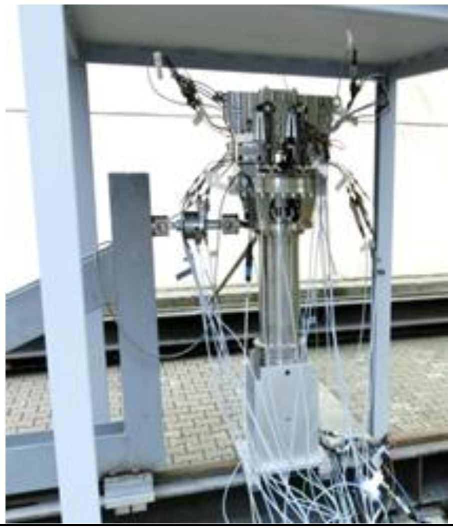

Figure 10: ACS - test facility hardware design

Based on this lightweight design, a test facility hardware concept design (see Figure 10) was generated to fulfill the function of an ACS, but it is more modular and less integrated than a possible flight design to allow the change or modification of parts and has more massive structures in order to allow refurbishment of parts or assemblies or re-use.

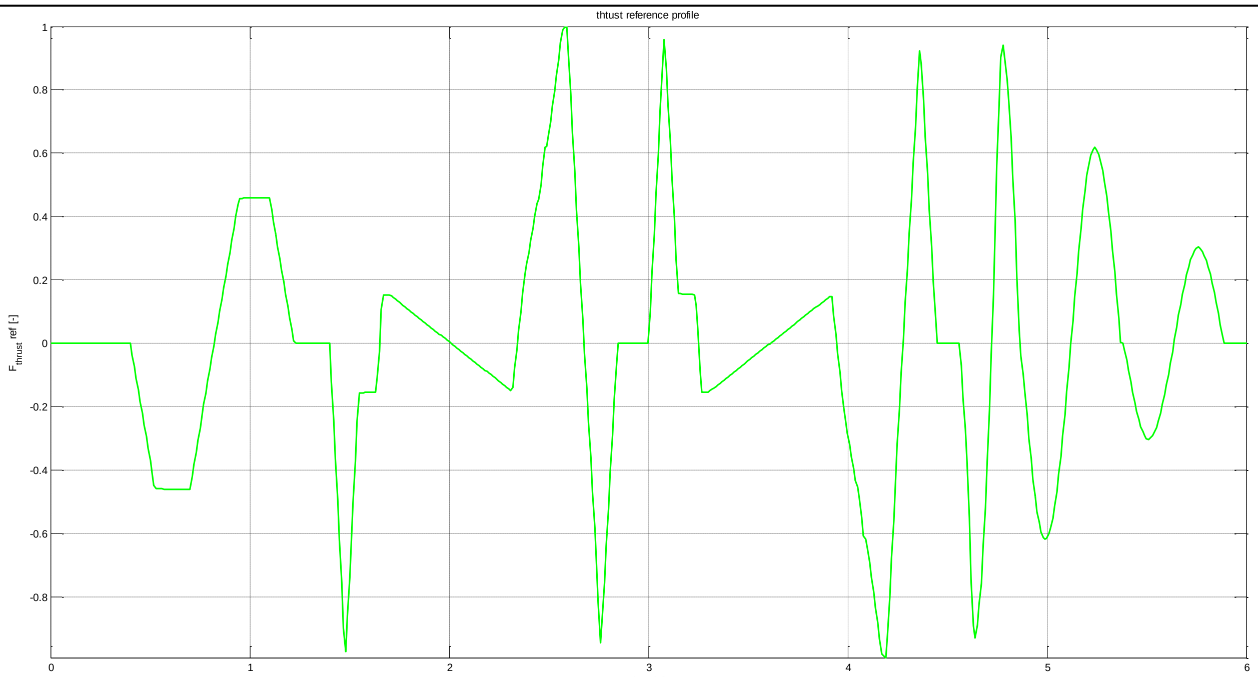

Figure 11: trial: PN reference thrust profile (normalized)

The demonstrator concept is represented by two nozzles for the ACS, i.e. one nozzle plane, with plenum, pintles and an actuator. The full functionality of the ACS can be demonstrated with only 50 per cent of the nozzle numbers and actuators.

The nozzles have a quasi-Cartesian configuration with pintles to control the thrust direction. The actuators are not exposed to the hot gas. Typical test facility actuators are used, i.e. the time constant of the demonstrator is slower than expected for an operational system.

The aims of the test facility trials are to determine the dynamic behavior of the system, validate the accuracy of the design and simulation model, determine actuator forces and confirm the design and technology handling.

For simplicity, coupled pintles are used instead of individual controlled nozzles. This implies a higher propellant mass flow during the trial but reduces the complexity of the system. A complete closure of a nozzle is a harder challenge then a “nearly closed”. Therefore, “nearly closed” nozzles are assumed.

The simulation model and funnel controller implementation is verified by analytical test cases and real test facility trials with an ACS test facility demonstrator based on a flight design. In order to investigate the performance and control algorithm of the controlled ACS, a single trial will be chosen.

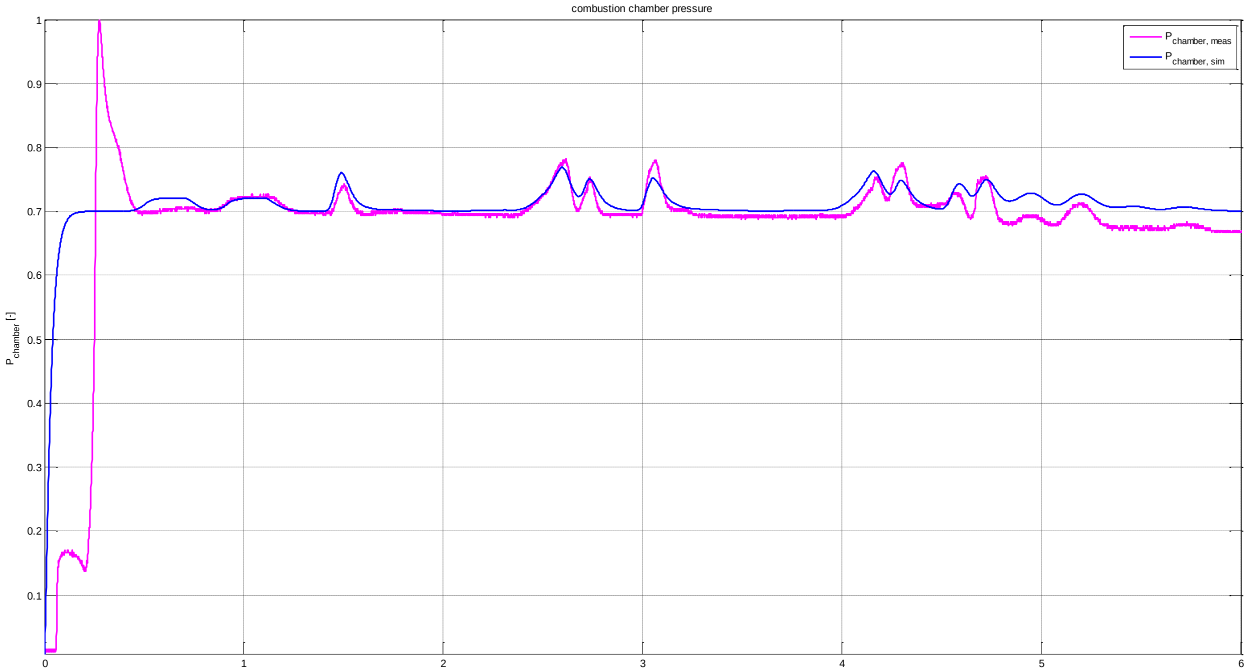

Figure 12: trial: pressure (normalized)

For a standardized classical missile, proportional navigation is a first standard approach for a guidance law and performance studies (e.g. like range, flight time, footprint etc.). The presented trial uses a common thrust reference profile as expected during real flights (see Figure 11). Since the ignition process is not represented inside the simulation model, the reference thrust has the zero command at the beginning to guarantee that the ignition process of the engine is finished.

As a gas supply system, a gelled propellant with a combustion temperature of approximately 2000 K is used since the propellant handling is simpler and cheaper compared to a solid propellant gas generator. For safety reasons, if a failure happens during the trial, the gelled propellant combustion and gas production can be stopped immediately.

The graphs of the combustion chamber pressure, thrust and pintle position are normalized. Figure 12 shows the simulated combustion chamber pressure (blue) based on the simulation model and the measured trial pressure (magenta). The ignition process is not represented inside the model which explains the differences between measurement and simulation over the first 0.4s. Afterwards, the fitting between measurement and simulation is good and the pressure movements are visible in both graphs. Some loss of insulation explains the pressure drop at the end of the trial.

Figure 14 shows the commanded, pre-defined reference thrust (blue) as in Figure 11 which shall be tracked by the ACS. The measured thrust of the active controlled system via pintle position and thrust control is in magenta taking into account that the used controller is an inline pre-defined

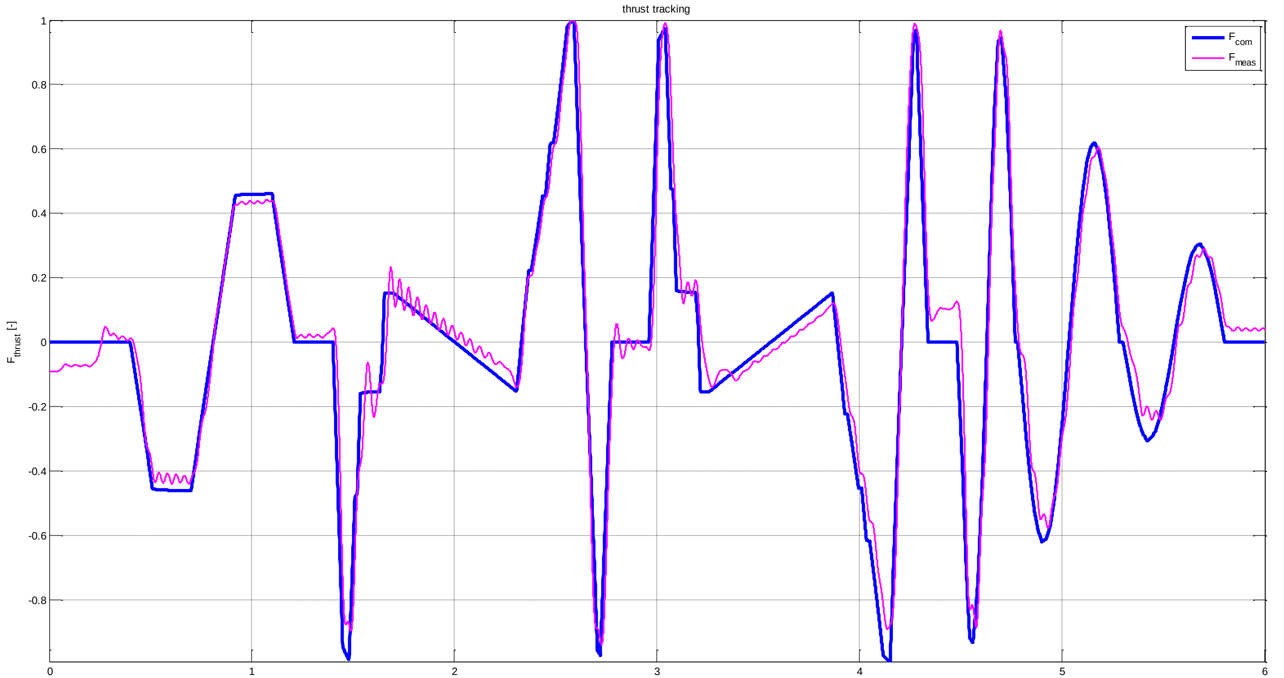

Figure 14: trial: thrust (normalized)

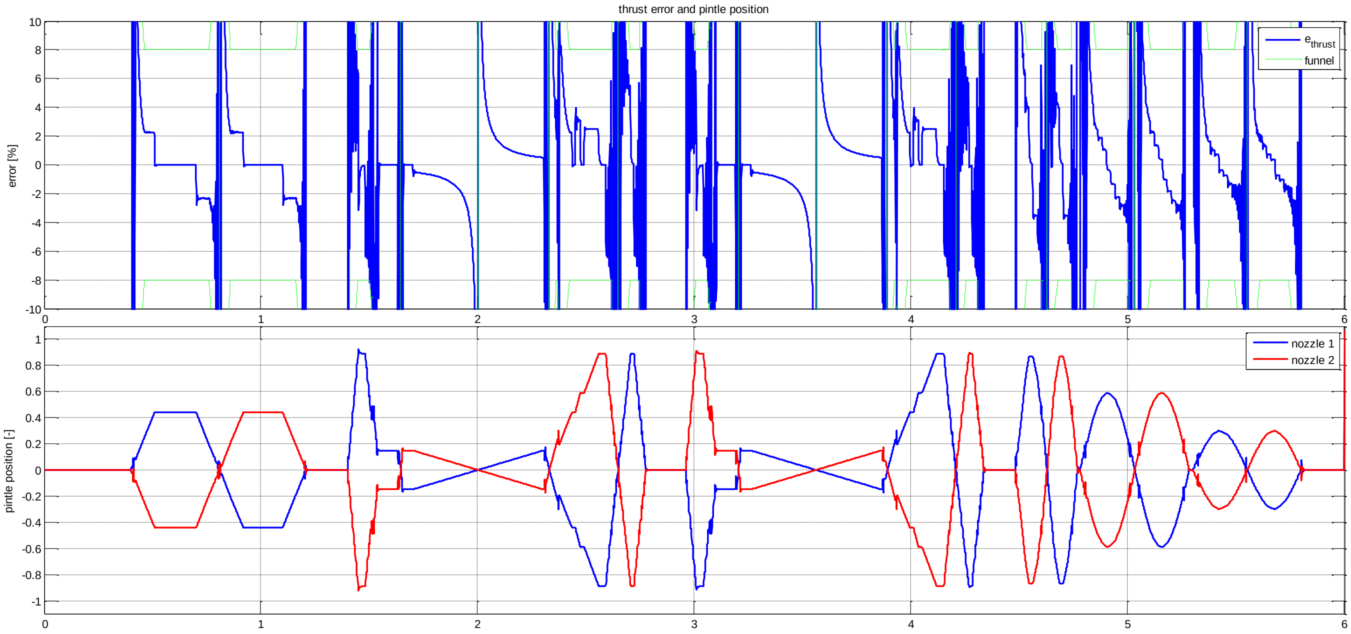

Figure 14: trial: error between measured thrust and reference thrust

performance funnel. As seen in Figure 8, the test facility demonstrator has an oscillation capability and no integrated damper which would have an influence to the thrust measurement. Therefore, the main focus is not on the measured thrust curve in absolute values but on the qualitative behavior and the control handling and reaction. It can be seen that the introduced funnel controller can guarantee the system control, material dispersions (e.g. insulation loss, erosion etc.), oscillation events and actuator delays.

Figure 14 presents the thrust error between commanded and measured thrust and the performance funnel (first subplot). Through the oscillation capability and no integrated damper, the user allowed pre-defined error range is 8 %. Most of the time, the tracking error is less than 4 %. As explained in subsection III, the performance funnel is non monotone and the algorithm increases the performance funnel automatically to more than the pre-defined tracking error (see first subplot of Figure 14).

The second subplot contains the pintle movement. Note that a mechanical actuator has a reaction time for a new commanded position.

Figure 15 shows the control input and the gain. A zoom-in shows that the control input u(·) is smaller than 0.05 in absolute values. This means that the tracking is fast and immediately such that no large control inputs are necessary. Moreover, the gain is not constant and the intrinsic high gain property is obviously, i.e. the gain is large if necessary and otherwise small.

VIII. CONCLUSION

The combination of increasingly complex and expensive hardware and constrained military budgets results in the fact that it is not economically feasible to test a system for the entire possible range of operations or with different designs. A precise model of the performance, certified by trials that can be used to predict system performance accurately for all operating points or updated subcomponents is essential. Especially the controller design and the modeling accuracy and reliability are very important constituents of the missile or rocket engineering design.

This paper presented the main components of a simulation control system applied to an ACS. A main issue was to prove that such a complex system can be controlled using a pre-defined performance funnel. A linearized simulation model, transfer functions or frequency-domain descriptions are not necessary.

The tracking error is required to evolve within the funnel: transient and asymptotic behavior of the tracking error is influenced through choice of parameter values which define the funnel. The proposed structure is an error feedback wherein the gain function evolves so as to preclude contact with the funnel boundary. A feasibility condition (formulated in terms of the funnel data and the reference signal) can be formulated under which the tracking objective is achieved, whilst maintaining boundedness of all signals. The performance funnel evaluates system reliability and technical performance so as to allow a better orientation, more accurate matching and a better control of the parameter influence on the results.

The presented performance funnel controller guarantees a transient behavior for the missile. Since the performance method is described by generic functions, a large range of models can be analyzed. The implemented funnel algorithm allows the optimization of both – the geometrical shape of the pintle nozzle system and actuator parameters with respect to given requirements.

As explained in the algorithmic description, the maximum allowed error of the tracked parameter (e.g. thrust) is user defined. The maximum allowed error has to be high enough as that a physically meaningful solution can be obtained.

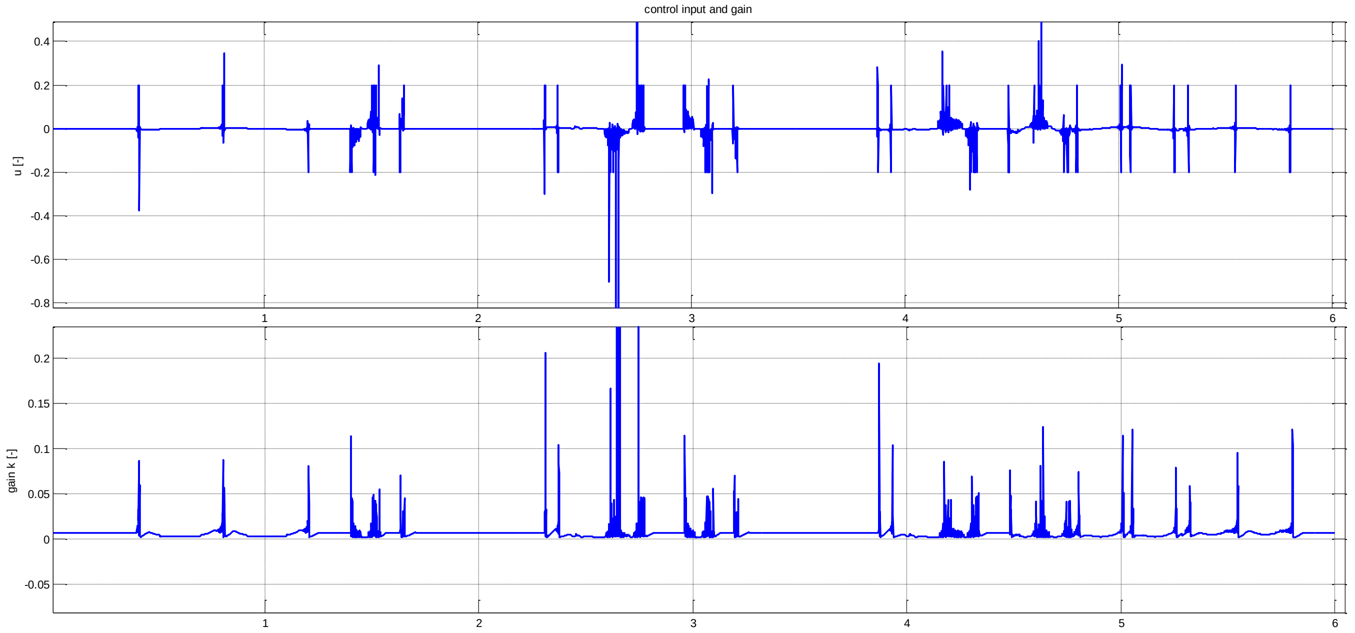

Figure 15: trial: gain k and control input u

NOMENCLATURE

ACS	Attitude Control System
CoG	Centre of Gravity
GG	Gas Generator
PID	Proportional Integral Differential (Controller)
PN	Proportional Navigation
RJ	Ram Jet
TDR	Throttleable Ducted Rocket
$A_{burning}(\cdot)$	burning area of the propellant
$A_{throat}(\cdot)$	pintle position dependent nozzle throat area
$c^*(\cdot)$	characteristic velocity of the gas
$F_{thr}(\cdot)$	thrust
γ	heat specific value
$\dot{m}_{combustion}(\cdot)$	mass flow rate due to propellant combustion
$\dot{m}_{throat}(\cdot)$	mass flow rate exiting the nozzle
$\dot{r}_{burn}(\cdot)$	burn rate of the propellant
$P_{combustion}(\cdot)$	combustion chamber pressure
R	universal gas constant
$\rho_{propellant}$	density of the propellant
$\rho_{combustion}$	gas density in the combustion chamber
$T_{combustion}(\cdot)$	combustion chamber temperature
$V_{combustion}(\cdot)$	combustion chamber volume
$\mathbb{R}, \mathbb{R}_{\geq 0}$	space of (non-negative) real numbers
$\mathfrak{L}^\infty(\mathbb{R}_{\geq 0} \to \mathbb{R}^m)$	measurable and essentially bounded functions
$\mathrm{W}^1(\mathbb{R}_{\geq 0} \to \mathbb{R}^m)$	bounded locally absolutely continuous functions with essentially bounded first derivative

REFERENCES

[ESAIM2002] A. Ilchmann, E.P. Ryan and C.J. Sangwin, Tracking with prescribed transient behavior, *ESAIM: Control, Optimisation and Calculus of Variations*, Volume 7, 2007, p. 471–493

[IEEE2004] P. Castillo, A. Dzul and R. Lozano, Real-time stabilization and tracking of a four-rotor mini rotorcraft, *IEEE Transactions on Control Systems Technology*, Volume 14, Issue 4, 2004, p. 510–516

[IEEE2007] S. Bouabdallah and R. Siegwart, Full control of a quadrator, *IEEE/RSJ International Conference on Intelligent Robots and Systems*, 2007, p. 153-158

[IFAC2013] N. Hopfe and P. Caldas-Pinto and G. Kurth, Funnel Control for systems with relative degree two, *IFAC Automatic Control in Aerospace*, Volume 19, Issue 1, 2013, p. 125–130

[ROMA2009] E. Cavallini, *Modelling and Numerical Simulation of Solid Rocket Motors Internal Ballistics*, Ph.D., Sapienza Universita di Roma, 2009

[RTO2012] C. Bauer and N. Hopfe and P. Caldas-Pinto and F. Davenne and G. Kurth, Advanced Flight performance Evaluation Methods of Supersonic Air-Breathing Propulsion System by a Highly Integrated Model Based Approach, *RTO AVT-208 Symposium*, RTO-MP-AVT-208, San Diego, 2012

[SIAM2013] C. Hackl and N. Hopfe and A. Ilchmann and M. Mueller and S. Trenn, Funnel Flight Controller for a TDR 6-DoF Simulation Model, *SIAM J. of Control and Optimization*, Volume 51, Issue 2, 2013, p. 965–995

[SPAR1982] C. Sparrow, *The Lorenz Equations: Bifurcations, Chaos, and Strange Attractors*, Number 41 in Applied Mathematical Sciences, Springer-Verlag, 1982

[TAM2004] D.S. Stewart, K.C. Tang, S. Yoo, M.Q. Brewster and I.R. Kuznetsov, Multiscale modeling of solid rocket motors: Time integration methods from computational aerodynamics applied to stable quasi-steady motor burning, TAM report no. 1054, Theoretical and Applied Mechanics, University of Illinois at Urbana-Champaign, 2004

[UVIL2010] N. Hopfe, *Feedback control: systems with higher unknown relative degree, input constraints and positivity*, Universitäts-Verlag Ilmenau, 2010

[WALT1998] W. Walter, *Ordinary Differential Equations*, Springer, New York, 1998

[WILE2001] G. P. Sutton and O. Biblarz, *Rocket Propulsion Elements*, 7nd edition. John Wiley & Sons, 2001

Journal of Energy Challenges
and Mechanics
http://www.nscj.co.uk/JECM/

ISSN 2056-9386
Volume 3 (2016) issue 2, article 6

A review of materials science research pathways and opportunities for building integrated photovoltaics

光伏建筑一体化之材料科学研究途径与机遇述评

Bjørn Petter Jelle[1,2*], Serina Ng[2], Tao Gao[1], Sohrab Alex Mofid[1] and Tore Kolås[3]

[1]*Norwegian University of Science and Technology (NTNU), Department of Civil and Transport Engineering, NO-7491 Trondheim, Norway.*
[2]*SINTEF Building and Infrastructure, Department of Materials and Structures, NO-7465 Trondheim, Norway.*
[3]*SINTEF Materials and Chemistry, Department of Materials and Nanotechnology, NO-7465 Trondheim, Norway.*

[*]*Corresponding author: bjorn.petter.jelle@sintef.no (e-mail), +47-73593377 (phone).*

Accepted for publication on 3rd August 2016

Abstract - **Building integrated photovoltaics (BIPV) represent a powerful and versatile tool for achieving the ever-increasing demand for energy-efficient and energy-harvesting buildings of the near future. The BIPV systems offer an aesthetical, economical and technical solution to integrate solar cells harvesting solar radiation to produce electricity being an integral part of the climate envelopes of buildings. Building integration of photovoltaic (PV) cells are carried out on sloped roofs, flat roofs, facades and solar shading systems, where the BIPV systems replace the outer building envelope skin, thus serving simultaneously as both a climate screen and a power source generating electricity. Hence, BIPV may provide savings in materials and labour, in addition to reducing the electricity costs. Nevertheless, in addition to specific requirements put on the solar cell technology, as the BIPV systems act as the climate protection screen it is of major importance to have satisfactory requirements on rain tightness and durability, where various building physical issues such as heat and moisture transport in the building envelope also must be considered and accounted for. Research within materials science in general and within PV technology may enable and accelerate the development of highly innovative and efficient BIPV materials and systems. Sandwich, wavelength-tuned, dye-sensitized, material-embedded concentrator, flexible (e.g. copper indium gallium selenide CIGS and cadmium telluride CdTe), thin amorphous silicon, quantum dot, nanowire, brush-paint and spray-paint solar cells, different surface technologies and various combinations of these are examples of possible research pathways for PV and BIPV. From a materials science perspective, this work presents a review bridging the path from the current state-of-the-art BIPV to possible research pathways and opportunities for the future BIPV.**

Keywords - **building integrated photovoltaics, BIPV, solar cell, materials science, surface.**

I. INTRODUCTION

The demand for energy-efficient and energy-harvesting buildings is growing, hence initiating the exploration of miscellaneous solutions. Building integrated photovoltaic (BIPV) systems are increasing in popularity and usage as they represent a powerful and versatile tool for achieving the ever increasing demand for zero energy and zero emission buildings of the near future, hence providing an aesthetical, economical and technical solution to integrate solar cells to become an integral part of the exterior climate envelopes of buildings.

Building integrations of photovoltaic (PV) cells are carried out on sloped roofs, flat roofs, facades and solar shading systems, thus replacing the outer building envelope skin and hence serving simultanously as both a climate screen and a power source generating electricity.

That is, BIPV may provide savings in materials and labour, in addition to reducing the electricity costs. Nevertheless, in addition to specific requirements put on the solar cell technologies, it is of major importance to have satisfactory requirements on rain tightness and durability, where various climate exposure factors and building physical issues such as heat and moisture transport in the building envelope also have to be considered and accounted for.

The aim of this work is to present from a materials science perspective an overview and bridge the path from the state-of-the-art BIPV systems of today to possible research opportunities for making the BIPV solutions of tomorrow.

II. STATE-OF-THE-ART BIPV SYSTEMS

The BIPV product range is very wide, and the BIPV products or systems may be categorized in different ways, e.g. as foil, tile, module and solar cell glazing products. On the other hand, building attached (applied/added) photovoltaics (BAPV) are regarded as add-ons to the buildings, thus not replacing the traditional building parts as BIPV systems are doing. Examples of BIPV tiles on building roofs are shown in Fig.1 [1,2]. Furthermore, two different BIPV products are depicted in Fig.2 [3,4]. For an overview and detailed information of state-of-the-art BIPV products it is referred to earlier studies [5,6].

Fig.1. Examples of BIPV tiles on building roofs, Solar Thermal Magazine (left) [1] and Applied Solar (right) [2].

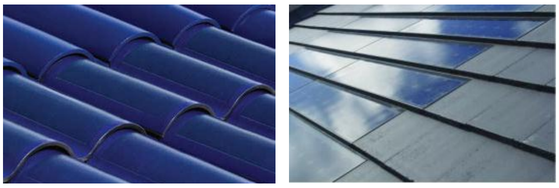

Fig.2. BIPV tile products, SRS Energy (left) [3] and Solar Century (right) [4].

III. MATERIALS SCIENCE RESEARCH PATHWAYS

3.1. IMPACT ON BIPV FROM PV DEVELOPMENT

The development of PV materials and their technologies may have an even stronger impact on the BIPV development in the years to come. This will especially be valid if one from the PV based research is able to tailor-make solar cell materials and solutions for building integration [7,8]. In Fig.3 there is given a timeline for reported best research-cell efficiencies, depicting all verified records for different PV conversion technologies [9].

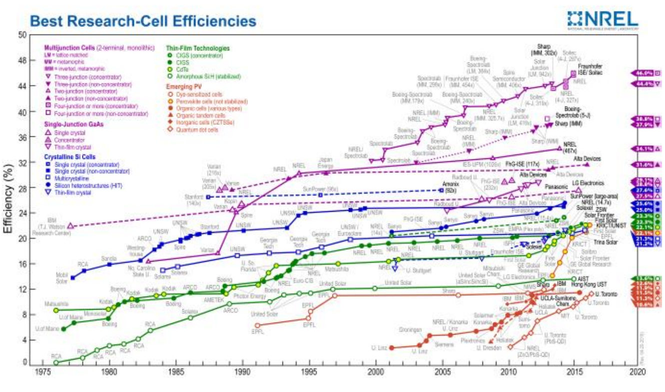

Fig.3. Timeline for reported best research-cell efficiencies (enlarge digitally to see details) [9].

The miscellaneous PV conversion technologies given in the overview in Fig.3 include crystalline Si, thin film, single-junction GaAs, multijunction and emerging technologies, and are collected from solar companies, universities and national laboratories [9].

Ongoing experimental studies range from those with more focus on pure materials science, e.g. quantum dots [10], to the more device focused ones, e.g. ceramic tiles [11].

3.2. HIGH-PERFORMANCE SOLAR CELLS

Research laboratories have for many years produced high-performance solar cells with efficiencies up to 25-40 %. One approach is to use materials with higher purity and to eliminate the impurities along in the process. The back surface can be passivated with silicon oxide and amorphous silicon to minimize recombination losses at the surfaces and contacts. Furthermore, textured surfaces and buried contacts with minimal shading reduce optical losses. The total production is very expensive.

High-performance solar cells may also be made as solar cell concentrators or concentrated photovoltaic (CPV) cells. The highest solar cell efficiency for a CPV cell is currently 46.0 % in 2016 (see Fig.3).

3.3. ABSORBING NON-VISIBLE SOLAR RADIATION

A system for harvesting solar radiation has been developed, using small organic molecules that are tuned to absorb specific non-visible wavelengths (i.e. ultraviolet and near infrared) of solar radiation and letting the visible solar radiation pass straight through (Fig.4), thus resulting in a solar cell able to produce electricity while still allowing people to see through a clear glass with no colour distortions [12]. Thereby, solar energy may be harvested by windows which apparently look like normal and clear windows.

Fig.4. Solar harvesting tuned to absorb specific non-visible wavelengths of solar radiation and letting visible solar radiation pass straight through [12].

3.4. SANDWICH SOLAR CELLS

Sandwich or stack solar cells use several different material layers and cells with different spectral absorbances to harvest as much as possible of the solar radiation in a wide wavelength range. As an example, Fig.5 [13] shows a triple solar cell that has a top cell layer which absorbs the blue light and allows the other wavelength parts of the solar radiation to pass through. The green and yellow light ranges are then absorbed by the middle cell layer, and the red light is absorbed by the bottom cell layer. Hence, a much larger portion of the solar radiation may be utilized.

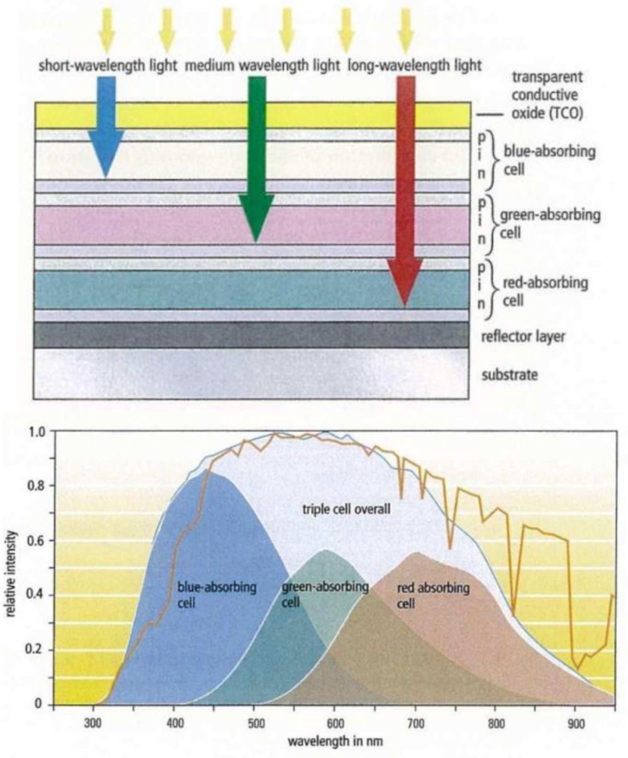

Fig.5. A triple solar cell with its configuration (top) and spectral responses (bottom) [13].

3.5. POLYMER SOLAR CELLS

Ultra-low cost and low-medium efficiency organic based modules are based on dye sensitized solar cells (DSSC), extremely thin absorbers, organic polymer cells and others. Organic semiconductors are less expensive than inorganic ones. The highest reported efficiency for an organic solar cell (with the exception of DSSC) was 6.5 % in 2007 and has now reached 11.5 % in 2016 (see Fig.3). However, polymer solar cells are more sensitive to degradation, where ultraviolet solar radiaion and oxygen from the atmosphere may oxidize the organic layer.

3.6. DYE SENSITIZED SOLAR CELLS

Dye sensitized solar cells (DSSC) have solar radiation absorbing dyes usually deposited onto a titanium dioxide (TiO_2) substrate material like in the Grätzel solar cell. The schematic structure and band diagram for DSSC are depicted in Fig.6 [14,15].

The DSSC technology is often compared with and stated to imitate the photosynthesis, and is by Grätzel called ”the artificial leaf”. The cells absorb across the visible spectrum and therefore lead to an increased efficiency ranging from 7 % under direct solar irradiation (AM1.5) and up to 11 % in diffuse daylight. The TiO_2 material is a renewable and non-toxic white mineral, thus giving smaller environmental impacts, where an easy manufacturing process contributes to lower costs. The reduced production costs and the decreased environmental impacts result in shorter energy and economical payback time, and therefore makes the DSSC technology very promising. The market share for this technology is still very small, but it is expected to rise and may achieve a great influence in the future.

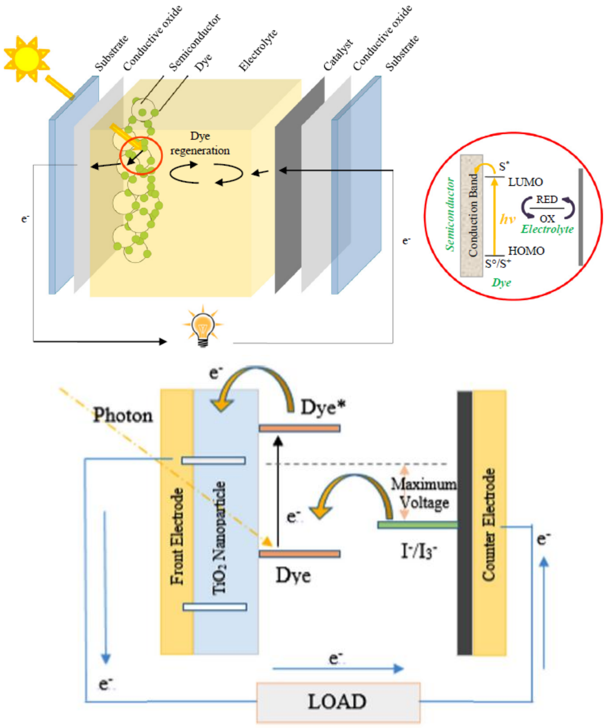

Fig.6. DSSC schematic structure (top [14]) and band diagram (top [14] and bottom [15]).

3.7. ANTENNA-SENSITIZER SOLAR CELLS

So-called solar cell ”antennas” may harvest several wavelengths, i.e. a much broader spectrum of the solar radiation. This technology concept may also be compared to the more ”traditional” sandwich solar cells. ”The use of antenna-sensitizer molecular devices may constitute a viable strategy to overcome problems of light harvesting efficiency in the spectral sensitization of wide-bandgap semiconductors.” [16]. A principle drawing of an antenna-sensitizer solar cell example is depicted in Fig.7 [16].

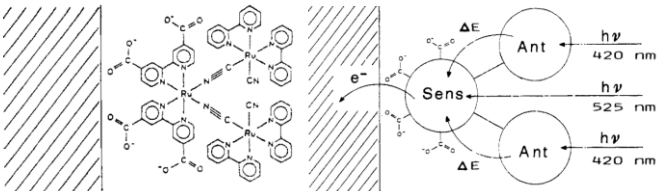

Fig.7. Illustrative representation of the adsorption mode of the trinuclear complex on the TiO_2 surface (left) and block diagram showing the function of the trinuclear complex as an antenna-sensitizer molecular device (right) [16].

3.8. CIGS AND CdTe SOLAR CELLS

Flexible and lightweight CIGS (copper indium gallium selenide) and cadmium telluride (CdTe) solar devices are shown in Fig.8 (principle configuration drawings) and Fig.9 (photos of actual devices), and have yielded an active area efficiency of 14.7 % and 9.4 %, respectively [17]. These flexible and lightweight devices increase the integration flexibility and allow building integration in structures which can not take the additional load of heavy and rigid glass laminated solar modules. ”The flexible solar modules can be laminated to building elements such as flat roof membranes, tiles or metallic covers without adding weight and thus, the installation costs can be reduced significantly.” [17].

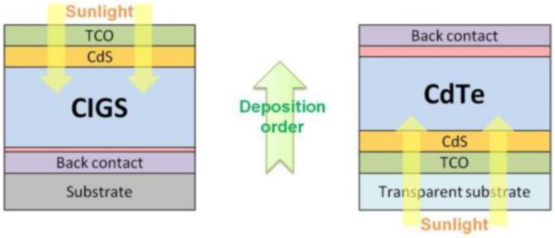

Fig.8. Schematic configuration build-up of CIGS (left) and CdTe (right) thin film solar cells [17].

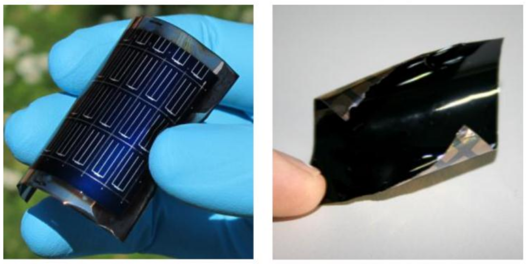

Fig.9. Photos of flexible CIGS (left) and CdTe (right) solar cells on polyimide substrates [17].

The flexibility of CIGS solar cells is also noted by others, e.g. quoting ”Thanks to flexible lamination, CIGS solar cells now have the ability to both realize their potential as the most efficient thin film technology and to dominate the building-integrated photovoltaics (BIPV) market in the future” [18]. A bending test carried out on a CIGS solar cell on flexible borosilicate ultra-thin glass substrate (100 μm) is shown in Fig.10 [19].

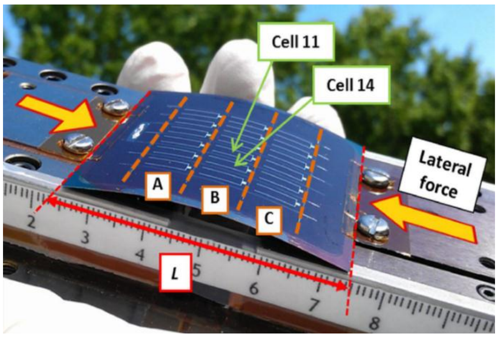

Fig.10. Bending test of a CIGS solar cell on flexible borosilicate ultra-thin glass substrate (100 μm) [19].

3.9. Quantum Dot Solar Cells

Experimental investigations carried out by Semonin et al. [10] have reported photocurrent quantum efficiencies exceeding 100 % in a quantum dot solar cell, being enabled by multiple exciton generation (MEG). The MEG process may occur in semiconductor nanocrystals or quantum dots where absorption of a photon with at least twice the bandgap energy creates two or more electron-hole pairs. In Fig.11 there are shown scanning electron microscope images of TiO_2 nanorods and cadmium sulfide (CdS) quantum dots [20]. For further details, including charge transfer processes between CdS and TiO_2 in a quantum dot nanowire based solar cell, it is referred to the review by Badawy [20]. Hence, miscellaneous new and exciting discoveries within solar cell research may with time find its way into the PV and BIPV systems for the buildings of tomorrow.

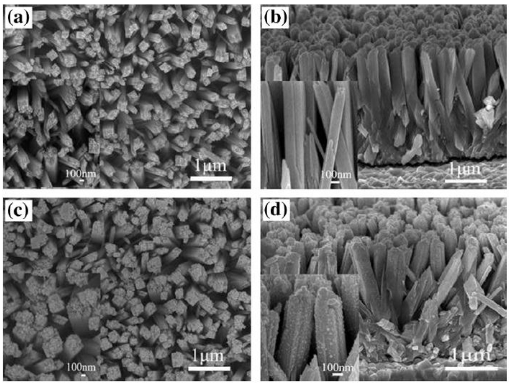

Fig.11. Field-emission scanning electron microscope (FESEM) images of (a) TiO_2 nanorod array (top view), (b) cross-sectional SEM image of TiO_2 nanorod array grown on FTO (fluorinated tin oxide), (c) top and (d) cross-sectional view of CdS quantum dots coated on a TiO_2 nanorod array [20].

3.10. Solar Cell Concentrators

It is possible to envision to be able to make an exterior surface capable of harvesting as much solar energy as if the whole exterior surface was covered with a PV material, while in fact the actual PV material surface is considerably smaller and located somewhat beneath the exterior surface, hence reducing the PV material costs. This may be viewed as a special built-in concentrator system integrated within the PV surface. Hence, the idea may then be to fabricate a ”solar concentrator” at a microscopic material level embedded in the solar cell surface and beneath [5].

A luminescent solar concentrator (LSC) example is depicted in the illustrations given in Fig.12 [21], where first dye-doped polymethylmethacrylate (PMMA) plates were prepared by an in-situ polymerization method and thereafter crystalline silicon solar cells were mounted to the as-prepared dye-doped PMMA plates.

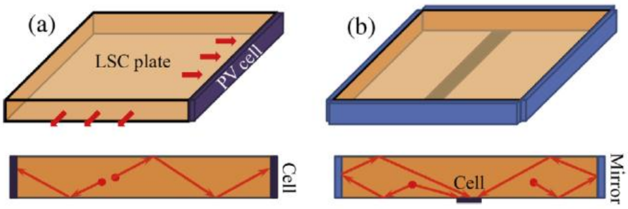

Fig.12. Illustration of a luminescent solar concentrator with (a) side-mounted and (b) bottom-mounted solar cells [21].

Naturally, for solar cell concentrators to be applied as BIPV, it is crucial to make the concentrator dimensions as small as possible, e.g. with respect to the total thickness.

An example still at a macroscale, but nevertheless being part of the ongoing process of reducing the dimensions of solar concentrators, is shown in Fig.13, where the height of the polyurethane (PUR) concentrator element is as small as 25 mm, thereby entitling the authors to name their system as building integrated concentrating photovoltaics (BICPV) [22].

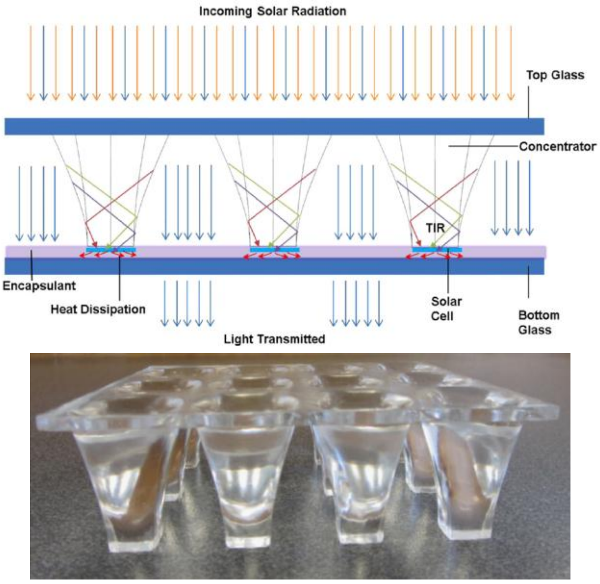

Fig.13. Schematics of a solar concentrator utilizing total internal reflection (TIR) in order to guide the incoming solar radiation to the active solar cell parts (top) and actual concentrator element array made of polyurethane (bottom) [22].

3.11. INVERTED PYRAMID TEXTURING

An illustration of inverted pyramid texturing utilized to harvest more of the incident solar radiation is depicted in Fig.14 [23].

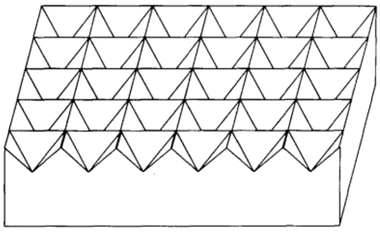

Fig.14. Inverted pyramid geometry texturing utilized for light trapping on Si solar cells [23].

Inverted pyramid geometry texturing of a solar cell surface allows a more effective solar radiation trapping due to the following three effects: (a) reduced front surface reflectance by providing the opportunity for a portion of the incoming solar rays to undergo a triple bounce, (b) increased path length of the solar ray through the cell, thus absorbing a larger fraction of the solar rays which has entered the cell before exiting the cell, and (c) increased amount of solar rays reflected from the back surface, by total internal reflection at the front surface/air interface by making the incident angle greater than the critical angle. Note also the work by e.g. Kang et al. [24] where they have designed an asymmetrically textured structure for efficient solar radiation trapping in BIPV.

3.12. INTEGRATION OF PV IN CONCRETE

A possible option for the future that e.g. Enecolo and SolarPower Restoration Systems Inc. have looked into is to integrate the PV cells in materials at an early stage, e.g. in prefabricated concrete plates [25,26]. Since concrete is one of the most widely used construction materials in the world, and the integration of PV with concrete surfaces has remained largely undeveloped, this research field has a huge potential. Furthermore, note also the BIPV product DysCrete using an organic dye on a concrete surface to harvest solar radiation and generate electricity, the name origin from dye sensitized solar cells and concrete [27,28].

3.13. SOLAR CELL PAINT

Thin laminate and paint layer solar cell materials represent another future option for the PV sector. Obviously, such materials have a huge potential for BIPV applications. Considerably reduced material usage, extremely easy application like brush or spray painting and the fact that nearly any building may easily be coated on any surface are crucial advantages that hold the potential of changing the way photovoltaics are being integrated in buildings. Wear and tear and reduced durability of the solar cell paint layers may be compensated by more frequent maintenance intervals, i.e. repainting, if the costs will be kept sufficiently low for the emerging solar cell paint systems we are just merely catching the very first glimpses of today.

A complete photovoltaic cell was fabricated by Javier and Foos [29] using a handheld airbrush, dilute solutions of cadmium selenide (CdSe) and cadmium telluride (CdTe) nanorods, commercially available silver paint, and transparent-conducting-electrode-coated glass, as illustrated in Fig.15. They explored the suitability of a handheld airbrush to create high-quality films and were able to form ultra smooth surfaces from 20 to 500 nm in thickness. The current estimated efficiency is very low, but the research demonstrates the variety in the potential of PV cells [29]. In this respect, see also the study by Lee et al. [30].

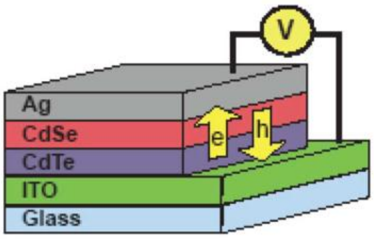

Fig.15. Illustration of a PV cell configuration composed of ITO-coated glass, CdTe and CdSe nanorods, and silver paint. Electrons (holes) are preferentially pushed towards the Ag (ITO) electrode as depicted by the arrows [29].

Moreover, a patternable brush painting process for fabrication of flexible polymer solar cells was investigated by Heo et al. [31], their flexible polymer solar cell being depicted in Fig.16. Furthermore, schematics of a brush painting process to prepare brush-painted flexible organic solar cells are shown in Fig.17, where highly transparent and flexible Ag nanowire electrodes with low sheet resistance were utilized [32]. It is referred to the available literature for other examples of investigations carried out on brush painting, spray coating and flexible solar cells [33-36].

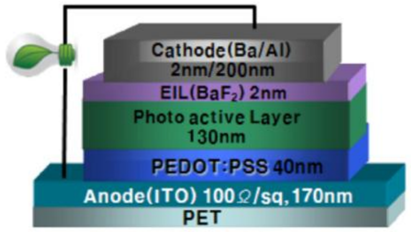

Fig.16. Device structure of a flexible polymer solar cell [31].

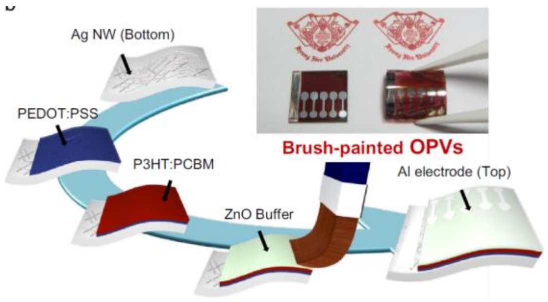

Fig.17. Schematics depicting a brush painting process of preparing brush-painted flexible organic solar cells. The inset photo shows the flexibility of the brush-painted flexible organic solar cells [32].

3.14. HYBRID SOLAR CELLS

Hybrid solar cells are combining various properties of different materials. Typically, they consist of both organic and inorganic semiconductors, where the organics absorb the solar radiation and the inorganics function as the electron transporter. The structure and interface types are of crucial importance for the hybrid solar cells. Often an increased interfacial surface area between the organic and inorganic materials is desired in order to facilitate charge separation and increase the efficiency.

Miscellaneous nanoscale structures like mesoporous inorganic films mixed with organics, alternating inorganic-organic lamellar structures and nanowire structures may be made. Hybrid solar cells exist in many variations and combinations and hence constitute a very broad group of solar cells, where e.g. nanoparticle, nanowire, quantum dot, graphene, carbon nanotube, conjugated polymer, silicon, cadmium telluride, cadmium sulfide, perovskite, titanium dioxide and dye sensitized materials among others are being applied in various devices [37-51].

3.15. ELECTROCHROMIC PV DEVICES

Solar cell glazing products available today have potential for optimization, e.g. the solar radiation utilized in a solar cell cannot be exploited as daylight in the buildings. One possible optimization pathway may be to incorporate electrochromic materials [52-62] with PV materials in completely new and innovative devices. Hence, we may pay attention to the following quote: ”Nevertheless, various optimizing schemes of the key properties in these fenestration types have to be chosen and carried out, e.g. the solar radiation utilized in a solar cell and converted into electricity cannot be exploited as daylight in the buildings. One might also envision incorporating solar cells or photovoltaics with electrochromic materials in completely new fenestration products, where the photovoltaic and electrochromic material or materials cover the whole glazing area. However, normal windows still need a transparent (in some cases translucent) state, and when in this state such windows cannot produce electricity from the visible part of the solar spectrum as the visible light is transmitted through the window.” [52].

The National Renewable Energy Laboratory (NREL) of Golden (USA) has built self-powered photovoltaic electrochromic devices up to 25 cm^2 [60]. For these self-powered PV electrochromic devices, ”…the main concerns for future large-area applications are the possible loss of the energy generated by the PV device for larger dimensions, a small range of optical modulation and rather low transmittances in the clear state.” [60].

Thus, integrating PV with electrochromics or other smart window (colour switching) technologies in a way so that the PV-electrochromic elements will provide shading when there is need for it is yet another research path [63-67]. Thereby, electricity will be produced while the windows block the solar radiation. Moreover, in the building industry electrochromic windows with no external electrical wiring may at the moment be most desirable.

3.16. SELF-CLEANING SURFACES

Self-cleaning window glass panes already exist commercially, which are supposed to decrease the need for manual cleaning substantially. This technology may also be used for the glass surfaces of PV and BIPV systems. Most of these self-cleaning glass panes function by applying a photocatalytic coating like e.g. titanium dioxide (TiO_2) on the outer glass surface, where the incident ultraviolet (UV) solar radiation reacts with this coating to break down organic dirt. Thereafter, rain water spreads evenly over the hydrophilic surface and runs off in a ”sheet” taking loosened dirt with it, thus drying quickly without leaving stains or streaks. A state-of-the-art review on commercially available self-cleaning glazing products along with a study on future research pathways are presented by Midtdal and Jelle [68].

According to their operational state when purchased, the commercial self-cleaning products may be divided into factory- and user-finished products [68]. Factory-finished products cover all factory produced glazing products (e.g. windows) where a self-cleaning surface is already operational when purchased. User-finished (user-do-it-yourself) products involve liquid products, either in form of a spray or a roll-on applicator, which can be applied by the user to existing glass surfaces to obtain a self-cleaning coating or film on top of the regular glass pane or any other material.

Various strategies are applied and pursued for achieving a self-cleaning effect, where these may be categorized into the following different surface characteristics:

(a) Photocatalytic hydrophilic surface.
(b) Superhydrophobic or ultrahydrophobic surface.
(c) Microstructured or nanostructured surface.

Commercial factory-finished self-cleaning products are most often based on photocatalytic hydrophilic coatings or surfaces, whereas user-finished self-cleaning products are normally based on the creation of hydrophobic coatings on the desired surfaces.

In the following we will learn that there exists an important correlation between superhydrophobicity and a structured coarseness of a surface, whereupon the term icephobicity will also be discussed. As a general rule of thumb, the coarseness dimensions of the structured self-cleaning surface should be smaller than the dirt particles to be removed by the self-cleaning effect.

3.17. SUPERHYDROPHOBIC AND ICEPHOBIC SURFACES

Superhydrophobicity, icephobicity and similar aspects on how to avoid snow and ice formation on the solar cell surfaces will be among the important issues to address. In Fig.18 [69,70] this challenge is shown, as depending on the climate conditions, snow and ice may stick to smooth glass surfaces for large inclination angles and even for vertical surfaces.

Fig.18. Snow/ice slab firmly sticking to the glass surface of an insulated window pane even at an inclination angle of 90° during a laboratory experiment (left). Snow covering a solar cell panel at an inclination angle of 70° (right) [69,70].

Hydrophobicity is an often used measure of the repellent nature of a surface, and then especially to repel water. A completely hydrophobic surface has a water contact angle of 180°, whereas a completely hydrophilic surface has a water contact angle of 0°. A surface is considered as hydrophilic for water contact angles below 90°, hydrophobic above 90°, superhydrophilic below 5° (within 0.5 s or less) and superhydrophobic above 150° [71-74].

The hydrophobicity of a surface will be dependent upon (i) the micro- and nanoscale coarseness of the surface, and (ii) the surface energy of the surface, where the former one may be considered as a mechanical property and the latter one as a chemical property, respectively. In general, a micro- or nanoscale coarse surface and a low surface energy will give a hydrophobic surface. A low surface energy can be achieved by use of reactive molecules mainly classified into four categories, i.e. fluorinated molecules, alkyl molecules, non-fluorinated polymers and silicon/silane compounds [73,75].

A surface's coarseness on a micro- and nanoscale has a direct influence on its repellent and hydrophobic properties. The wetting states of a liquid drop placed on a surface are illustrated in Fig.19 depicting a smooth surface (where contact angle measure is shown), the Wenzel state, the Cassie-Baxter state and a combined state [76], where the Cassie-Baxter state represents the superhydrophobic state where liquid drops are repelled as spheres from the surface (large contact angle). In the Wenzel state the liquid (water) drops are impaled by the nanorods (or similar structure) on the surface, while in the Cassie-Baxter state the liquid drops are resting on top of the nanorods with trapped air pockets beneath between the nanorods.

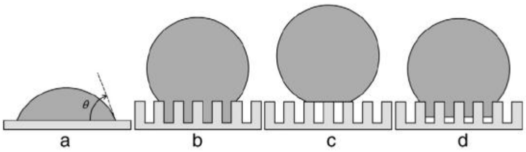

Fig.19. Wetting states of a liquid drop to a surface: (a) drop on a smooth surface (contact angle measure is illustrated), (b) Wenzel state, (c) Cassie-Baxter state, and (d) combined state [76].

In Fig.20 there is given an overview of the timeline of major advances in the area of liquid repellency, including advances in theory, polymer and surface chemistry, development of superhydrophobic surfaces (SHS), slippery liquid-infused porous surfaces (SLIPS), polydimethylsiloxane (PDMS) and polytetrafluoroethylene (PTFE) [77].

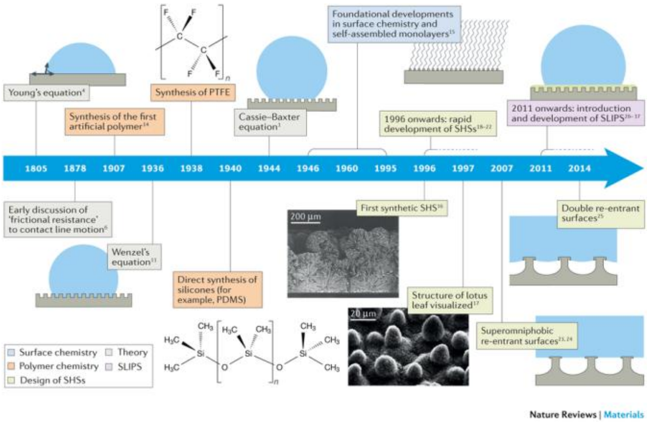

Fig.20. Timeline of major advances in the area of liquid repellency (enlarge digitally to see details) [77].

Examples of natural water-repellent leaf surfaces and artificially fabricated superhydrophobic surfaces are given in Fig.21 [78,79].

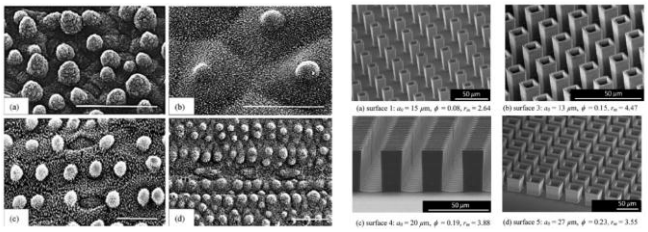

(a) surface 1: $a_0 = 15\ \mu m$, $\phi = 0.08$, $r_w = 2.64$
(b) surface 3: $a_0 = 13\ \mu m$, $\phi = 0.15$, $r_w = 4.47$
(c) surface 4: $a_0 = 20\ \mu m$, $\phi = 0.19$, $r_w = 3.88$
(d) surface 5: $a_0 = 27\ \mu m$, $\phi = 0.23$, $r_w = 3.55$

Fig.21. Micromorphologies for water-repellent leaf surfaces of (a) Nelumbo nucifera and (b) Lupinuspolyphyllos (scale bars = 50 μm), and (c) Gladioluswatsonioides and (d) Sinarundinaria nitida (scale bars = 20 μm) (left four photos) [78]. Images of four artificially fabricated hollow hybrid superhydrophobic surfaces (scale bars = 50 μm) (right four photos) [79].

Several of the same principles may be applied for anti-icing investigations as for self-cleaning aspects, in particular superhydrophobicity and structured surface coarseness effects, hence the term icephobicity has been introduced and is now in common usage. Anti-icing coating design cases with various roughness scales, including microscale roughness, nanoscale roughness and hierarchical roughness (combination of both micro- and nanoscale) are illustrated in Fig.22 [80].

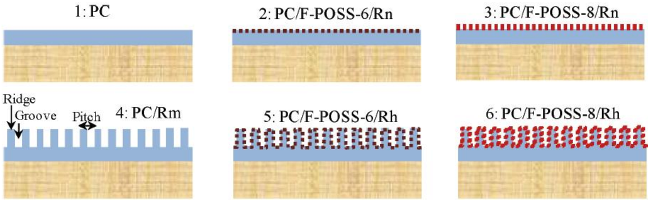

Fig.22. Anti-icing coating design cases with roughnesses Rn nanoscale, Rm microscale, and Rh hierarchical [80].

In Fig.23 there are shown micrographs of various surface structures for icephobicity, depicting nanocones, nanopits, micropillars and micropillars with embedded nanotextures [81]. Furthermore, Fig.23 also shows the effects of a nano-fluorocarbon coating on icing processes, where the water droplets on the coated surface have a much smaller contact area to the superhydrophobic surface, i.e. water spheres due to the large contact angle caused by the superhydrophobicity, resulting in a much longer starting time for icing and also a much longer total time needed to complete the whole icing process for the superhydrophobic surface than for the non-coated plain surface [82].

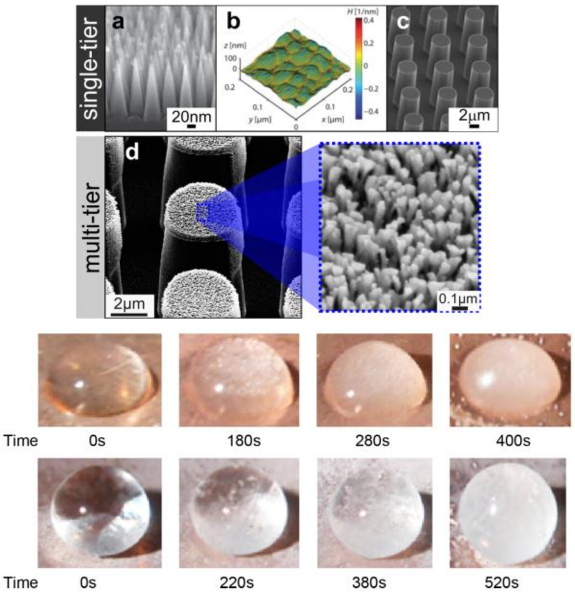

Fig.23. (Top) Micrographs showing relevant length scales and structures utilized in single-tier and multi-tier structures for icephobicity: (a) etched Si nanocones, (b) etched SiO_2 nanopits, (c) etched SiO_2 micropillars, and (d) etched Si micropillars/nanotextures with the nanotexture depicted in the inset image [81]. (Bottom) Icing process of a water droplet on a plain copper surface (top) and a nano-fluorocarbon coated surface (bottom) [82].

The task of preventing snow and ice formation involves other crucial aspects than merely removal of dirt and water from these surfaces. Freezing of water below 0°C represents a huge obstacle or challenge in this respect, which in some cases is further complicated by in general possible moisture condensation from surrounding air and subsequent freezing on the surfaces. Although many promising results have been achieved, e.g. for prolonged freezing delays on superhydrophobic surfaces, there is still much research to be carried out before practical and efficient snow and ice avoiding/repelling surfaces for a full range of outdoor weather exposure conditions have been accomplished.

An interesting research pathway may be to investigate if it is possible to make some sort of force field solution. That is, to envision a force field which could repel all snow crystals already before they are impacting onto the solar cell surfaces, in addition to prevent any ice formation on the exterior surfaces (e.g. rain which freezes, and condensation and freezing processes from moisture in the ambient air). Hence, one has to ask what kind of force field this could be, which in addition is (ideally) not using extra energy. An electric or magnetic force field, or a combination of these, either static or dynamic, may be investigated. Or could something entirely different be envisioned? In order to be able to repel the snow crystals one may explore if the dipolarity in water molecules may be taken advantage of and utilized, even in solid state as snow and ice and not as liquid water, or the various transition states (gas, liquid and solid state) at the solar cell surfaces.

Natural, biological superhydrophobic surfaces like e.g. plant leaves and insect wings when damaged may regenerate their surfaces by biological growth processes and are therefore able to maintain their superhydrophobicity over their whole lifetime. Thus, one may ask if it could be possible to make artificial superhydrophobic surfaces which would continuously regenerate their surface patterns and thereby retain their superhydrophobic properties, i.e. self-healing, self-repairing or self-regenerating superhydrophobic surfaces.

3.18. FINAL REMARKS

As new building materials and components are being developed, including BIPV materials, it is of major importance to investigate the durability of these materials, e.g. by carrying out accelerated climate ageing in the laboratory [83]. Furthermore, conducting a robustness assessment of these materials and components may also be found to be beneficial [84]. Finally, it seems appropriate to end this with the following vision from Richard Lunt at Michigan State University: ”*Ultimately, we want to make solar harvesting surfaces that you don’t even know are there.*” [12].

IV. CONCLUSIONS

Various research pathways and opportunities for building integrated photovoltaics (BIPV) from a materials science viewpoint are explored. Continued research and development within both PV and BIPV materials and technologies will improve the BIPV solutions in the coming years, e.g. with respect to solar cell efficiency, environmental aspects, robustness, long-term durability versus climate exposure, production costs and miscellaneous building integration aspects. Easily applicable and flexible solutions like e.g. paint applications of PV cells and bendable solar cells are among the future visions for BIPV.

ACKNOWLEDGEMENTS

This work has been supported by the Research Council of Norway and several partners through the research projects ”Building Integrated Photovoltaics for Norway” (BIPV Norway) and ”The Research Centre on Zero Emission Buildings” (ZEB).

REFERENCES

[1] Solar Thermal Magazine, October 23, 2010, <http://www.solarthermalmagazine.com/2010/10/23/the-curved-solar-power-rooftop-tile-homeowners-now-have-better-looking-options/>, 2010 (accessed November 8, 2011).

[2] Applied Solar, <http://www.appliedsolar.com/roofingsystems/roofingtiles.php>, 2010 (accessed December 9, 2010).

[3] SRS Energy, <http://www.srsenergy.com/maint/files/SPT16%20Technical%20Specifications%20090310.pdf>, 2010 (accessed October 5, 2010).

[4] Solar Century, <http://www.solarcentury.co.uk/installers-and-roofers/products/solar-tiles/c21e-solar-roof-tiles/>, 2011 (accessed December 14, 2011).

[5] B.P. Jelle, C. Breivik and H.D. Røkenes, *Solar Energy Materials and Solar Cells*, **100**, 69-96, 2012.

[6] B.P. Jelle and C. Breivik, *Energy Procedia*, **20**, 68-77, 2012.

[7] B.P. Jelle and C. Breivik, *Energy Procedia*, **20**, 78-87, 2012.

[8] B.P. Jelle, *Energies*, **9**, 1-30, Article no. 21, 2016.

[9] NREL, Best research-cell efficiencies, Rev. 04-20-2016, <http://www.nrel.gov/ncpv/images/efficiency_chart.jpg>, 2016 (accessed April 20, 2016).

[10] O.E. Semonin, J.M. Luther, S. Choi, H.-Y. Chen, J. Gao, A.J. Nozik and M.C. Beard, *Science*, **334**, 1530-1533, 2011.

[11] Y.-C. Huang, C.-C. Chan, S.-J. Wang and S.-K. Lee, *Energy Procedia*, **61,** 1874-1878, 2014.

[12] A. Mourant, ”BIPV: Better form, improved function”, *Renewable Energy Focus*, September/October 2014.

[13] The German Energy Society (DGS), ”Planning and installing photovoltaic systems - A guide for installers, Architects and Engineers”, Earthscan, 2008.

[14] M.L. Parisi, S. Maranghi and R. Basosi, *Renewable and Sustainable Energy Reviews*, **39**, 124-138, 2014.

[15] V. Sugathan, E. John and K. Sudhakar, *Renewable and Sustainable Energy Reviews*, **52**, 54-64, 2015.

[16] R. Amadelli, R. Argazzi, C.A. Bignozzi and F. Scandola, *Journal of the American Chemical Society*, **112**, 7099-7103, 1990.

[17] S. Buecheler, A. Chirilă, J. Perrenoud, L. Kranz, C. Gretener, P. Blösch, F. Pianezzi, S. Seyrling and A.N. Tiwari, ”Flexible and lightweight solar modules for new concepts in building integrated photovoltaics”, in: *Proceedings of the CISBAT*, Lausanne, Switzerland, September 14-16, 2011.

[18] B. Stuart, ”CIGS cells to ”dominate” future BIPV market”, PV Magazine, <http://www.pv-magazine.com/news/details/beitrag/cigs-cells-to-dominate-future-bipv-market_100001483/>, November 1, 2010 (accessed February 9, 2012).

[19] A. Gerthoffer, F. Roux, F. Emieux, P. Faucherand, H. Fournier, L. Grenet and S. Perraud, *Thin Solid Films*, **592: Part A**, 99-104, 2015.

[20] W.A. Badawy, *Journal of Advanced Research*, **6**, 123-132, 2015.

[21] Y. Zhang, S. Sun, R. Kang, J. Zhang, N. Zhang, W. Yan, W. Xie, J. Ding, J. Bao and C. Gao, *Energy Conversion and Management*, **95**, 187-192, 2015.

[22] H. Baig, N. Sellami and T.K. Mallick, *Solar Energy Materials and Solar Cells*, **134**, 29-44, 2015.

[23] A.W. Smith and A. Rohatgi, *Solar Energy Materials and Solar Cells*, **29**, 37-49, 1993.

[24] J. Kang, C. Cho and J.-Y. Lee, *Organic Electronics*, **26**, 61-65, 2015.

[25] D. Prasad and M. Snow, ”Designing with solar power - A source book for building integrated photovoltaics (BiPV)”, The Images Publishing Group Pty Ltd and Earthscan, London, 2005.

[26] SolarPower Restoration Systems Inc., ”Solar seal PV concrete system”, <http://www.solarpower-restoration.com/solar-seal-pv-concrete-system.html>, (not dated) 2011 (accessed December 9, 2011).

[27] DysCrete, ”DysCrete: Power from concrete”, <http://becquerelinstitute.org/dyscrete-power-from-concrete/>, 2015 (accessed July 30, 2015).

[28] DysCrete, ”DysCrete - Experimental energy production systems”, <http://www.baukunsterfinden.org/en/research/projects/dyscrete-energy-production-systems/>, 2015 (accessed July 30, 2015).

[29] A. Javier and E.E. Foos, *IEEE Transactions on Nanotechnology*, **8**, 569-573, 2009.

[30] J.-H. Lee, H.-S. Shin, Y.-J. Noh, S.-I. Na and H.-K. Kim, *Solar Energy Materials and Solar Cells*, **114**, 15-23, 2013.

[31] S.-W. Heo, J.-Y. Lee, H.-J. Song, J.-R. Ku and D.-K. Moon, *Solar Energy Materials and Solar Cells*, **95**, 3041-3046, 2011.

[32] S.-B. Kang, Y.-J. Noh, S.-I. Na and H.-K. Kim, *Solar Energy Materials and Solar Cells*, **122**, 152-157, 2014.

[33] D.-Y. Cho, K. Eun, S.-H. Choa and H.-K. Kim, *Carbon*, **66**, 530-538, 2014.

[34] Y.-J. Kang, D.-G. Kim, J.-K. Kim, W.-Y. Jin and J.-W. Kang, *Organic Electronics*, **15**, 2173-2177, 2014.

[35] S.-S. Kim, S.-I. Na, S.-J. Kang and D.-Y. Kim, *Solar Energy Materials and Solar Cells*, **94**, 171-175, 2010.

[36] J.-W. Lim, D.-Y. Cho, Jihoon-Kim, S.-I. Na and H.-K. Kim, *Solar Energy Materials and Solar Cells*, **107**, 348-354, 2012.

[37] Q. Liu, T. Ohki, D. Liu, H. Sugawara, R. Ishikawa, K. Ueno and H. Shirai, *Nano Energy*, **11**, 260-266, 2015.

[38] N. Chehata, A. Ltaief, E. Beyou, B. Ilahi, B. Salem, T. Baron, P. Gentile, H. Maaref and A. Bouazizi, *Journal of Luminescence*, **168**, 315-324, 2015.

[39] Z. Ge, L. Xu, R. Zhang, Z. Xue, H. Wang, J. Xu, Y. Yu, W. Su, Z. Ma and K. Chen, *Applied Surface Science*, **334**, 15-18, 2015.

[40] F. Cao, H. Wang, Z. Xia, X. Dai, S. Cong, C. Dong, B. Sun, Y. Lou, Y. Sun, J. Zhao and G. Zou, *Materials Chemistry and Physics*, **149-150**, 124-128, 2015.

[41] I. Mihalache, A. Radoi, M. Mihaila, C. Munteanu, A. Marin, M. Danila, M. Kusko and C. Kusko, *Electrochimica Acta*, **153**, 306-315, 2015.

[42] P. Yu, S. Qu, C. Jia, K. Liu and F. Tan, *Materials Letters*, **157**, 235-238, 2015.

[43] T. Kim, Y. Gao, H. Hu, B. Yan, Z. Ning, L.K. Jagadamma, K. Zhao, A.R. Kirmani, J. Eid, M.M. Adachi, E.H. Sargent, P.M. Beaujuge and A. Amassian, *Nano Energy*, **17**, 196-205, 2015.

[44] X. Ren, X. Li and W.C.H. Choy, *Nano Energy*, **17**, 187-195, 2015.

[45] X.-P. Cui, K.-J. Jiang, J.-H. Huang, Q.-Q. Zhang, M.-J. Su, L.-M. Yang, Y.-L. Song and X.-Q. Zhou, *Synthetic Metals*, **209**, 247-250, 2015.

[46] W. Yan, Y. Li, Y. Li, S. Ye, Z. Liu, S. Wang, Z. Bian and C. Huang, *Nano Energy*, **16**, 428-437, 2015.

[47] K. Wang, C. Liu, P. Du, L. Chen, J. Zhu, A. Karim and X. Gong, *Organic Electronics*, **21**, 19-26, 2015.

[48] T. Segal-Peretz, O. Sorias, M. Moshonov, I. Deckman, M. Orenstein and G.L. Frey, *Organic Electronics*, **23**, 144-150, 2015.

[49] W. Jaimes, G. Alvarado-Tenorio, C. Martinez-Alonso, A. Quevedo-López, H. Hu and M.E. Nicho, *Materials Science in Semiconductor Processing*, **37**, 259-265, 2015.

[50] U. Mehmood, I.A. Hussein, K. Harrabi, M.B. Mekki, S. Ahmed and N. Tabet, *Solar Energy Materials and Solar Cells*, **140**, 174-179, 2015.

[51] U. Dasgupta, A. Bera and A.J. Pal, *Solar Energy Materials and Solar Cells*, **143**, 319-325, 2015.

[52] B.P. Jelle, A. Hynd, A. Gustavsen, D. Arasteh, H. Goudey and R. Hart, *Solar Energy Materials and Solar Cells*, **96**, 1-28, 2012.

[53] B.P. Jelle and G. Hagen, *Journal of The Electrochemical Society*, **140**, 3560-3564, 1993.

[54] C.G. Granqvist, "Handbook of inorganic electrochromic materials", Elsevier, Amsterdam, 1995.

[55] P.M.S. Monk, R.J. Mortimer and D.R. Rosseinsky, "Electrochromism: Fundamentals and applications", VCH, 1995.

[56] B.P. Jelle, G. Hagen and Ø. Birketveit, *Journal of Applied Electrochemistry*, **28**, 483-489, 1998.

[57] B.P. Jelle and G. Hagen, *Journal of Applied Electrochemistry*, **28**, 1061-1065, 1998.

[58] B.P. Jelle and G. Hagen, *Solar Energy Materials and Solar Cells*, **58**, 277-286, 1999.

[59] B.P. Jelle, A. Gustavsen, T.-N. Nilsen and T. Jacobsen, *Solar Energy Materials and Solar Cells*, **91**, 342-354, 2007.

[60] R. Baetens, B.P. Jelle and A. Gustavsen, *Solar Energy Materials and Solar Cells*, **94**, 87-105, 2010.

[61] B.P. Jelle, *Solar Energy Materials and Solar Cells*, **116**, 291-323, 2013.

[62] R.J. Mortimer, D.R. Rosseinsky and P.M.S. Monk (Eds.), "Electrochromic materials and devices", Wiley-VCH, 2015.

[63] J.N. Bullock, C. Bechinger, D.K. Benson and H.M. Branz, *Journal of Non-Crystalline Solids*, **198-200**, 1163-1167, 1996.

[64] W. Gao, S.H. Lee, J. Bullock, Y. Xu, D.K. Benson, S. Morrison and H.M. Branz, *Solar Energy Materials and Solar Cells*, **59**, 243-254, 1999.

[65] S.K. Deb, S.-H. Lee, C. Edwin Tracy, J. Roland Pitts, B.A. Gregg and H.M. Branz, *Electrochimica Acta*, **46**, 2125-2130, 2001.

[66] C.M. Lampert, *Solar Energy Materials and Solar Cells*, **76**, 489-499, 2003.

[67] K.-S. Ahn, S.J. Yoo, M.-S. Kang, J.-W. Lee and Y.-E. Sung, *Journal of Power Sources*, **168**, 533-536, 2007.

[68] K. Midtdal and B.P. Jelle, *Solar Energy Materials and Solar Cells*, **109**, 126-141, 2013.

[69] B.P. Jelle, *Energy and Buildings*, **67**, 334-351, 2013.

[70] B.P. Jelle, T. Gao, S.A. Mofid, T. Kolås, P.M. Stenstad and S. Ng, *Procedia Engineering*, **145**, 699-706, 2016.

[71] N.J. Shirtcliffe, G. McHale, S. Atherton and M.I. Newton, *Advances in Colloid and Interface Science*, **161**, 124-138, 2010.

[72] V. Hejazi, K. Sobolev and M. Nosonovsky, *Scientific Reports*, **3:2194**, 1-6, 2013.

[73] L. Yao and J. He, *Progress in Material Science*, **61**, 94-143, 2014.

[74] P. Zhang and F.Y. Lv, *Energy*, **82**, 1068-1087, 2015.

[75] C.-H. Xue, S.-T. Jia, J. Zhang and J.-Z. Ma, *Science and Technology of Advanced Materials*, **11**, 1-15, Article no. 033002, 2010.

[76] C. Antonini, M. Innocenti, T. Horn, M. Marengo and A. Amirfazli, *Cold Regions Science and Technology*, **67**, 58-67, 2011.

[77] M.J. Kreder, J. Alvarenga, P. Kim and J. Aizenberg, *Nature Reviews Materials*, **1**, 1-15, Article no. 15003, 2016.

[78] S.-H. Hsu, K. Woan and W. Sigmund, *Materials Science and Engineering R*, **72**, 189-201, 2011.

[79] S. Dash, M.T. Alt and S.V. Garimella, *Langmuir*, **28**, 9606-9615, 2012.

[80] J. Xiao and S. Chaudhuri, *Langmuir*, **28**, 4434-4446, 2012.

[81] T.M. Schutzius, S. Jung, T. Maitra, P. Eberle, C. Antonini, C. Stamatopoulos and D. Poulikakos, *Langmuir*, **31**, 4807-4821, 2015.

[82] H. Wang, G. He and Q. Tian, *Applied Surface Science*, **258**, 7219-7224, 2012.

[83] B.P. Jelle, *Journal of Materials Science*, **47**, 6475-6496, 2012.

[84] B.P. Jelle, E. Sveipe, E. Wegger, A. Gustavsen, S. Grynning, J.V. Thue, B. Time and K.R. Lisø, *Journal of Building Physics*, **37**, 213-245, 2014.

Journal of Energy Challenges
and Mechanics
http://www.nscj.co.uk/JECM/

ISSN 2056-9386
Volume 3 (2016) issue 2, article 7

Multisided approach for photovoltaics regulated outputs: computer-based simulations

多片面光伏稳压输出：基于计算机的模拟

Janvier Kamanzi[1*], Mohamed Kahn[2]

[1,2]*Centre for Distributed Power and Electronic Systems, Cape Peninsula University of Technology, Cape Town 7535, SA*

kajanois@gmail.com

Accepted for publication on 2 September 2015

Abstract – **The world is experiencing unprecedented moments of energy crisis along with its associated aftermath. However, solutions sought in renewable energy sources have not been optimally exploited, and this the case of solar-based sources that use Photovoltaics (PVs) as an energy conversion platform. Through computer-based simulations, this article shows, in accurate figures, the extent of the effects of using the classic single fixed-tilt solar panels; and investigated multisided PV systems in order to provide an evenly distributed power as to address the issue of Gaussian-shaped outputs characteristic of fixed-tilt panels. Various multisided systems were therefore studied; and a double-sided PV system, with a 60^0 junction angle, was found to be the best in terms of output power level and smoothness. The study also suggested the adoption of cylindrical-shaped systems for direct and continuous output though with a bit lower level than the output of a double-sided system.**

Keywords – **Distributed systems, Multisided systems, Photovoltaics, PV topologies, Renewable energy.**

I. INTRODUCTION

The whole world is living an unprecedented time of energy crisis and its associated aftermath on the society and environment [1] and solutions have been sought in alternative primary energy sources. The fossil fuels dominating the pool of primary energy supply are faced with depletion due to exponential increase in energy demand in one hand and critics big role in the alarming global warming and climate change on the other hand.

The global demand in energy is deemed to double within the next two decades [2] involving an imminent increase use of green and renewable energy [3]. In this regard, Global Market Outlook [4] indicated that solar-based power would increase from 138.8 GW 2013 figures to 1700 GW within two and half decades (2030), whereas a further remarkable increase up to 4670 GW would be expected by 2050. In parallel, the author [4] highlighted there would be an increase in the implantation of wind supplied power generators with a bit low impact observable as compared to solar powered generators.

With the sun providing about 2 MWh/m^2 to the earth [5], which is by far higher than any other source of energy [6] and being by excellence IEA compliant, solar energy has proven its worth in terms alternative power generation platform for all the time.

In the context of South Africa, the Department of Energy (DoE) along with public electricity utility (ESKOM) plus private companies have made significant progress toward a full and optimized use of available energy sources and integration of the latter in the national grid. Policies involving Independent power producers (IPP) were adopted with regard to integrating distributed energy sources in electric power systems [7], [8]. To make this a success, smart techniques for grid automation and management of power distributed systems were given a priority research wise [9].

However, with focus on solar energy, low efficiency and inconsistent power outputs of PV cells remain an intricate concern to address. This has been a major and longtime handicap to the adoption of the PV based grid as part of the countries' national grids. A lot of studies and initiatives from various perspectives have been conducted with encouraging results; of which some have been spotlighted.

Low efficiency improvement has been targeted by much research in an attempt to make PV technology more viable and an increase of 5% could be gained by using Magnesium-doped quantum dot sensitized solar cells [10]. Thin film is another technology which was brought forth to increase the PV efficiency yielding an increase of about 4% [11].

While the efficient is inherent to the scarcity of material used to manufacture PV cells, another factor lowering the cells output is external. Solar cells performance reliance to weather conditions results in a non-uniform power distribution throughout the day and the year and no much can be done versus natural conditions.

Nevertheless, the way PV arrays have been used do not take advantage of the available light for a maximum electrical energy conversion. PV arrays as traditionally laid on the roof of buildings at a certain angle can receive the maximum sun irradiation at noon over a whole day (Figure 1). Moreover, the sun shuttling between the two tropics yearly exposes the shortcoming of fixed tilt angle PV approach. Figure 2 shows combined effect of sun's daily and yearly apparent movements on the output power dynamics. The PV output power was simulated with respect to the irradiance set at 1 kW/m^2 for convenience purposes; the sun moving from one tropic to another i.e. between -23.45^0 and 23.45^0. The sun's movement double effect is also shown on a 3D plot in Figure 3. The PV output power shown in Figure 2 reflects a moderated case with a minimum of 92 % of the expected output for an observer located in the equatorial region. With the tropic being the limits of observation, the best in terms of irradiance will occur when one tropic is experiencing the solstice whereas the opposite tropic is at the worse since having the longest night producing an output drop down to 72% of the nominal output.

The paper aims to address the issue of the Gaussian-shaped PV output as represented in Figure 1. By ideally considering that the sun rises at 6 am, the irradiance is null, the PV output grows up and becomes maximum at noon and falls back to zero at 6 pm, ideal sunset. Thus, between sunrise and sunset, the power follows a sine waveform between zero and pi radians. Mathematically, it can be expressed as per equation 1.

$$I = I_M \sin\theta, \quad 0 \le \theta \le \pi \tag{1}$$

where I is the irradiance, I_M, the maximum irradiance and θ, an angle describing the sun's apparent movement over a day.

Figure 3 shows in 3-D the double effect of the sun's motion and the study's expected outcome. During the day, the power is expected to be uniform while less may be done to circumvent the effect of the sun's shuttle between the two tropics on the PV output; the worst case still being observed at poles.

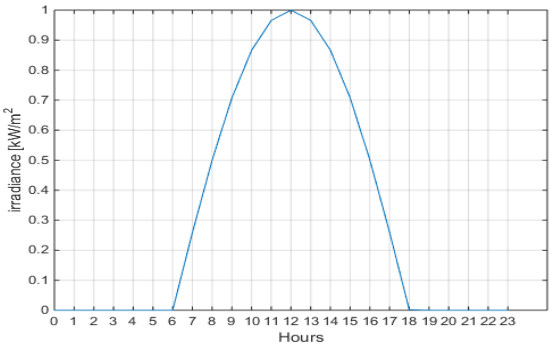

Fig.1, Power distribution for a single classic panel

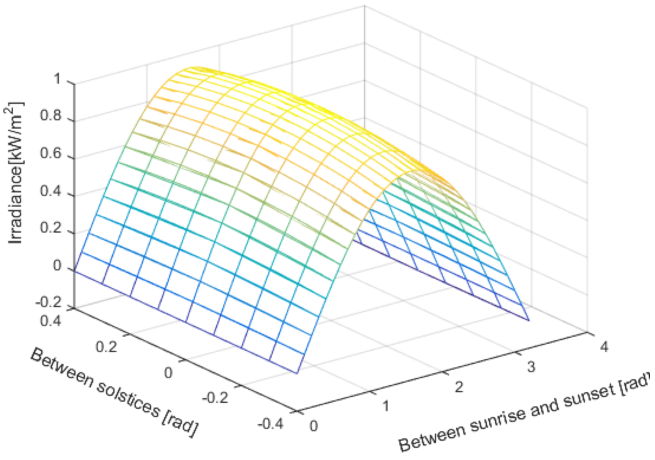

Fig.2, Simulation of moderated effects of double sun's apparent movement on the power

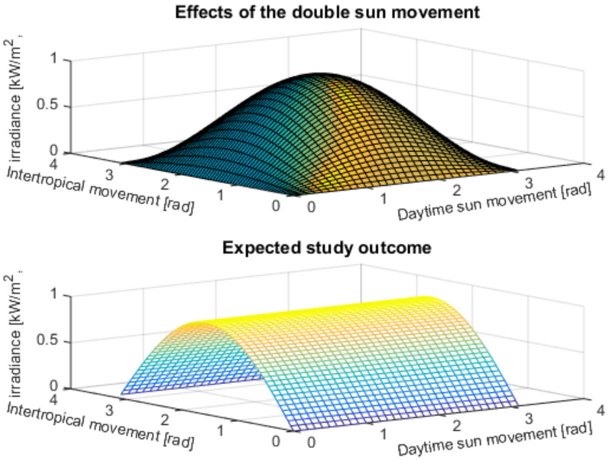

Fig.3, Simulation of the study expected outcome

II. MULTISIDED APPROACH

A multisided PV system approach is one of the possible solutions to improving PV output based on a possibility such a system can exhibit in terms of optimum exposure to the sun at any moment of the day time (Figure 4). The study therefore explores various type of PV arrays arrangements and was referred to a work which was conducted on PV topologies [12]. The systems' performance was assessed trough simulations conducted in Matlab, a scientific and engineering computing environment.

Assumptions were made for convenience and simplicity purposes with the aim to ease the understanding of the study and the interpretation of the results. The irradiance, the power per unity area produced by the sun, was assumed to be 1kW/m^2 and the sides of the PV system to be identical, have equal area and have a total area of 1m^2. Hence, simulated results on various graphs reflect dynamics in power and irradiance simultaneously following the sun's apparent movement. In the context of this study, a day or day time refers to the time interval to the night between the sunrise and sunset, a portion opposed to the night. The study started from a double-sided PV system, a direct upgrade of a classic single-sided.

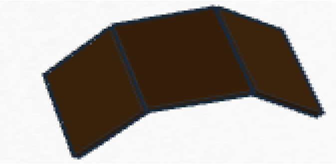

Fig.4, Picture of a tilted multisided PV system

2.1. DOUBLE-SIDED PV SYSTEM

A double-sided PV system was conceived in a way the structure allows significant and balanced exposure to the sun from sunrise to sunset. Therefore, the sides of the system were designed as to have the external angle facing the sun at noon. Systems with a 120^0, 90^0, 60^0, 45^0 and 30^0 junction angles respectively were studied and exhibited power performance according to Figures 5 through 9, including wide and obtuse angles to make ensure the study is comprehensive.

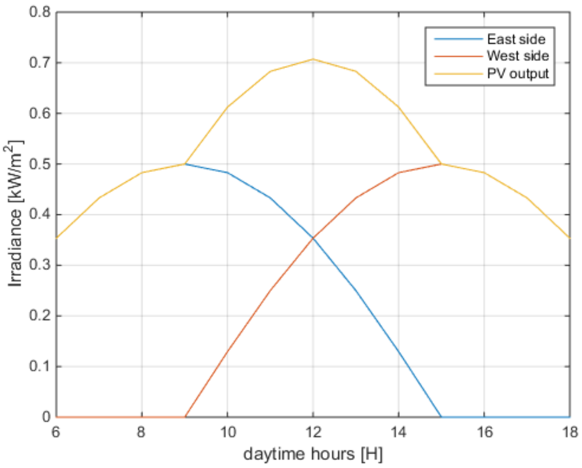

Fig.5, Power dynamics for a double-sided with 90^0 junction angle

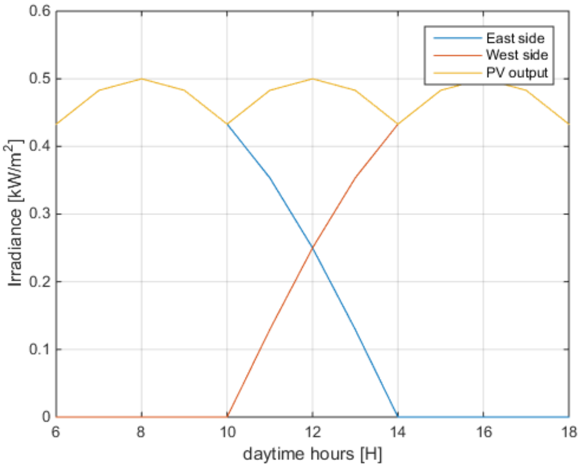

Fig.6, Power dynamics for a double-sided with 60^0 junction angle

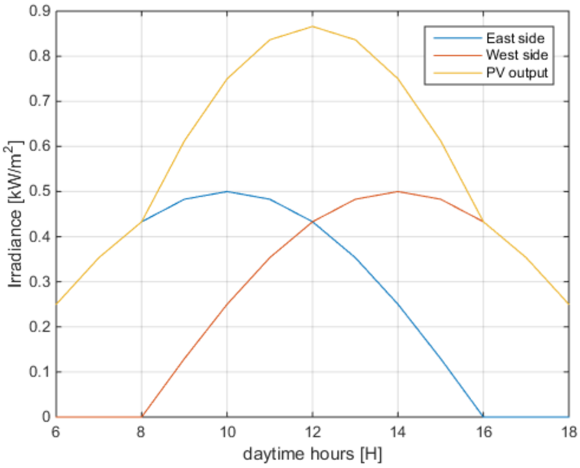

Fig.7, Power dynamics for a double-sided system with 120^0 junction angle

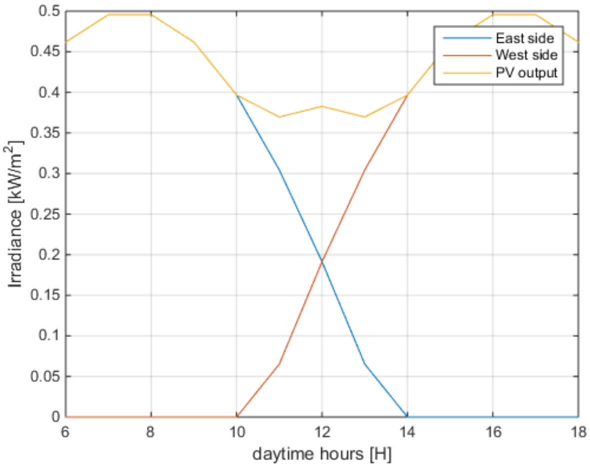

Fig .8, Power dynamics for a double-sided with 45^0 junction angle

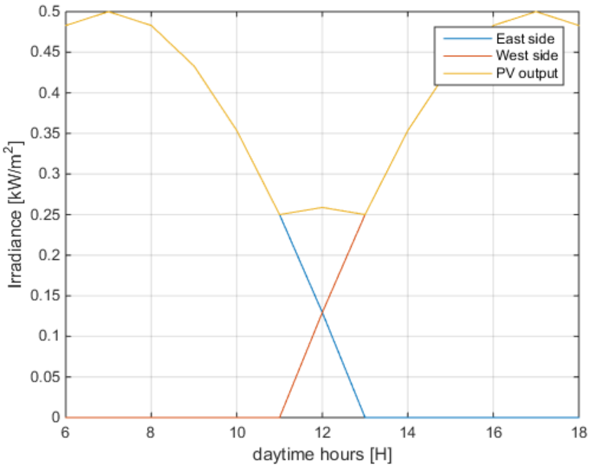

Fig.9, Power dynamics for a double-sided with 30^0 junction angle

For the double-sided PV systems, simulation results showed that systems with 60^0 junction angle (Figure 6) produce better power dynamics in terms of steadiness and uniformity of the output power over the whole day though with a bit lower average output 0.4715 kW against 0.5259 kW and 0.5644 kW for systems with 90^0 (Figure 5) and 120^0 (Figure 7) junction angles respectively and a bit higher than 0.4420 kW and 0.4049 kW for systems with 45^0 (Figure 8) and 30^0 (Figure 9) respectively. The PV systems with 90^0 and 120^0 angles manifest a remarkable power bump around noon whereas the remaining two exhibit a depression around the same period, which is not good for the load and therefore require extra regulation attention. Also the output power ripple for the 60^0 angled system is the lowest, 0.067 kW than the rest having ripples ranging between 0.1261 kW and 0.616 kW. Systems with further more sides were investigated in the perspective of improved power dynamics and low ripple rates.

2.2. THREE-SIDED PV SYSTEM

A three-sided PV system should be the first to consider matching three main parts a day can be divided into, the morning, the noon and the evening.

This PV system was thought of with one PV side exposed to the rising sun with a period of 6:00 to 10:00, another between 10:00 and 14:00 whereas the last has to effectively deal with energy harvesting between 14:00 and 18:00, the sunset time. PV sides have the same area and are joined at right angles.

Three sided systems with different angles were explored and their output power simulated in the process of seeking a system with a much better performance. Therefore, systems with wider angle than 90, thus a 120^0 angled system became part of the stud and power dynamics plotted in Figures 10 and 11 respectively.

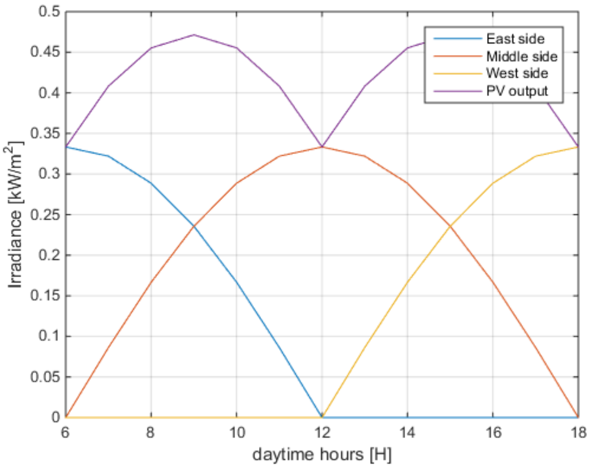

Fig.10, Power dynamics for a three-sided system with right angle junction

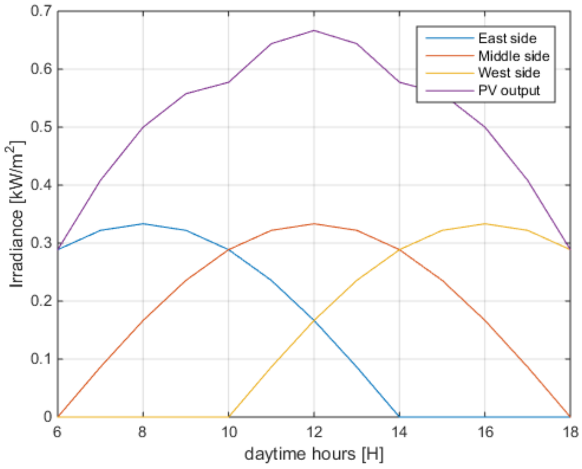

Fig.11, Power dynamics for a three-sided system with 120^0 junction angle

Simulation results obtained from the strategically chosen three-sided systems showed that systems with 90^0 junction angle exhibit more promising output power plot though with a bit lower average power, 0.4152 kW (Figure 10) than 120 angled systems, 0.5091 (Figure 11), and far away improved dynamics than systems separated with much wider angles. In this respect, systems with 90^0 have a significantly low ripple rate 29% as compared to 57% of the 120^0 angled systems. In this perspective, it is important to notice that the wider the angle, the more the system tends to behave like a classic single-sided PV panel and has an exacerbated amount of power around noon.

2.3. SYSTEMS WITH A LARGER NUMBER OF SIDES

Systems with a higher number of sided were investigated namely a four, five, six seven sided and output powers were plotted in Figures 12 through 16 respectively. These systems were assumed to have junction angle equivalent to the angle between the sides of a base of a corresponding half polygon, i.e. 135^0 for a four-sided, 144^0 for a five-sided, 150^0 for a six-sided, 154.5^0 for a seven-sided and 157.5^0 for an eight-sided.

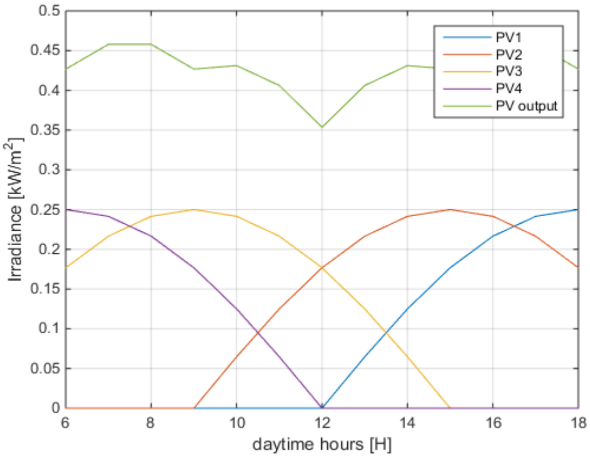

Fig.12, Power dynamics for a four-sided system with 45^0 junction angle

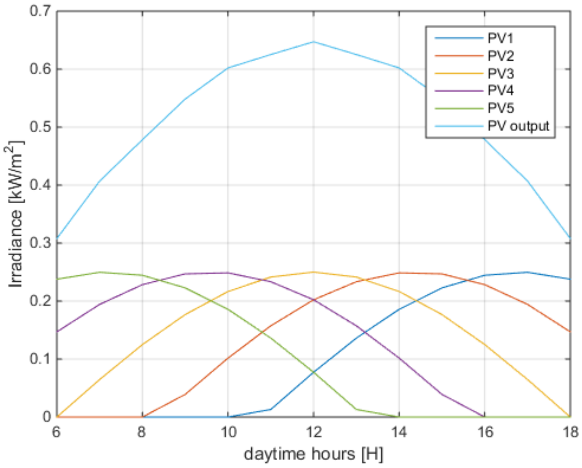

Fig.13, Power dynamics for a five-sided system

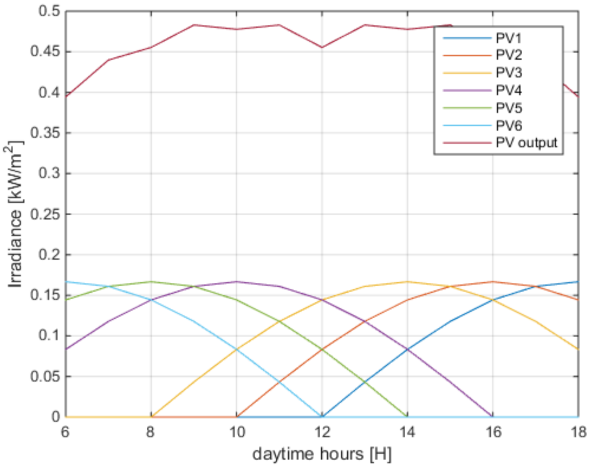

Fig.14, Power dynamics for a six-sided system

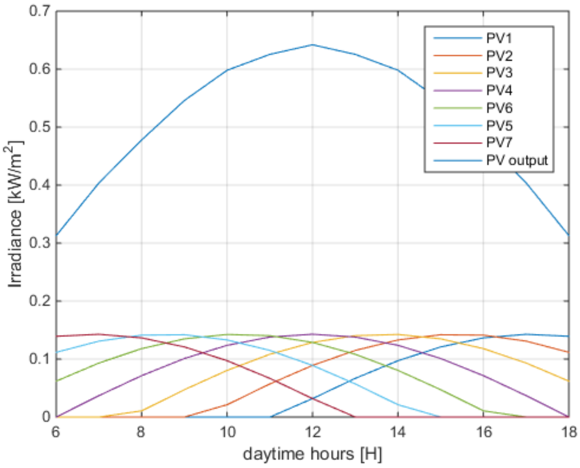

Fig. 15, Power dynamics for a seven-sided system

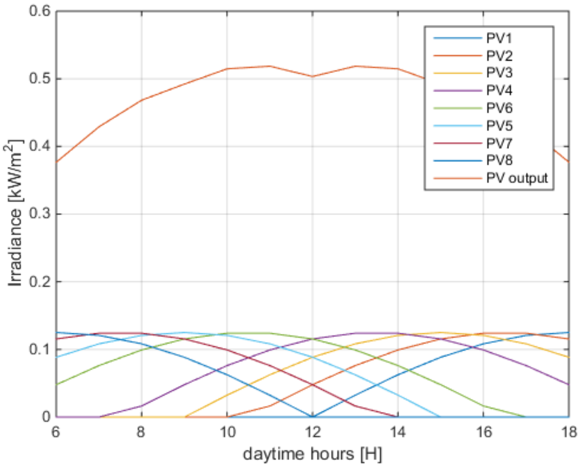

Fig. 16, Power dynamics for an eight-sided system

The general observation was that the six-sided had a much more even power distribution, 18% ripple ratio with an average power of 0.455 kW, followed by the four and eight-sided systems with 23% and 27% ripple ratios with an average power of 0.42 kW and 0.46 kW. The five and seven sided systems' power dynamics exhibit a huge bump around noon, due to the presence of a middle panel permanently exposed to the sun the whole day which is at its peak at noon.

III. SUMMARY OF RESULTS

The results for the studied multisided PV systems are summarized in Table 1 and presented in graphs for a broad view and easy comparison. Parameters hereby concerned are the maximum power, average power, the ripple and ripple ratio as per Figures 17 through 20. The average power and the ripple ratio are especially predetermining parameters when it comes to the output amplitude and smoothness and hold therefore the key factor for best system selection.

TABLE 1, RESULTS SUMMARY

System-angle	Max (kW)	Average	Ripple-	Ripple

(^{0})		(kW)	(kW)	(%)
Double (60)	0.500	0.472	0.067	50.0
Double (90)	0.707	0.526	0.354	13.4
Double (120)	0.866	0.564	0.433	71.0
Double (30)	0.500	0.405	0.250	50.0
Double (45)	0.496	0.442	0.126	25.4
Three (90)	0.744	0.636	0.411	29.3
Three(120)	0.667	0.629	0.089	56.7
Four (135)	0.458	0428	0.104	22.8
Five (144)	0.647	0.507	0.339	52.4
Six (150)	0.483	0.455	0.089	18.3
Seven (154.5)	0.642	0.505	0.329	51.2
Eight (157.5)	0.519	0.470	0.142	27.4

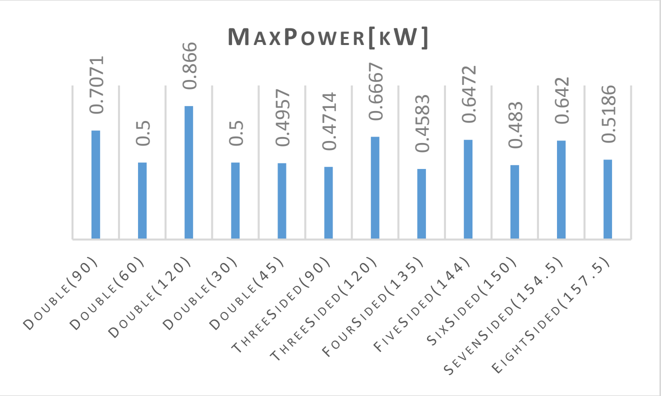

Fig.17, Maximum power comparison

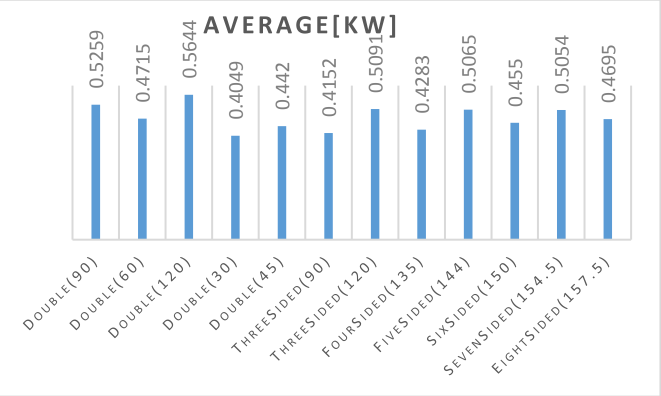

Fig.18, Average power comparison

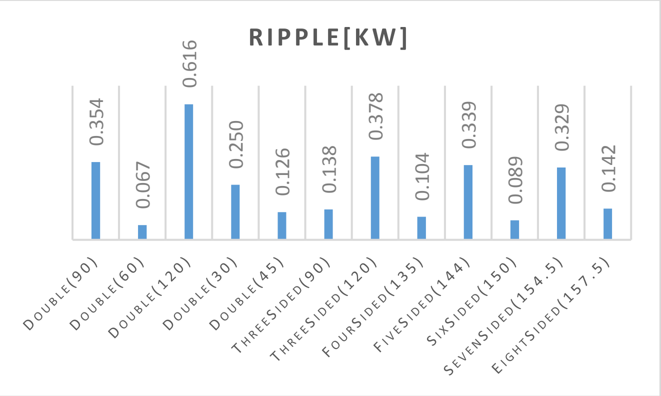

Fig.19, Ripple comparison

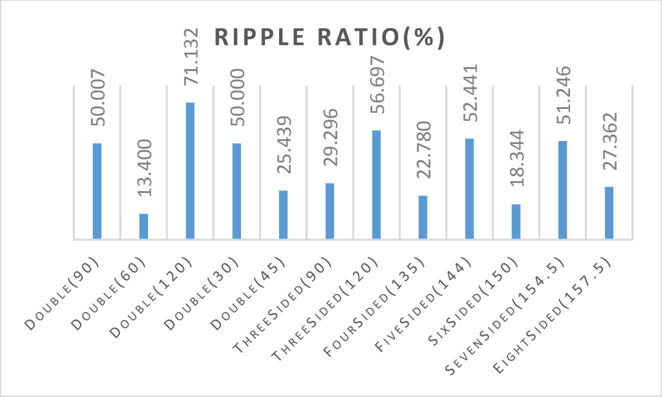

Fig.20, Ripple ratio comparison

IV. RESULTS DISCUSSION, ANALYSIS AND INTERPRETATION

Results for various PV systems investigated produce similarities regarding some parameters including the maximum and average output power. Double-sided and three-sided systems with junction angles greater than 90^0 have a maximum output greater than 0.7 kW and an average slightly greater than 0.5 kW whereas those with junction angle smaller than 90^0 supply a maximum of 0.5 kW and an average power ranging between 0.40 kW and 0.47 kW. In terms of ripple values, obtuse angles provide smaller ripple ratios and therefore a smoother output, and a 60^0 angled PV system was found to have the best power dynamics and lowest ripple and a reasonable average output power of about 0.5 kW.

For the rest, the four, the six and eight sided systems proved to have peak output powers ranging between 0.46 kW and 0.52 kW and an average lying between 0.43 kW and 0.46 kW. The mentioned systems offer an advantage of good power distribution, with the 60^0 angle systems having the lowest ripple ratio, 18.3%. Though the five and the seven sided can supply peak output powers greater than 0.64 kW and an average power a bit greater than 0.5 kW, their ripple ratio is a setback when it comes to the output smoothness. This is a general observation with regard to PV systems with an odd number of sides, same as with half cylinder shaped systems.

However, much regulated power outputs may be obtained using closed systems such as hollowed polygonal prism and cylindrical shaped systems (Figure 21). The power dynamics of such PV topologies were studied and the average output found to be 0.32 kW out of 1kW PV system nominal power, findings derived from a work explained in [12] [13]. In this respect a cylindrical shaped system may provide a perfectly regulated output power of about 0.32 kW for a total PV area of 1 m^2 and an irradiance of 1 kW/m^2.

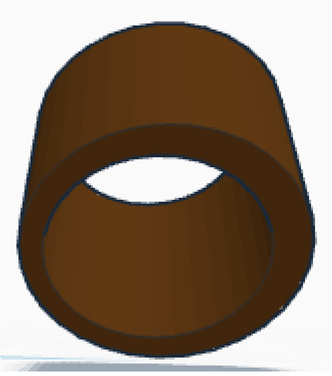

Fig.21, Cylindrical-shaped PV system

V. CONCLUSION

As a conclusion, from the pool of PV systems hereby studied, a double-sided system with a 60^0 junction angle shows much promise in terms of efficient utilization of sides, good output power average and smoothness. Come closed PV systems; hollowed cylindrical-shaped systems prove to be the best in applications where regulated power is imperative.

REFERENCES

[1] J. P. Holdren and C. Berkeley, “Population and the Energy Problem,” vol. 12, no. 3, 1991.
[2] G. W. Crabtree and N. S. Lewis, “Solar energy conversion,” *Physics Today*, March, pp. 37–42, 2007.
[3] J. Wright and E. E. Africa, “Electrical energy storage to make wind and solar PV resources disptatchable,” *Energize*, Vol.3, June, pp. 54–59, 2015.
[4] F. Photovoltaics, “GLOBAL MARKET,” 2014.
[5] P. R. E. Systems, “The sun shines , but not always …,” *Energize*, Vol.3, June, pp. 51–53, 2015.
[6] V. Mittal, “The study of solar absorption air-conditioning systems,” vol. 16, no. 4, pp. 59–66, 2005.
[7] A. Apostolov, “Integration of distributed energy resources in electric power systems,” *Energize*, Vol.3, June, 2015.
[8] C. Carter-brown, E. Ipp, R. Marais, K. Leask, D. Vrey, and R. Melesi, “Transmission network integration of renewable energy in South Africa,” *Energize*, Vol.3, June, 2015.
[9] P. Diamandis and Q. C. Systems, “Smart-grid technologies for automation and control in a grid connected wind energy facility in South Africa,” *Energize*, Vol.3, June, pp. 35–38, 2015.
[10] P. K. Santra and P. V Kamat, “Mn-Doped Quantum Dot Sensitized Solar Cells: A Strategy to Boost Efficiency over 5%,” pp. 23–26, 2012.
[11] S. Africa, “Thin film PV modules offer over 4 % more energy than silicon PV in South Africa,” *Energize*, vol.3, June, 2015.
[12] J. Kamanzi and M. Kahn, “Development of a Renewable Energy-Based Cooling System for a Mobile Ground Station,” *Aerospace and Electronics Systems IEEE Magazine*, Vol.30, no 2, February, pp. 6–13, 2015.
[13] J. Kamanzi and M. Kahn, "Low energy cooling technology for a cubesat mobile ground station," *Industrial and Commercial Use of Energy 10th annual Conference*, Cape Town, South Africa, August 19-21, 2013.

Journal of Energy Challenges and Mechanics
ISSN 2056-9386
http://www.nscj.co.uk/JECM/

Scope:

Since James Watt, a Scottish inventor, improved efficiency of the steam engine, human civilization relies more and more on a steady supply of energy. Today we are at a transitional age. On the one hand, we see technology advances in the exploration and development of oil and gas, a depleting resource; we see growth in handling aging and decommissioning. On the other hand, we see ideas and plans for new energy infrastructure. This journal is about energy challenges and the underlying mechanics, involving multiple disciplines in science, technology, management and policy-making. Mechanics, fundamentally, is about force and the related behaviours, where force is about relationships, including those physical, human and social. For mechanics, the journal covers interactive boundaries with many other disciplines. For energy, topics include both fossil fuels and many different forms of renewable energy; also, issues related to energy economy, energy policy, efficiency, safety, environment and ecology will also be covered.

North Sea
Cove Bay, Aberdeen, Scotland, United Kingdom